Function of the mechano-gated ion channel NompC in tissue morphogenesis

Dissertation

for the award of the degree 'Doctor rerum naturalium' (Dr.rer.nat.) at the Philipps University, Marburg

Submitted by

Ankit Roy Choudhury

From Kolkata, India

Marburg, Germany 2023

This dissertation was prepared from 01.01.2020 to 30.06.2023 at the Department of Biology under the supervision of Prof. Dr. Jörg Großhans.

Accepted as a dissertation by the Department of Biology at the Philipps University of Marburg (university reference number 1180) on 28.08.2023

First reviewer: Prof. Dr. Jörg Großhans
Second reviewer: Prof. Dr. Annette Borchers

Date of defence: 26.09.2023

Declaration

I certify that I independently wrote my dissertation entitled “Function of the mechano-gated ion channel NompC in tissue morphogenesis” without unauthorised help. I did not use any sources or aids other than those I have expressly indicated.

This dissertation has not been submitted to any other university in its current or similar form and has not yet served any other examination purposes.

Marburg, 14.08.2023

Ankit Roy Choudhury

Acknowledgements

This thesis is the realisation of my earnest endeavour blended with the substantial support from everyone in the Developmental Genetics lab of Prof. Großhans at the Philipps University Marburg.

First and foremost, I thank my supervisor and mentor, Prof. Dr. Jörg Großhans. He helped me improvise my intrinsic ability of problem-solving through his scientific temper, optimism and a lot of tolerance to answer my questions. I sincerely appreciate all the valuable time he spent and the ideas he shared since I was a novice until the completion of the thesis. The enthusiasm he has for research is contagious and motivational for me. I humbly thank my thesis advisory committee members, including Prof. Dr. Annette Borchers and Prof. Dr. Dominik Oliver, for inspiring me to finish my thesis by sharing their valuable insights and ensuring I can progress smoothly.

I sincerely thank Prof. Dr. Fred Wolf and Dr. Matthias Häring for extending their hands of collaboration that led to a lot of excellent analysis. Meetings with Matthias helped me understand my research from a theorist's perspective.

My time at the lab has given me an environment of scientific and personal development, primarily through the regular departmental seminars, subgroup meetings and lunchtime discussions with my colleagues (Dr. Shuling Yan, Dr. Maria Kriebel, Dr. Deqing Kong, Dr. Na Zhang, Kaja Sommer and Roya Abbaszadeh). I thank Dr. Deqing Kong for his preliminary work on the project. He helped me with the technical details of the experiments. I was naive in *Drosophila* research when I joined, and his guidance made me evolve as a better fly pusher and researcher. I also thank Larissa and Chiara for their contribution as part of their Master's and Bachelor's dissertation programs.

I like to thank DAAD for providing me with financial support. As an associate member of GRK 2213, I thank GRK for the annual retreats, weekly seminars and many courses that helped me grow as a researcher.

Words cannot express my feelings for my parent's unconditional love and support. They believed in my potential and fostered me to let me be here today. Finally, I like to express my love for the person nearest to my heart, my friends and all the well-wishers. I feel honoured to be a part of this grand design of God.

Zusammenfassung

Mechanosensitive Ionenkanäle werden seit langem im Bereich der Neurobiologie untersucht. Ihre Rolle in anderen Geweben, insbesondere in Epithelgeweben, blieb jedoch unklar. Epithelzellen, die in Geweben dicht gepackt sind, können mechanische Kräfte, die von ihren Nachbarn erzeugt und übertragen werden, wahrnehmen und darauf reagieren. Eine solche mechanische Kommunikation zwischen Epithelzellen erfolgt klassischerweise über die Cadherin-Catenin-Komplexe an den Zellverbindungsstellen. Die von den Mechanomolekülen empfangenen mechanischen Signale werden dann entweder direkt durch die Reorganisation des Zytoskeletts weitergeleitet oder in biochemische Signale innerhalb der Zellen umgewandelt. Wir stellten die Hypothese auf, dass mechanosensitive Ionenkanäle in Epithelzellen ebenfalls als Mechanomoleküle wirken können.

Ausgehend von den bisherigen Erkenntnissen habe ich untersucht, ob NompC, der erste bekannte mechanosensitive Kanal in Drosophila, auch in den Epithelzellen exprimiert wird und, wenn ja, welche Funktion er dort erfüllt. Ich habe eine weit verbreitete Expression des NompC-Kanals in mehreren Geweben gefunden, einschließlich der Amnioserosa, einem hochdynamischen und kurzlebigen Epithelgewebe während des Dorsalschlusses, einem wichtigen morphogenetischen Transformationsereignis bei Drosophila. Das Fehlen von NompC führte zu zahlreichen Defekten im Prozess des Dorsalschlusses. Amnioserosa-Zellen weisen ein hohes Maß an Koordination auf, das sich in einem synchronisierten oszillierenden Verhalten zwischen benachbarten Zellen äußert. Meine Studie ergab, dass NompC ein wichtiger Regulator dieser Synchronie ist.

Ich fand auch heraus, dass NompC auf mechanische Kräfte im Amnioserosa-Gewebe reagiert und den Ca2+-Einstrom in die Zellen steuert. Die Abreicherung von NompC führte zu einer Störung der gerichteten Kraftverteilung im Gewebe und zu einer anisotropen Zellmorphologie. Ich fand heraus, dass NompC wichtig ist, um eine aktive Zelloszillation zu ermöglichen. Fehlt NompC, können die Zellen externe mechanische Kräfte nicht mehr effizient durch das Gewebe leiten. Ich fand mehrere interessante Veränderungen des Zytoskeletts, die direkt oder indirekt von NompC beeinflusst werden und die molekulare Grundlage für das Verhalten auf der Gewebeskala

darstellen. Zusammenfassend lässt sich sagen, dass diese Studie uns ein klares Verständnis der Rolle eines mechanosensitiven Ionenkanals, NompC, in Epithelzellen vermittelt. Es sind jedoch weitere Forschungsarbeiten erforderlich, um die Gate-Aktivität und die interagierenden Partner des NompC-Kanals aufzuklären.

Table of Contents

Abstract

Mechanosensitive ion channels have long been investigated in the field of neurobiology. However, their roles in other tissues, especially in epithelial tissues, remained elusive. Epithelial cells, being closely packed in tissues, can sense and are able to respond to the mechanical forces generated and transmitted by their neighbours. Such mechanical communication among epithelial cells is classically achieved via the cadherin-catenin complexes at the cell junctions. The mechanical signals received by the mechanomolecules are thereafter either directly transmitted through the cytoskeletal reorganisation or are transduced into biochemical signals inside the cells. We hypothesised that mechanosensitive ion channels can also act as mechanomolecules in epithelial cells.

Based on the previous findings, I went on to investigate if NompC, the first to be known mechanosensitive channel in *Drosophila*, is expressed in the epithelial cells too and, if so, what purpose it serves there. I have found a widespread expression of the NompC channel in multiple tissues, including the amnioserosa, a highly dynamic and short-lived epithelial tissue during dorsal closure, a major morphogenetic transformation event in *Drosophila*. The absence of NompC led to multiple defects in the dorsal closure process. Amnioserosa cells exhibit a high degree of coordination, manifested through a synchronised oscillatory behaviour between neighbouring cells. My study revealed that NompC is a critical regulator of this synchrony.

I also found that NompC is responsive to mechanical forces in the amnioserosa tissue and drives Ca^{2+} influx into the cells. Depletion of NompC caused a disruption in directional force distribution across the tissue and an anisotropic cellular morphology. I found NompC is important to facilitate active cell oscillation. An absence of NompC disables the cells to relay external mechanical inputs across the tissue efficiently. I found several interesting cytoskeletal changes that directly or indirectly are supposed to be affected by NompC as the molecular basis that translates into the downstream tissue-scale behaviour. In brief, this study provides us with a clear understanding of the roles of a mechanosensitive ion channel, NompC, in epithelial cells. However, more research is needed to elucidate the gating activity and the interacting partners of the NompC channel.

Abbreviations

%	Percentage
Δ	Deletion (knock-out)
°C	degree Celsius
µ	Micro-
a.u.	Arbitrary unit
Anti-sync.	Anti-synchronised
AS	Amnioserosa
BSA	Bovine serum albumin
DAPI	4', 6' – Diamidino-2-phenylindole
DC	Dorsal closure
ddH_2O	Double distilled water
DNA	Deoxyribonucleic acid
Ecad	E-cadherin
EDTA	Ethylenediaminetetraacetic acid
et al.	The Latin phrase for 'and others'
FRT	Flippase recognition target
GFP	Green fluorescent protein
in vitro	The Latin phrase for 'within the glass'
in vivo	The Latin phrase for 'within the living'
LE	Lateral epidermis
min	Minutes
NompC	No mechanoreceptor potential C
OrR	Oregon R
PBS	Phosphate buffer saline
PCR	Polymerase chain reaction
PIV	Particle image velocimetry
RNA	Ribonucleic acid
RNAi	RNA interference
ROI	Region of interest

s	Seconds
SDS	Sodium dodecyl sulfate
Sph-Sqh	Spaghetti squash
Sync.	Synchronised
TAE	Buffer solution of Tris base, acetic acid and EDTA
TMC	Transmembrane Channel-like protein
Tris	Tris (hydroxymethyl) aminomethane
TRP	Transmembrane Channel-like protein
UAS	Upstream activating sequence
WT	Wild-type

CHAPTER 1: Introduction

1.1. Epithelial morphogenesis: fixed-wired and self-organisation

Functionally similar aggregation of the same or different types of cells forms a tissue. The four major tissue types include epithelial, connective, muscular and nervous. The epithelial tissue comprises a group of closely connected cells that form the covering of external and internal organs. During organ formation, epithelial tissue, alongside other tissues, must remodel extensively to generate the right shape. The process is known as morphogenesis (Lemke and Nelson, 2021).

Morphogenesis etymologically means the 'formation of shapes' (Morali *et al.*, 2013). In nature, any structure formation event involving multiple objects has to happen via the establishment of a high degree of synchrony among them at the expense of individual randomness. Similarly, epithelial cells are meant to undergo a series of morphodynamic and functional changes during development without losing tissue integrity. From a classical viewpoint, genetic information controls tissue topology, and the physical contact between cells. According to modern understanding, all three act as mutually dependent critical determinants of the morphogenetic information flow (Levin, 2012; Nelson, 2009). Based on how these three factors influence the morphogenetic outcome, two principles have been theorised, i. Assembly according to a fixed program: the mechanical interaction between cells followed by morphogenesis is predetermined by the tissue's initial patterning (genetic) and geometry.; ii. Self-organisation: geometry and mechanics regulate each other as parts of a feedback loop constantly modulating morphogenetic changes, see Figure 1.1.b (Collinet and Lecuit, 2021a, 2021b). Figure 1.1.a exemplifies two natural events, i.e. germination of seeds and murmuration of Sterling birds. Both accept a collective definition of individuality in order to form shapes. Germination is mostly controlled by the gradients of genetic predeterminants, exemplifying a fixed-wired mode of information flow. On the contrary, the murmuration of birds purely depends on the momentary decision made based on the geometry and dynamics of the ensemble, representing self-organisation. Practically cellular morphogenesis is more of a combination of these two modes of action.

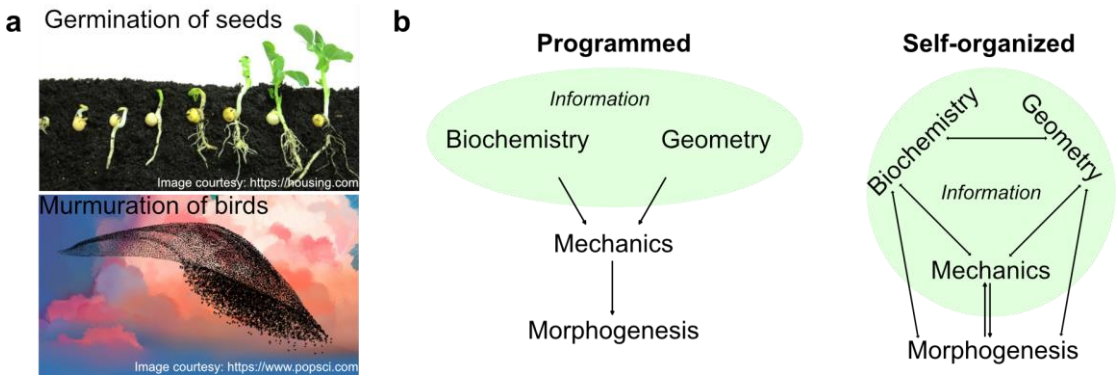

Figure 1.1. Two types of information flow. a. two natural phenomena exemplifying two distinct principles of 'shape formation'. Germination needs the biochemical imprints to be already stored in the seed. The murmuration of birds is more spontaneous, and the outcome cannot be anticipated from a snapshot. b. Programmed events are hierarchical and unidirectional, whereas self-organised events consider the inputs from ongoing changes. These are two extreme models. Practically coordination of cellular processes is achieved by combining both modes to different extents, depending on the process (Adapted and modified from Collinet *et al.*, 2021).

Cells undergo apical contraction via actomyosin assembly. This is simply the genetic/biochemical factor affecting the mechanics of the cell (Martin and Goldstein, 2014). During mesoderm invagination, a group of ventral epithelial cells is to contract apically to facilitate an inward movement of the tissue (Martin, 2020). However, individual apical constriction cannot sum up to bring about such a significant tissue-scale change. Self-organisation via cell-cell ordination is necessary, schematically described in Figure 1.2 (Rauzi *et al.*, 2013).

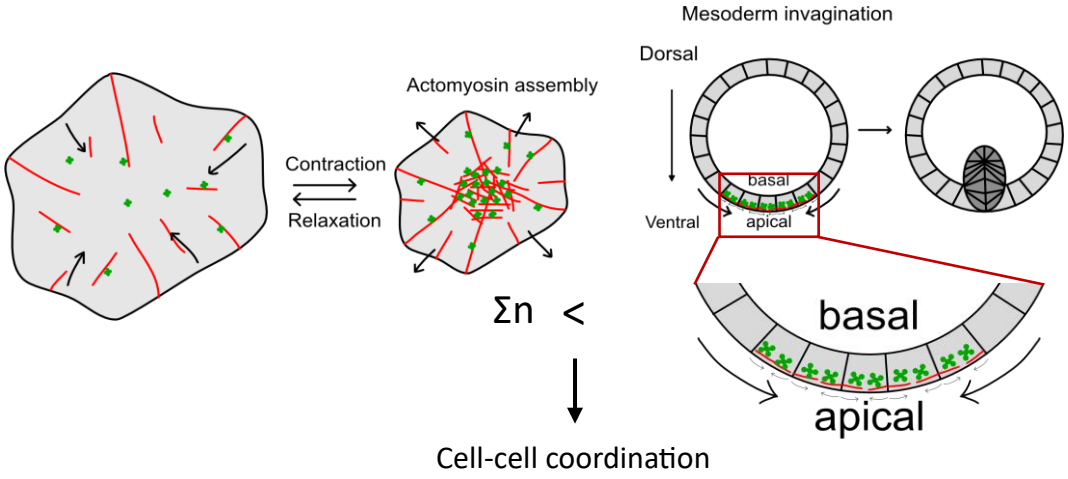

Figure 1.2. Cell-cell coordination is the key to morphogenetic events. Actomyosin assembly and disassembly is the key to cortical area change in the epithelial cells. The formation of actomyosin focus in the cell cortex makes the cell contract. However, individual contraction of cells here and there does not lead to the folding of an epithelial sheet. It requires a collective effort by a group of cells. These cells must coordinate spatiotemporally to ensure the morphogenesis at the right place and time.

Before going into the mechanisms of how cell-cell coordination is achieved, I will briefly go through a few major epithelial morphogenesis events in *Drosophila* and review the roles of programmed and self-organised modes of information flow in those contexts.

The tissue that emerges first during the embryonic development of *Drosophila* is the epithelium of blastoderm (Warn and Robert-Nicoud, 1992). From gastrulation onwards, this epithelial epidermis is subjected to a series of spatially defined morphogenetic movements, *e.g.* tissue invagination, collective cell migration, convergent extension, dorsal closure, tube formation, head involution *etc*. ~5 minutes after the cellularisation, the mesodermal precursors start migrating on the ventral side of the embryo forming ventral furrow (Sweeton *et al.*, 1991). Expression of two transcription factors, Twist and Snail, in a stripe of ventral cells, triggers apical contraction during mesoderm invagination (Martin, 2020). Simultaneously, the cephalic furrow formation separates the head from the trunk tissues, see Figure 1.3 a, a' (Spencer *et al.*, 2015). Another large-scale epithelial morphogenesis that partially overlaps mesoderm invagination is the germband extension. During germband extension, epithelial cells heavily rearrange to lengthen the tissue by ~2.5 fold; see Figure 1.3 b,

b' (Hartenstein and Campos-Ortega, 1985; Irvine and Wieschaus, 1994). *Even-skipped* and *runt* determine myosin polarisation and directional cell rearrangement during germband extension (Irvine and Wieschaus, 1994; St Johnston and Nüsslein-Volhard, 1992; Umetsu, n.d.). Parallel to germband extension, dorsal columnar cells become squamous and form AS. The AS tissue remains covered by the germband until the germband retracts posteriorly (Lacy and Hutson, 2016). The AS tissue eventually undergoes extrusion by the concerted contraction of the AS cells, and the dorsal opening is closed by the surrounding lateral epidermis, see Figure 1.3 c (Kiehart *et al.*, 2017). Spatiotemporal activation of the Jun kinase cascade is essential to facilitate actin and non-muscle myosin accumulation at the leading edge of the lateral epidermal cells during dorsal closure (Reed *et al.*, 2001).

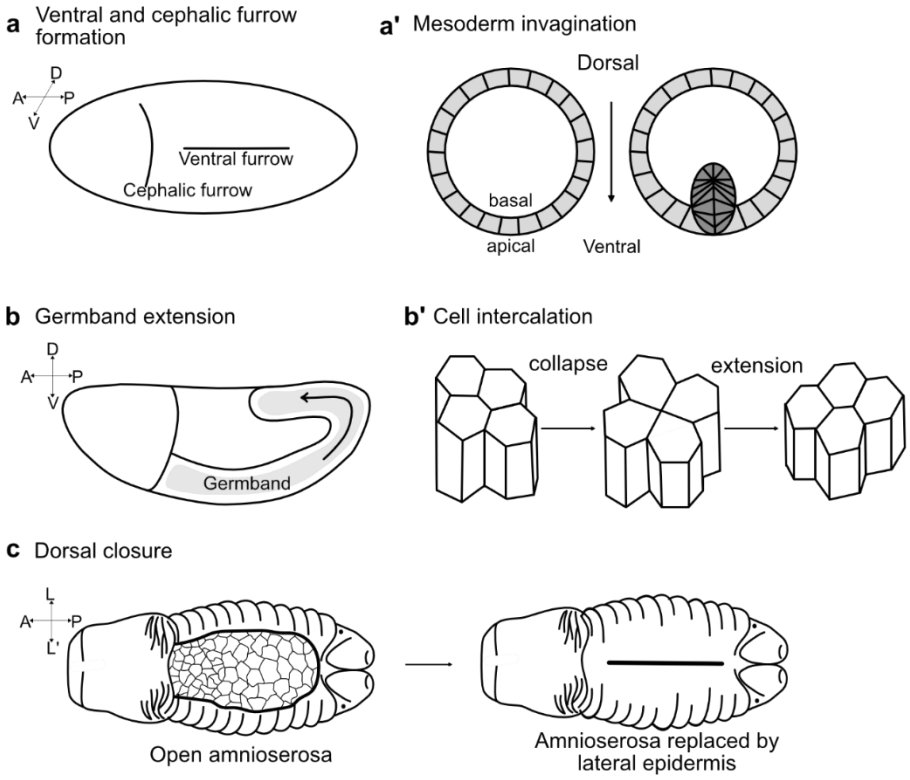

Figure 1.3. Examples of some important morphogenesis in *Drosophila*. a. Ventral and cephalic furrows form during stage 6 of *Drosophila* embryonic development. a'. Ventral furrow forms as a result of the concerted contraction of mesoderm precursor cells at the embryo's ventral surface. b. Germband extends ventrodorsally at the stage 8 embryos and covers the existing dorsal cells, which upon germband

retraction at stage 12, are called amnioserosa. b'. Germband consists of columnar epithelial cells that exchange relative positions instead of stretching and flattening individually. This results in simultaneous narrowing and lengthening of the germband tissue. c. Dorsal closure happens during stages 13-14. After germband retraction, the squamous epithelial cells at the dorsal side are exposed. Under this single sheet of tissue lies the yolk. The amnioserosa cells are eventually extruded and replaced by the cuboidal cells of the lateral epidermis.

None of the morphogenetic phenomena is mutually exclusive. On the contrary, spatiotemporally, they overlap and thus depend very much on each other. We now know not only the genetic determinants, as it is classically understood, but also multiple tissue-scale forces together with the changing geometry of the tissue influence cell-cell communication, which in turn decides the morphogenetic fate.

1.2. How cells communicate: Biochemical and mechanical signalling pathways

Chemical signalling relies on the ligand-receptor interaction. According to the classical 'lock-and-key' hypothesis, a ligand, as a key, fits into the right lock, *i.e.* the receptor (Lemieux and Spohr, 1994). This rather simplistic model was later revised and replaced by the 'induced fit' hypothesis (Koshland, 1958) or a more recent 'combination lock' hypothesis (Tripathi and Bankaitis, 2017). Ligand-receptor binding kicks off a cascade of molecular interactions and gene regulations. This is how the chemical signal is transduced to regulate many cellular activities. Based on the site of ligand-receptor binding and mode of action, receptors are membrane-bound (for lipophobic ligands) and intracellular (for lipophilic ligands). Based on the target of action, chemical communication is broadly classified into autocrine, juxtracrine, paracrine, and endocrine signalling pathways (Abe, 2000; Ben-Jonathan and Liu, 1992; Richards and Ascoli, 2018); see Figure 1.4.a.

Mechanical communication relies on the physical connection between the cells in apposition. The physical linkage is principally established by the robust trans-binding of cadherins of adherens junctions in parallel (Fichtner *et al.*, 2014). The cytoskeletal actin in close association with the adherens junctions are subjected to transduce the forces via dramatic reorganisation see Figure 1.4.b.

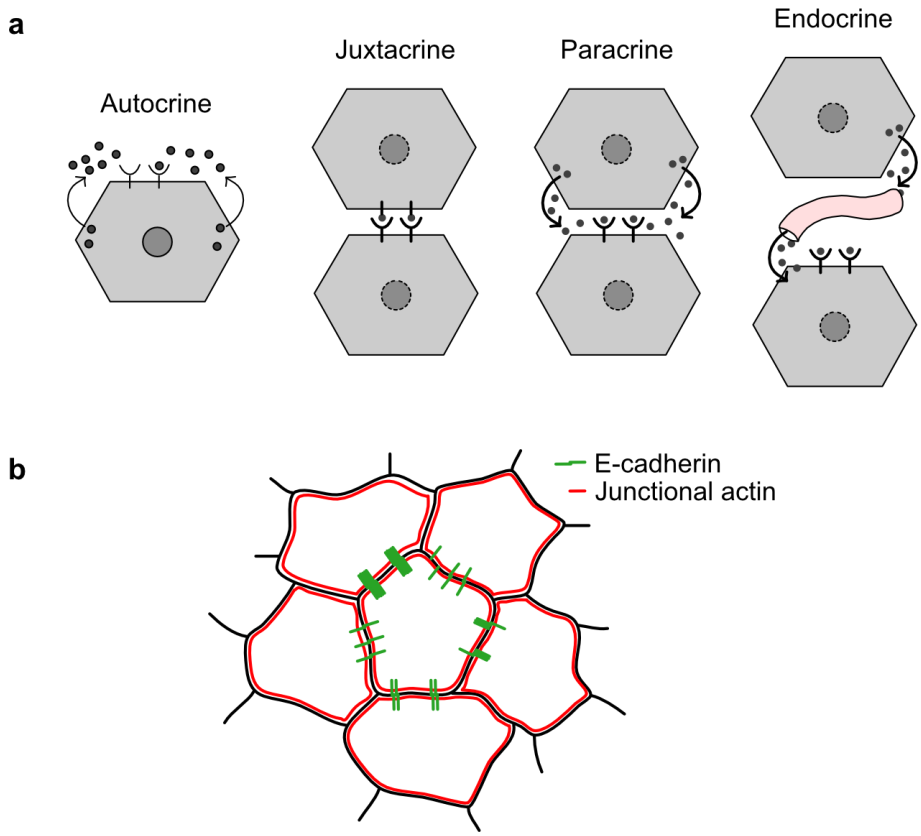

Figure 1.4. Cell-cell communication via a. Chemical signalling. Cells express the receptors on the membrane or the nucleus. The ligand interacts with its receptor to initiate the signalling cascade in the cell. In autocrine signalling, the ligand binds to the receptor in the same cell. Juxtacrine signalling involves ligand-receptor interaction between neighbouring cells. In this case, the ligand and the receptor are usually expressed on the cell membrane. In paracrine signalling, the ligand interacts with its receptor in another cell of the same tissue or cells not so far away. Endocrine signalling requires the ligand to traverse with the body fluid to act on far-off cells (Adapted and modified from Abe, 2000) b. Mechanical signalling. Epithelial cells tightly packed in a sheet-like tissue, are subjected to mechanical push-pull from the neighbouring cells. The principal sensors of the mechanical forces are E-cadherin molecules of the adherens junction. Trans-interaction between E-cadherins of apposed cells transduces mechanical forces into cytoskeletal reorganization or chemical signalling pathways.

To bring about a tissue-scale morphogenetic change by a group of chemically communicating epithelial cells, the cells must be pre-programmed to express the receptors and their ligands in a spatiotemporal fashion. This is known as patterning (Salazar-Ciudad *et al.*, 2003). Such pattern formations precede major morphogenetic events in *Drosophila*. For example, during convergent extension in *Drosophila*, two pair-rule transcription factors, *even-skipped* and *runt*, build up an anterior-posterior asymmetry by inducing the expression of three Toll-family receptors (Toll-2, 6, and 8) in an overlapping pattern (Irvine and Wieschaus, 1994; Paré *et al.*, 2014; Zallen and Wieschaus, 2004). This patterning is necessary for the extracellular domains of Toll 2 and Toll 6/8 to interact with each other as mutual ligand-receptors to set a polarised distribution of myosin that facilitates the polarised contraction of cell-cell boundaries along the dorsoventral axis and the exchange of neighbouring cells (Gilmour *et al.*, 2017; Tepass, 2014); see Figure 1.5 b.

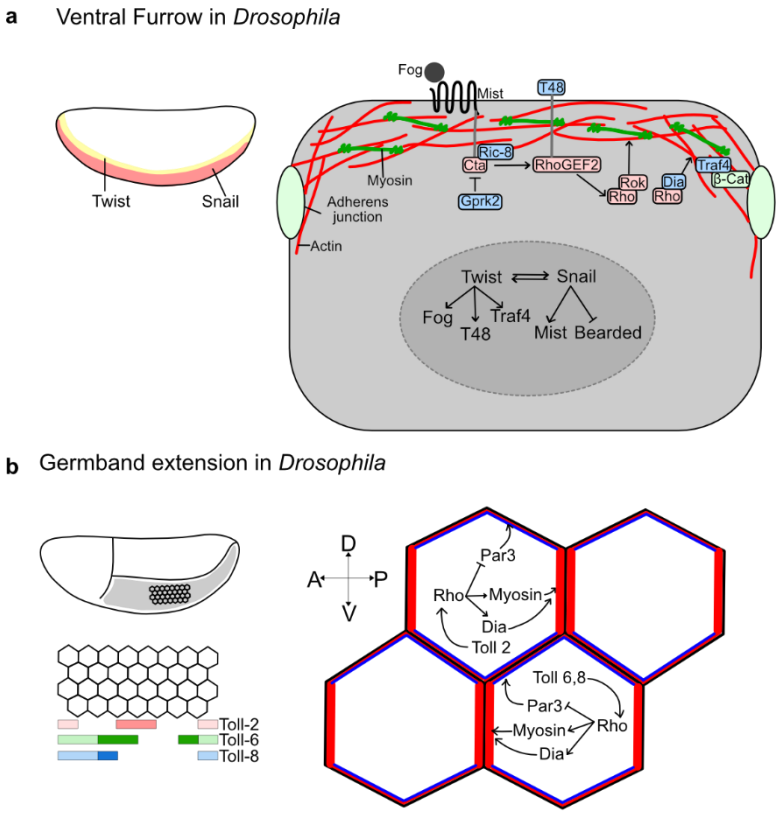

Figure 1.5. Examples of chemical signalling during Drosophila morphogenesis. a. Ventral furrow formation in *Drosophila* involves conditioning the mesoderm precursor cells via autocrine and paracrine signalling pathways. The Twist-target Fog interacts with GPCR Mist to activate the Rho-Rok signalling

pathway. The Rho-Rok complex activates myosin and regulates junctional actomyosin via Diaphanous (Dia). Another Twist-target, Traf-4, physically interacts with β-catenin (β-cat) and helps relocalising the adherens junction to the apical domain of the cell. b. Germband extension requires juxtracrine signalling between two adjacent columns of cells. Overlapping expression of Toll 2, 6, and 8 receptors creates anteroposterior asymmetry in the myosin expression. This leads to polarised shrinkage of cell junctions along the dorsoventral axis and neighbouring cell exchange. (Adapted and modified from Gilmour *et al.*, 2017; Tepass, 2014)

Similarly, the gradient expression of the nuclear *dorsal* establishes the dorsoventral axis (Roth *et al.*, 1989). The highest level of Dorsal in the prospective mesoderm activates Twist and Snail along the ventral midline. Snail regulates expression of transmembrane G-protein-coupled receptor, Mist which interacts with Fog. Expression of secreted Fog ligands is controlled by Twist as a transcription factor. The Fog/Mist pathway culminates in activating Rho-Rock mediated actomyosin accumulation to drive apical constriction. Figure 1.5.a describes the process elaborately (Perez-Vale and Peifer, 2020).

On the other hand, mechanical signalling depends on the direct perception of mechanical impulse from the neighbouring cell or within. Epithelium cells, being closely packed in a sheet of tissue, are highly responsive to mechanical inputs (shear flow, hydrostatic pressure, substrate stiffness, stretch, compression etc.) that the tissue is subjected to drive tissue-scale morphogenesis while maintaining tissue integrity. The most obvious changes epithelial cells exhibit in response to mechanical stimuli are via cell shape and cell rearrangement (Martin, 2010). Another prominent response is collective cell migration (Friedl and Gilmour, 2009), but during so, the cell undergoes epithelial-to-mesenchymal transition (EMT), so the hallmarks of epithelial cells are, to some extent, compromised. In the following sections, the role of mechanotransduction in epithelial morphogenesis and the molecules involved have been thoroughly discussed.

Here I highlight the differences and parallels between chemical and mechanical signalling pathways. Chemical signalling usually is much slower than mechanical signalling. While chemical signalling needs time in the range of minutes to days for ligand release, receptor-ligand binding and activation of the effector molecules, mechanical signalling is almost immediate, in a timescale of a seconds to sub-minutes

(Janmey and Miller, 2011). Chemical signalling is more fixed-wired compared to the mechanical counterpart. This is because chemical signalling activates or suppresses a long range of transcription factors which carries out a more persistent change in the cell (Miller and Davidson, 2013). Contrary to this, mechanical signalling induces dynamic reorganisation of junctional and cytoskeletal components and can act as a new signal generator (Cai and Sheetz, 2009; Uray and Uray, 2021). Despite these differences, both signalling pathways are not mutually exclusive. They are interdependent when it comes to morphogenesis. One such example where chemical signalling sculpts the mechanical property of the tissue is the establishment of planar polarised myosin during convergent extension (Huebner and Wallingford, 2018). The opposite is equally evident. For example, during *Drosophila* endoderm invagination, initial myosin-driven contraction by Fog signalling is perpetuated by the mechanical interaction between the apical domain of the buckling cells and the vitelline membrane (Bailles *et al.*, 2019; Das *et al.*, 2019; Kindberg *et al.*, 2020); see Figure 1.6.

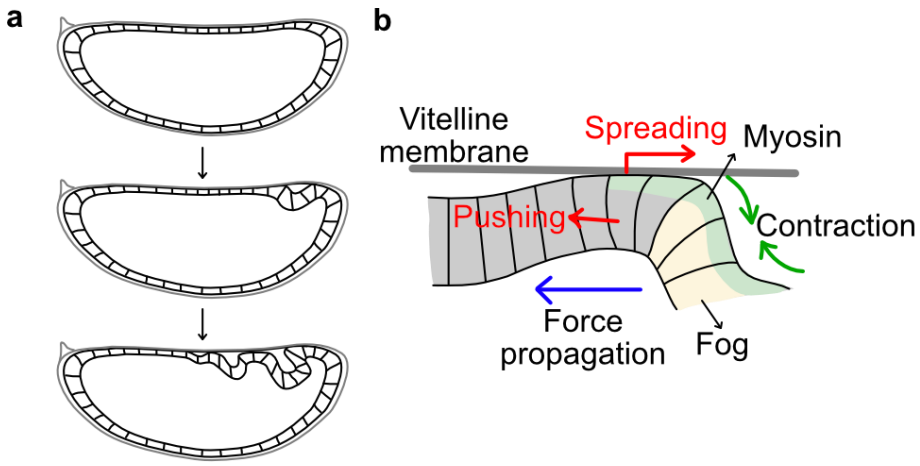

Figure 1.6. Mechanical modulation of chemical signalling. Although during endoderm invagination in Drosophila, the initial activation of MyoII is caused by Fog signalling, the subsequent travelling of MyoII wave and apical constriction is carried out by the cyclic forward pushing of the buckling cells and apical spreading of the edge cells along the vitelline membrane. In this example, the mechanics and geometry of the tissue are sufficient to perpetuate the initial mechanical output derived from chemical signalling. (Adapted and modified from Kindberg *et al.*, 2020)

1.3. Mechanical features of epithelial cells and their surroundings

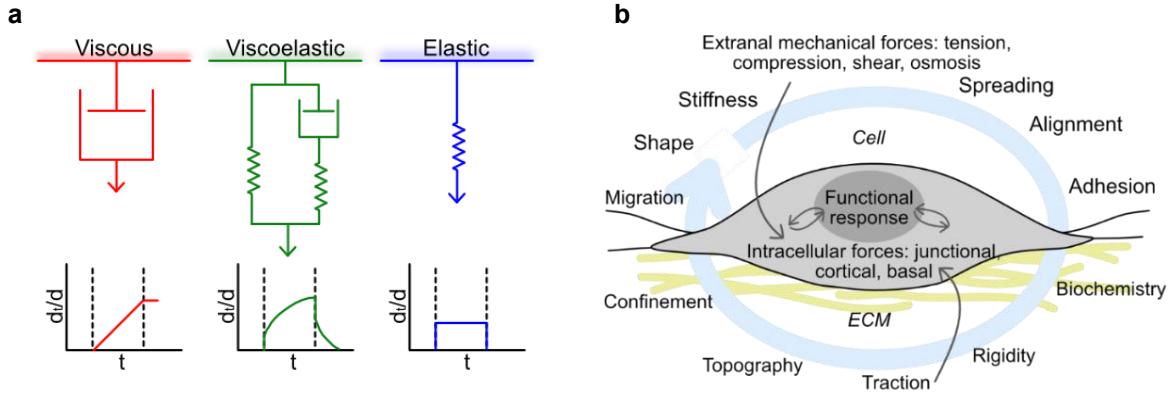

Figure 1.7. Mechanical property of epithelial cells. a. A schematic description of viscous, elastic and viscoelastic material. Upon stress, viscous materials (fluid) retain their shape, elastic materials (solid) regain their original shape, and viscoelastic materials regain their initial shape but at a slower pace. Epithelial cells are considered viscoelastic, of which the elasticity comes from the actomyosin, and the cytoplasmic drag causes the viscosity. (Adapted and modified from Molnar and Labouesse, 2021) b. Summary of forces acting on an epithelial cell and cellular response to them. Cell-cell adhesion and the ECM set the boundary conditions.

Epithelial tissue covers the organs internally and from the outside. In response to mechanical stress, epithelial cells possess the potential to change their shape by remodelling their junctions and cytoskeleton (Molnar and Labouesse, 2021). This property is the key to tissue morphogenesis in embryos. In homeostasis, cells tend to regain their shape after transient deformation (Guillot and Lecuit, 2013). Cells irreversibly alter their shape and positions during morphogenetic events (Clément *et al.*, 2017). However, in most cases, epithelial cells are viscoelastic, showing a combination of viscous and elastic behaviour (the physical terms are schematically shown in Figure 1.7.a (Bodenschatz *et al.*, 2022; Corominas-Murtra and Petridou, 2021). Studies with *Drosophila* embryos suggest that the cell cortex is most elastic while the cytosol is viscous (Doubrovinski *et al.*, 2017). Though the individual cells exhibit a more elastic response upon deformation (on seconds to minutes scale), a group of cells or tissue, on the contrary, appears more viscous (on a longer time scale) (David *et al.*, 2014; Jung *et al.*, 2020; Wyatt *et al.*, 2016).

Epithelial cells can sense and generate forces and other mechanical stimuli due to their interaction with surroundings, which usually trigger a functional response or are triggered by cellular activity (Chanet and Martin, 2014; Jaalouk and Lammerding, 2009; Martino *et al.*, 2018). These responses are broadly classified into physiological (transcriptional regulation, cell division, cell-cell adhesion), transformative (morphometric changes, differentiation), and motional (migration, reorganisation) (Hoon *et al.*, 2016). Intrinsic cues include cell density and shape, extracellular matrix (ECM) elasticity and topography, whereas forces due to shear stress, hydrostatic pressure, compression, and tension constitute the extrinsic cues (Petzold and Gentleman, 2021). The forces are mechanically or chemically transduced in the cell via the cytoskeleton that, in turn, activate signalling pathways (e.g. YAP/TAZ) (van Soldt and Cardoso, 2020); see Figure 1.7.b. The supracellular cytoskeletal network is pivotal in the instantaneous transduction of forces across the tissue (Chanet *et al.*, 2017). Rapid organisation and reorganisation of such networks depend on the force sensors (mechanomolecules) that rest at the cell-cell junctions (Angulo-Urarte *et al.*, 2020).

1.4. Molecular players of mechanotransduction: mechanomolecules

Many large protein assemblies and subcellular structures undergo conformational changes in response to mechanical forces, leading to local and global changes in cell organisation, behaviour, and differentiation. Here we call them mechanomolecules. A few of them are canonical and have been extensively researched, e.g. cadherin-catenin complex, integrins, actomyosin networks etc (DuFort *et al.*, 2011). Cadherin-catenin complex forms the part of the adherens junction that holds two neighbouring cells together, enabling the cells to perceive and respond to push-pull forces (Indra *et al.*, 2020; Li *et al.*, 2020; Mège and Ishiyama, 2017). Integrins, conversely, hold the cells with the ECM, making a perception of stiffness and traction forces possible (Mui *et al.*, 2016; Sun *et al.*, 2016). The Actomyosin network forms the dynamic cytoskeleton that modulates its density and orientation to transmit, amplify, or absorb mechanical forces (Murrell *et al.*, 2015). Here I will describe the cadherin-catenin complexes in more detail.

Cadherins are transmembrane glycoproteins that facilitate cell-cell adhesion in a Ca^{2+}- dependent way. In epithelial tissues, E-cadherins make homophilic interactions with each other to form clusters, namely, cis (lateral interaction among molecules of the same cell) and trans (interaction among the molecules of the neighbouring cell) (Perez and Nelson, 2004). These trans clusters are canonically understood to have three functions: adhesion tension: expansion of the cell-cell contact interface, adhesion coupling: opposing intra- and extracellular forces trying to separate the cells in contact; and adhesion signalling: ranging from actomyosin reorganisation to differentiation of tissues (Maître and Heisenberg, 2013). E-cadherin is physically associated with F-actin, which depends on α-catenin as an adaptor. The intracellular domain of E-cadherin binds to β-catenin, forming a stable link. α-catenin dynamically binds to β-catenin on one end with its VH1 domain while via its VH3 domain, it interacts with F-actin (Drees *et al.*, 2005). α-catenin undergoes reversible force-dependent conformational changes. Upon receiving the pulling force from the actin cytoskeleton, α-catenin takes up its open conformation. On one end, α-catenin binds to the cadherin-catenin complex in the open conformation. On the other end, it binds to the D1 domain of Vinculin via the mechanosensory modulatory (M) domain. When no force is applied, the M domain is inaccessible to interact with Vinculin and the associated F-actin (Buckley *et al.*, 2014; Kong and Großhans, 2020; Liang *et al.*, 2015). Thus, α-catenin and Vinculin act as force sensors and key F-actin regulators; see Figure 1.8.a.

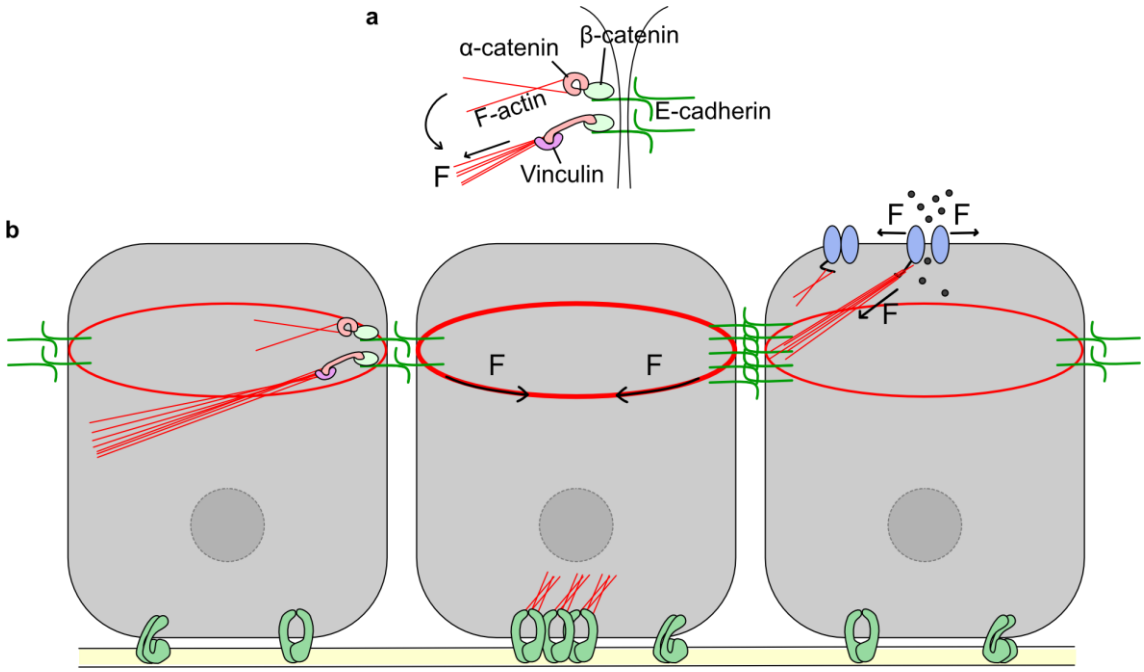

Figure 1.8. Schematics of mechanotransduction in epithelial cells. a. Epithelial cells are adhered to each other by the cadherin-catenin complexes forming the adherens junction. These complexes can sense force from both inside and outside the cell. Cadherins via extracellular homophilic interaction (trans clustering), build the machinery to sense push-pull forces from the neighbouring cells. On the cytoplasmic end, E-cadherin interacts with catenins. Upon sensing force from the actin cytoskeleton, α-catenin acquires conformation, making Vinculin binding site accessible. As a result, Vinculin binds and recruits more F-actin. On the basal domain, epithelial cells are attached to the basement membrane or extracellular matrix via the Integrin-Talin complex, which, in turn, interacts with F-actin. b. Epithelial cells with their various force-sensing and signal-transducing instruments. Other than the adherens junctions, subapical cortical actin ring is important to generate a homogeneous centripetal pulling force from inside the cell. Similarly, mechanosensitive channels detect forces and open up to allow ion influx. The gating mechanisms of these channels are highly speculative. Many channels have direct links to the cytoskeletal proteins (Actin, Tubulin etc.) and can sense forces from inside. Rests respond to the stretch or shear forces experienced by the cell membrane. They are highly investigated in neuronal cells and tissues. However, their role in epithelial mechanotransduction remained elusive. (Adapted and modified from Roy Choudhury *et al.*, 2021)

1.5. Mechanosensitive ion channels

Highly specialised sensory cells involved in hearing and proprioception can sense the forces (shear, vibrational, push-pull etc.) from their surroundings. However, almost

all eukaryotic cells can potentially detect mechanical stimuli via the conformational changes of membrane-bound proteins or protein complexes, the so-called mechanomolecules. These mechanomolecules can sense, transmit and transduce external mechanical signals into a cell. Adherens junctions, actomyosin cytoskeleton, G-protein coupled receptors, and mechanosensitive ion channels (MSCs) constitute a wide range of mechanosensors (Chen *et al.*, 2017; Martino *et al.*, 2018). MSCs are evolutionarily ancient, pore-forming, transmembrane proteins in almost every living organism ranging from archaea to bacteria to eukaryotes (Martinac and Kloda, 2003). In their open conformation, they allow ions such as Ca^{2+}, Na^{+}, K^{+}, and Cl^{-} to flow into or out of cells. The mechanism by which they switch from closed to open conformations and *vice versa* is called 'gating'. The gating behaviour is controlled by the forces acting parallel to the plasma membrane (membrane tension model) or by the forces exerted by the associated cytoskeletal or extracellular matrix proteins (tether model) (Ranade *et al.*, 2015; Sharif-Naeini, 2015). Channels are considered mechanically- gated, a. if a sufficient mechanical stimulus can immediately be transduced into the ion flux, at least faster than any other known second messenger b. if knocking them down leads to a loss of mechanosensory response, and c. reconstitution enables an otherwise insensitive cell to respond to mechanical stimuli (Christensen and Corey, 2007). In Figure 1.9, I have schematically summarised the gating mechanisms of a few mechano-gated ion channels, namely, Piezo, transmembrane Channel-like Protein (Tmc), Transmembrane protein 16 (TMEM16), epithelial sodium channel (DEG/ENaC), two-pore domain K+ channel (K2P), and last but not least, No Mechanoreceptor Potential C (NompC).

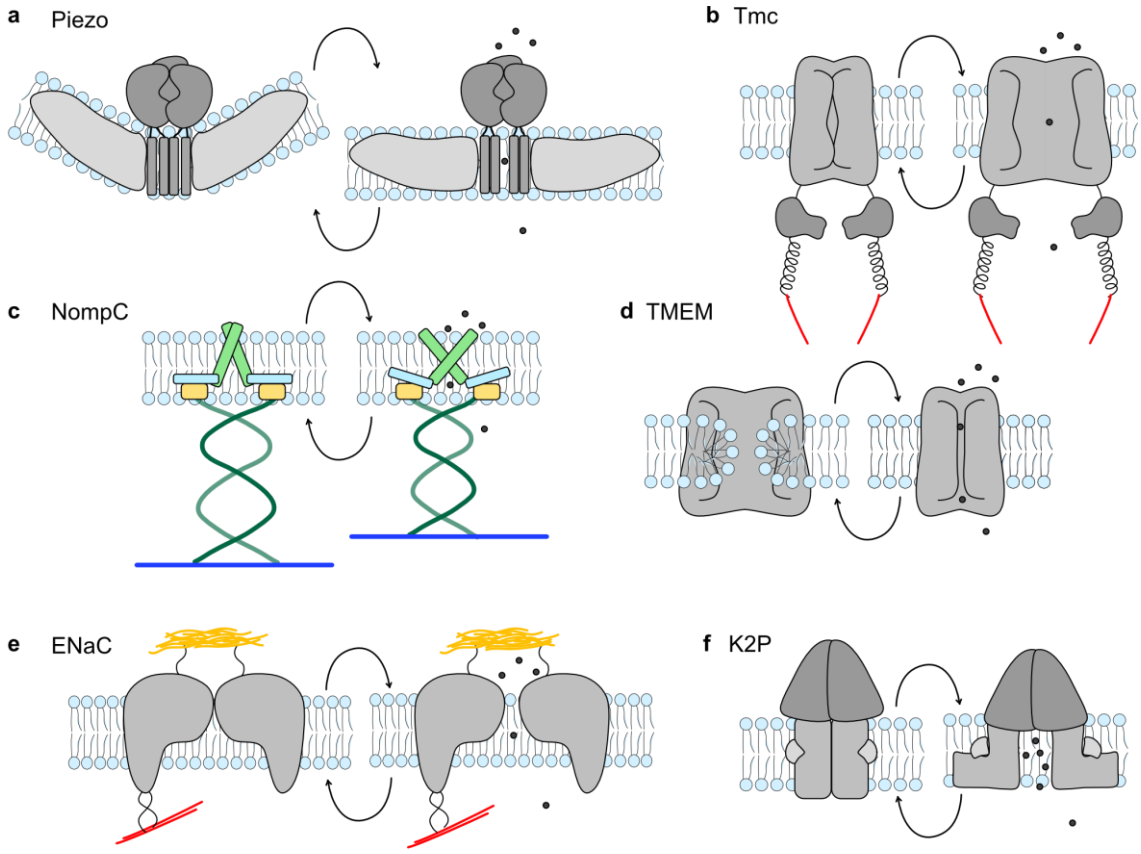

Figure 1.9. Schematic representation of mechano-gated channels and their proposed gating mechanisms. a. The Piezo channel forms a caveolae-like depression in the membrane. It is directly gated by tension from the lipid bilayer. Directional membrane tension opens the channel to allow Ca^{2+} influx. b. The transmembrane Channel-like protein (Tmc channel) forms complexes with other proteins (such as protocadherin 15) that bring extracellular mechanical inputs. Intracellular Tmc is linked to the cytoskeleton by ankyrin and calcium-binding proteins. The channel is gated by the tethering proteins from both extra and intracellular domains. c. No Mechanoreceptor Potential C (NompC) has a substantially long (29 ankyrin repeats) cytoplasmic domain that interacts with the microtubules. The gating of NompC depends on the deflections of the ankyrin repeat helices mediated by the cytoskeleton components. d. Transmembrane protein 16 (TMEM16) is a calcium-dependent chloride channel (CaCC). The dual function of TMEM16 as a lipid scramblase and as an ion channel makes it unique. These two functions are mutually exclusive and depend on the membrane tension-mediated conformational change of the protein. e. The epithelial sodium channel (ENaC) interacts with extracellular and intracellular proteins. Hydrostatic pressure, membrane stretch, and shear forces are the key mechanical cues that determine the gating of the channel pore. f. The lipid blocks the two-pore domain K^+ channel (K2P) in its closed state. Membrane tension releases the lipid blockade and allows the hinge-like bending of the transmembrane domain and, eventually, ion flux. (Adapted and modified from Roy Choudhury *et al.*, 2021)

The genome of *Drosophila* contains two Piezo genes: *Piezo* and *piezo-like* (*Pzl*). Though Piezo knockout adult flies are viable and fertile, larvae show significantly dampened behavioural responses toward obnoxious stimuli (Kim *et al.*, 2012). *Pzl* contributes to the locomotion and body gesture of the larvae. Distension of *Drosophila* midgut by mechanical forces leads to Piezo-mediate Ca^{2+}-influx to drive differentiation of secretory enteroendocrine (EEC) precursor cells into EEC cells (Beyder, 2018; He *et al.*, 2018).

Like Piezo, *Tmc* mutant *Drosophila* larvae exhibit defects in locomotion and have difficulty in food texture sensation (Guo *et al.*, 2016). The roles of *Tmc* in epithelial

morphogenesis has not been thoroughly studied yet. However, previous works in our lab showed an important function of *Tmc* in homogenous tension distribution across the oscillating amnioserosa cells and establishing synchronisation among neighbouring cells (Roy Choudhury *et al.*, 2021).

TMEM16 is Cl^- channel and helps maintain the critical cytoplasmic Cl^- concentration, which is necessary to regulate the microdomain positioning of $PI(4,5)P_2$, endocytic trafficking, and endosome recycling. It ensures membrane supply during ciliogenesis and junctional remodelling (He *et al.*, 2017). In *Drosophila*, the absence of *subdued* or TMEM16 results in dysmorphic epithelial architecture in the trachea and oesophagus (He *et al.*, 2017).

The ENaC proteins identified in Drosophila are Ripped pocket (Rpk) and Pickpocket (Ppk). *rpk* is prevalent in early embryos and adult ovaries. *ppk* is expressed in the sensory neurons of late-stage embryos (Adams *et al.*, 1998). Rpk is localised at the apical surface of AS cells. *rpk* mutant embryos show several defects in epitheliogenesis including impaired germband extension, dorsal closure, head involution, and consequent lethality (Hunter *et al.*, 2014). During imaginal disc development, Rpk depolarises the membrane potential of the anterior epithelial cells. Suppression of *rpk* leads to reduced depolarisation of anterior cells and disruption in the compartmentalisation between anterior and posterior cells (Emmons-Bell and Hariharan, 2021).

In the current study, I have mainly focussed on one of the old-known yet not-so-well-investigated ion channels, called NompC. NompC belongs to the TRPN family,

which comes under the superfamily of transient receptor potential (TRP) proteins. TRP superfamily contains more than 30 cation channels, of which most are permeable to Ca^{2+} or Mg^{2+} (Pedersen *et al.*, 2005). In 2000, the *nompC* gene was first identified in *Drosophila* during a screening of mechanoreceptive mutants with defects in mechanosensory physiology (Walker *et al.*, 2000). Loss-of-function point mutations of *nompC* virtually abolish the mechanosensory currents. Multiple nonsense and missense point mutations of *nompC* in *Drosophila* caused defects, such as hearing impairment, locomotion, gentle touch sensation, adaptive response to mechanical stimuli, and food texture sensation (Walker *et al.*, 2000).

The molecular structure of the NompC protein was resolved in 2017 using single-particle cryo-electron microscopy, See Figure 1.10.a. NompC contains a transmembrane domain, a short linker/neck domain, and a distinctive 29-ankyrin repeats long helical cytosolic domain (Jin *et al.*, 2017a). This ankyrin repeat helix interacts with microtubules and acts like a compression spring to convey force from the cytoskeleton to the channel, thus controlling the gating (Wang *et al.*, 2021). TRP channels are reported mostly to be permeable for monovalent cations like Na^{+} and K^{+} and divalent cations like Ca^{2+} (Ferrandiz-Huertas *et al.*, 2014; Lehnert *et al.*, 2013; Yan *et al.*, 2013). Ca^{2+} influx is known to change the conformational state of motor proteins that, in turn, modify cellular tension (Lehnert *et al.*, 2013). Recent findings demonstrate that point mutations of *nompC* lead to defective dorsal closure phenotypes in *Drosophila*, such as irregular purse string and increased embryonic lethality (Hunter, 2012). Furthermore, overexpressing NompC constructs with truncated ankyrin repeats in amnioserosa results in defective dorsal closure phenotypes, like failure to organise an actomyosin purse string, absence of leading-edge cell elongation, *etc* (Hunter, 2012).

The atomic structures of Tmc and Piezo channels were also resolved in past years. TMC-1 in vertebrates is one of the multiple subunits (the others being cytoplasmic CALM1, a Ca^{2+}-binding protein and TMIE, an integral membrane protein) together forming a transmembrane pore structure, see Figure 1.10.b. Homotrimerisation of Piezo subunits forms the pore-forming central cap domain. The transmembrane blade domains cause local deformation in the lipid bilayer in their innate state, see Figure 1.10.c.

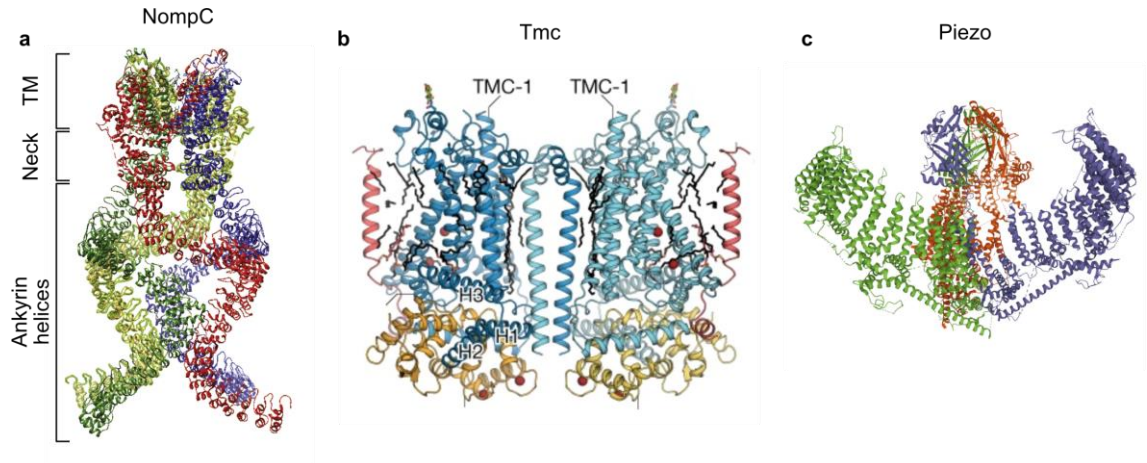

Figure 1.10: Atomic model of NompC, Tmc and Piezo. a. NompC. The transmembrane (TM) domain forms six transmembrane α-helices. Both the N- and C-termini of the protein are intracellular. The functional channel is a homotetramer having the N-terminal domain in contact with the cytoplasmic microtubules. (Adapted from Jin *et al.*, 2017) b. Tmc. The transmembrane pore-forming domain consists of TMC1 and TMIE (pink). CALM1 (orange) forms the cap domain at the cytoplasmic face (Jeong *et al.*, 2022). c. Piezo. Side view of the protein with a centrally placed extracellular cap domain (forms the pore) and the curved blade domains (sense force) embedded in the lipid bilayer (ttp://www.rcsb.org/pdb/home/home.do).

1.6. Role of Calcium in epithelial cell activity

Calcium signalling in epithelial morphogenesis is crucial in various model organisms. The convergent extension is defective if the calcium signalling is inhibited in Zebrafish and Xenopus. In contrast, gastrulation in *Echinoidea*, neural fold formation in *Ambystoma*, and egg chamber elongation in *Drosophila* are triggered by an experimentally induced rise in calcium ion (Ca^{2+}) concentration (He *et al.*, 2010; Lam *et al.*, 2009; Lane *et al.*, 1993; Moran and Rice, 1976; Wallingford *et al.*, 2001). In the early embryos of *Drosophila,* two patterns of Ca^{2+} activity have been detected: (a) spontaneous and repetitive Ca^{2+}-waves, which are often followed by a wave of tissue contraction, and (b) Ca^{2+}-spikes that stochastically and transiently arise in a single cell or a group of few cells (Markova *et al.*, 2019). In the *Drosophila* wing disc, intracellular Ca^{2+} transients function to integrate signals and decrease over time as the wing disc matures (Balaji *et al.*, 2017; Brodskiy *et al.*, 2019). Increased intracellular Ca^{2+} concentration regulates calcineurin and CRTC (CREB-regulated transcriptional co-

activator) (Deng *et al.*, 2015), corresponding to intestinal stem cell proliferation in *Drosophila*. In processes like wound healing, Ca^{2+}-waves help to build rapid communication across multiple cells (Jaffe, 2010; Leybaert and Sanderson, 2012). Ca^{2+}-spikes are reported to have a close association with Wnt signalling (Slusarski *et al.*, 1997), the inhibition of which leads to a decrease in spike activity and, eventually, morphogenetic impairment of the developing embryo (Markova and Lenne, 2012; Sheldahl *et al.*, 2003). Such waves and spikes temporally coincide with dorsal closure, cuticle formation, head involution and so on (Markova *et al.*, 2019; Markova and Lenne, 2012), and thus hold the potential to regulate various morphogenetic events, see Figure 1.11.

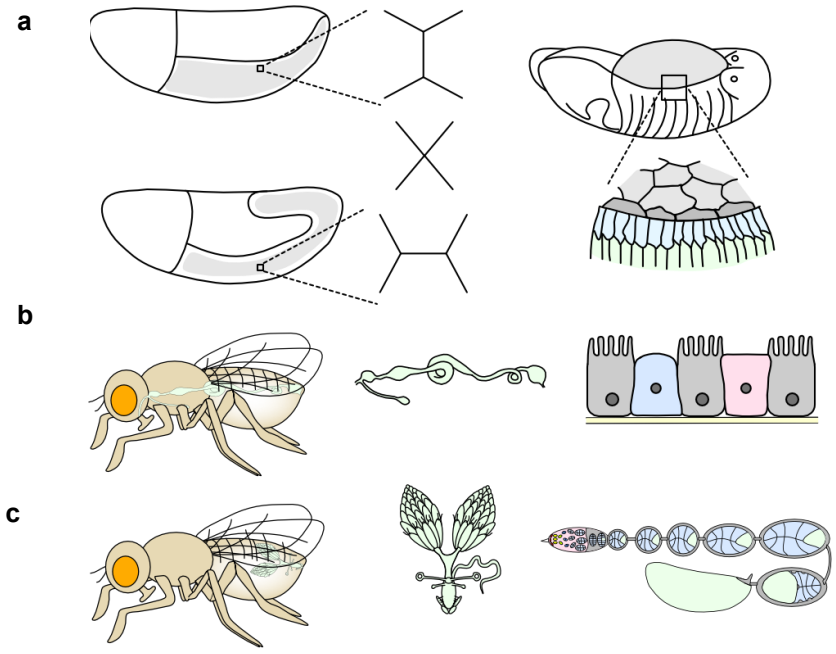

Figure 1.11. Ca^{2+} dynamics corresponding to epithelial tissue dynamics and homeostasis. a. The frequency of Ca^{2+}-spikes increases during the fast phase of germband extension. In *Xenopus*, Ca^{2+} waves are accompanied by a wave of contraction within the tissue. Pharmacological depletion of calcium stores abolishes Ca^{2+} dynamics and inhibits convergent extension. b. UV-mediated uncaging of chelated Ca^{2+} is sufficient to drive cell contraction in AS tissue. Also, endogenous Ca^{2+} fluxes correlate with cell contraction in the AS cells during dorsal closure. c. *Drosophila* midgut consists of cuboidal epithelial cells: enterocyte with microvilli for absorption, intestinal stem cell (light blue) for regeneration and proliferation, and enteroendocrine cell (pink) for secretion. Piezo-mediated Ca^{2+}-influx is attributed to the differentiation of the EEC cells. d. The *Drosophila* ovary comprises a chain of developing egg

chambers. In each egg chamber, a single oocyte and 15 supporting nurse cells are surrounded by a dense monolayer of cuboidal epithelial cells called follicle cells. Ca^{2+} regulates egg chamber elongation, which depends on the asynchronous oscillation of these cells. (Adapted and modified from Roy Choudhury *et al.*, 2021)

The reciprocity between cell contraction and adherens junction-mediated force transduction to the neighbouring cells gives rise to tissue-scale behaviours like folds and furrows formation (Liang *et al.*, 2015). Intracellular Ca^{2+} has long been recognised to regulate contraction in many cell types, including muscle cells (Kuo and Ehrlich, 2015), stromal fibroblasts (Lembong *et al.*, 2017; Nobe *et al.*, 2000), and epithelial cells in culture (Lee and Auersperg, 1980). *In vivo*, intracellular Ca^{2+} induces contractility in amnioserosa cells during dorsal closure (Hunter *et al.*, 2014), ectoderm cells during neural tube closure (Lee and Nagele, 1986; Suzuki *et al.*, 2017), and neural plate folding (Smedley and Stanisstreet, 1986). Ventral furrow formation during gastrulation and contraction of amnioserosa cells during dorsal closure highlights the importance of a 'ratchet' mechanism caused by the pulsatile cortical network of medioapical actomyosin (Sutherland and Lesko, 2020). The contractility in such non-muscle cells is primarily driven by non-muscle myosin II (NM II) regulated by Rho-ROCK signalling (Vasquez *et al.*, 2016; Verdier *et al.*, 2006; Vicente-Manzanares *et al.*, 2009). In the follicle cells of *Drosophila*, intracellular Ca^{2+} seems to regulate the basal concentration of NM II. Chelation of cytosolic Ca^{2+} by BAPTA reduces basal NMII. The effect can be reversed by ionomycin driving Ca^{2+} influx (He *et al.*, 2010). Intracellular Ca^{2+} can also directly bind to and form a complex with tetravalent calmodulin protein, activating myosin light chain kinase (MLCK), which activates the regulatory light chain of NM II downstream (Hartshorne *et al.*, 1998; Totsukawa *et al.*, 2000) (Figure 1.12).

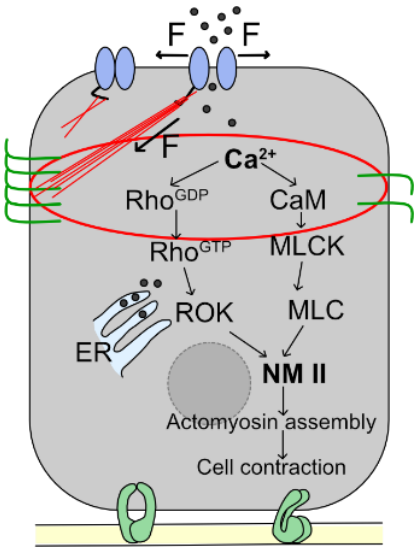

Figure 1.12. Calcium signalling modulates cytoskeletal assembly in epithelial cells. Increased intracellular Ca^{2+} modulates actomyosin assembly by activating non-muscle myosin II (NMII), the effector molecule, via one of the two main signalling pathways, Rho-ROCK and MLCK. CaM, calmodulin; MLCK, myosin light-chain kinase; MLC, myosin light-chain; ROCK, Rho-associated kinase. (Adapted and modified from Roy Choudhury *et al.*, 2021)

The amnioserosa consists of a monolayer of 150–200 autonomously oscillating squamous epithelial cells covering the dorsal opening of the developing *Drosophila* embryos of stages 13–15 (Kiehart *et al.*, 2000; Martin and Goldstein, 2014). Inducing rapid Ca^{2+} bursts by uncaging intracellular Ca^{2+} can trigger the contraction of amnioserosa cells in single-cell resolution (Kong *et al.*, 2019). This is mediated via NM II activation, wherein Ca^{2+} reportedly activates ROCK (Rho-associated kinase) in the Rho-ROCK pathway. Not only directly phosphorylates the myosin II regulatory light chain (RLC), but ROCK also prevents dephosphorylation of NM II by inhibiting protein phosphatase I (PP I), stabilising the activated NM II (Newell-Litwa *et al.*, 2015). MLCK, if constitutively activated in the entire amnioserosa, leads to overall rounding of the cells. Expression in single cells triggers impetuous apical constriction (Homem and Peifer, 2008). Rho and MLCK can act parallelly. In 3T3 fibroblast cells, MLCK is peripherally localised, whereas ROCK is localised more centrally (Totsukawa *et al.*, 2000). This skewed localisation concerns the spatial asymmetry in the stability of the

actomyosin structure within a cell. It could be further investigated to confirm such an argument in epithelial cells.

1.7. Apical constriction driving epithelial morphogenesis

Epithelial cells undergo highly dynamic collective movements and deformations to give rise to new shapes and structures. Apical constriction means the shrinkage of the apical area of an epithelial cell, causing the cell to take up a wedged shape (Martin and Goldstein, 2014). Coordinated apical constriction of a group of epithelial cells produces tissue bending and thus plays an important role in driving many local and global morphogenetic changes from invertebrates to vertebrates, *e.g.* gastrulation in *Caenorhabditis elegans* (Goldstein and Nance, 2020), *Drosophila melanogaster* (Martin, 2020); neural tube closure (Inoue *et al.*, 2016), lens placode formation (Plageman *et al.*, 2010) and primitive streak formation (Rivera-Pérez and Hadjantonakis, 2015) in vertebrates, among many others.

The principle force-generating component driving apical constriction is implicated to be the network of filamentous actin (F-actin) motored by non-muscle myosin II (Martin *et al.*, 2009). In its active GTP-bound state, RhoA activates Rho-associated coiled-coil kinase (ROCK) and also Diaphanous (Dia)-related formins (Lai *et al.*, 2008; Martin and Goldstein, 2014). Formins nucleate the unbranched actin filaments (Courtemanche, 2018), whereas ROCK activates and facilitates myosin condensation in the medioapical cortex (Coravos and Martin, 2016). A mutant version of ROCK that localises diffusely rather than centrally can inhibit apical constriction of epithelial cells (Coravos and Martin, 2016). Also, the seemingly randomised actin filaments are shown to have their barbed ends enriched at cell junctions. Another way of apical constriction is via the contraction of the circumferential actomyosin belts that underlie the cell junctions (Martin, 2010). Such actomyosin belts exhibit planar-cell polarity and are recruited in neural tube formation in vertebrates (Matsuda and Sokol, 2021). Cell polarity regulating protein complex Bazooka/Par3, Par6 and aPKC supports myosin activity and determines the rate and duration of actomyosin condensation (Nance and Zallen, 2011; Tostevin and Howard, 2008). To achieve an efficient apical constriction and coordination with the neighbouring cells without compromising tissue

integrity, cell junction proteins, especially the adherens junction proteins (E-cadherin, ß-catenin, α-catenin), has to have a coupling with the actomyosin aggregates. Disrupting adherens junction proteins leads to a loss of concert between myosin flow and cell shape change (in *C. elegans*) (Slabodnick *et al.*, 2023) or an inefficient contraction of the apical circumference while having a continuous myosin flow into the medioapical surface (in *Drosophila*) (Sumi *et al.*, 2018).

The anchoring (coupling strength) between junction proteins and medioapical actomyosin determines the degree of deformability and recovery after each contraction (Miyake *et al.*, 2006). High deformability and high recovery indicate more fluidity and less resistance, and *vice versa*, see Figure 1.13.

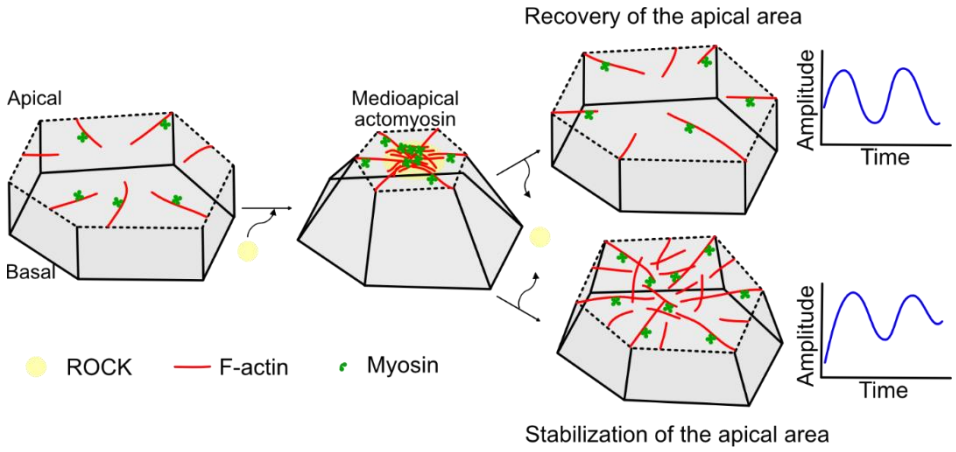

Figure 1.13. Mechanism of apical contraction in epithelial cells. The apical surface of epithelial cells undergoes contraction in several morphogenetic processes. The apical surface is marked with a dotted line. The contractile force is generated by Rok-dependent phosphorylation and activation of Myosin II. Cortical actomyosin accumulates centripetally (forming focus), causing the shrinkage of the apical surface. Being viscoelastic in nature, cells attempt to regain the initial apical area upon disassembly of the foci. The persistent F-actin filaments between two contractions act like a ratchet to stabilise the contracted surface area.

Recent research has pointed out two independent populations of F-actin in the medioapical cortex: pulsatile in a Rho1-dependent manner and homogeneous and persistent (present in between pulses), and having Frl/Fmnl-dependent nucleation (Dehapiot *et al.*, 2020). Like a ratchet, persistent actin filaments help stabilise the apical

surface area between two myosin pulses. Thus, the cell undergoes incremental contraction after each pulse.

Experiments with a phosphomimetic version of myosin have demonstrated that it disrupts incremental apical constriction and facilitates continuous constriction (Vasquez *et al.*, 2014). It also showed that pulsatile actomyosin assembly and disassembly, rather than a continuous accumulation, is required to maintain a supracellular actin network connection that mechanically links a large population of cells. This supracellular network helps to bring about a global morphogenetic change, such as tissue invagination, without losing tissue integrity (Yevick *et al.*, 2019).

1.8. Oscillatory behaviour of amnioserosa (AS) cells: the model system

Amnioserosa (AS) is a squamous epithelial tissue that plays a crucial role during the dorsal closure of the *Drosophila* embryo. During the cellularisation phase, the embryo consists of a homogeneous pull of cuboidal cells at the periphery of the embryo (Lacy and Hutson, 2016). Along with germband extension, ~200 dorsal-most columnar cells form the AS by flattening and dramatically changing their aspect ratio (laterally elongated). Its formation depends on the gradient expression of Decapentaplegic (dpp) and zerknüllt (zen) (Créton *et al.*, 2000; Lynch *et al.*, 2012). AS rests under the germband for quite a while until the germband retracts, leaving the dorsal side of the embryo occupied only by AS (McCleery *et al.*, 2019). Figure 1.14 shows the location and morphology of AS tissue and cells.

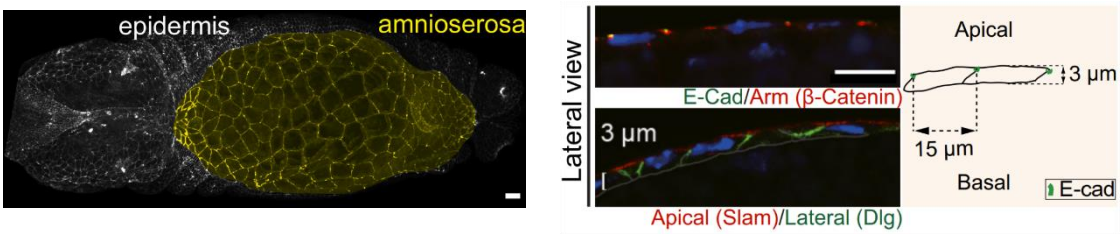

Figure 1.14. Position and morphology of AS. a. Amnioserosa tissue highlighted in yellow from embryo expressing ECad-GFP. AS bridges the lateral epidermis from both sides. b. Sagittal section of AS cells from E-Cad-GFP embryos stained for GFP, β-Catenin (adherens junction marker), Slam (apical marker), and Dlg (lateral junction marker) (Adapted from Kong *et al.*, 2019)

AS does not contribute to embryonic tissue. However, it facilitates two major morphogenetic events of the embryo: germband retraction and dorsal closure (McCleery *et al.*, 2019). Germband retracts to align the u-shaped germband along the straight line of body segments. AS mediates this movement by signalling and physical interaction with the underlying yolk sac (Schöck and Perrimon, 2003). During dorsal closure (DC), the lateral epidermis from both sides of AS is sealed along the dorsal midline (Lv *et al.*, 2022). AS guides DC in conjunction with the yolk sac and the leading edge of the lateral epidermis by providing contractile force.

After germband retraction, the AS is exposed in an elliptical shape. Between germband retraction (GBR) and initiation of DC, the surface area of AS cells fluctuates in a periodic fashion without a significant change in the overall area of the AS (Jayasinghe *et al.*, 2013). This phase is called the elliptical/stationary phase. This phase lasts 45 minutes to 1 hour until dorsal closure starts. The periodicity of 230±76 s in apical contraction is contributed by the periodic assembly and disassembly of medioapical NMII at the cell cortex(Sokolow *et al.*, 2012; Solon *et al.*, 2009). Figure 1.15 schematically summarises the morphogenetic movements during DC.

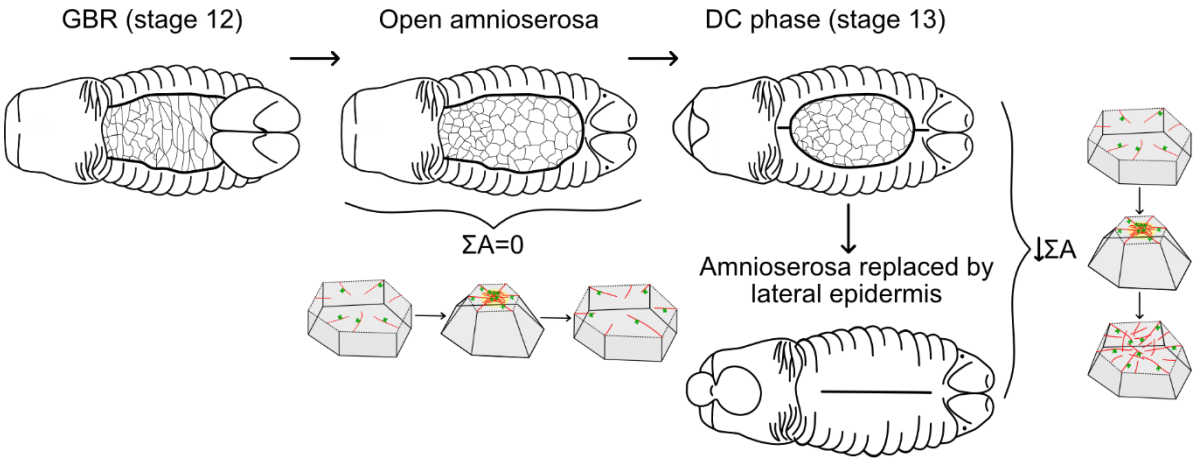

Figure 1.15. DC dynamics. Developing *Drosophila* embryo undergoes germband retraction to expose the dorsal opening of the embryos covered by the squamous epithelial monolayer called amnioserosa (AS). The tissue remains elliptical during the stationary phase. The apical area of the cells fluctuates in an oscillatory manner in association with the assembly and disassembly of the cortical actomyosin foci. The cells regain their initial surface area after every contraction and relaxation cycle. However, during

the late (DC phase), the cells tend to retain their contracted apical area, thereby undergoing apoptosis and extrusion.

Solon *et al.* has shown that the AS cell surface area fluctuation is non-autonomous and depends on the pulsation pattern of the direct neighbours. The pulsing of a pair of cells is shown to be either in-phase (correlated) or anti-phase (reverse-correlated) (Solon *et al.*, 2009). Such coupling fades with distance, i.e. far-away cells do not seem to affect the oscillation of a cell. Laser-induced cut at cell-junction of two adjacent cells leads to relaxation of the surrounding tissue. The immediate neighbours of the ablated site stop the oscillation almost instantaneously (Jayasinghe *et al.*, 2013). These experiments suggest that the AS cell oscillations are neighbour-dependent and temporarily coordinated. Although cell-cell coordination has been studied using a few numbers of AS cells, a tissue-scale study of cell coordination is hardly undertaken. In this study, I have exploited the potential of the AS to study the dynamics of cell-cell coordination on a tissue scale.

1.9. Multiple forces at play: morphodynamic regulators of AS cells

Building new shapes without losing integrity requires precise distribution of physical forces for tissues undergoing morphogenesis. Spatiotemporally regulated force generation, transmission and dissipation are key to achieving such precision. Dorsal closure (DC) is a good example of this. Two highlights of DC are 1. continuous, pulsatile contraction of AS cells (Pasakarnis *et al.*, 2016) and 2. dorsal-ward movement of the supracellular actin cable (purse-string) along with the leading edge cells of lateral epidermis from either side of the dorsal opening (Hayes and Solon, 2017; Jacinto *et al.*, 2002; Lv *et al.*, 2022).

During the first (stationary) phase, the leading edge remains uneven, oscillating dorsoventrally in correlation with the oscillation of the AS cells. However, a steady accumulation of F-actin along the purse string leads to the straightening of the leading edge that guides the lateral epidermal cells to move dorsally during the second (closure) phase (Lv *et al.*, 2022).

Disruption of actomyosin-driven AS contractility leads to failure in DC (Flores-Benitez and Knust, 2015; Young *et al.*, 1993). This contraction is resisted by the intracellular hydrostatic force exerted by the body of the AS cells (Saias *et al.*, 2015). In addition, leading edge cells surrounding amnioserosa generate an overall pulling force that resists the contractile force of AS cells (Wells *et al.*, 2014). Laser dissection of these cells results in persistent retraction of epidermal cells preventing DC (Hutson *et al.*, 2003). During the second phase of DC, the actomyosin purse string plays a vital role by acting like a ratchet and stabilising the small dorsal-ward movement of epidermal cells along with each contraction of AS cells, thus shortening the leading edge and bringing the two epithelial sheets together (Solon *et al.*, 2009). Finally, when the two sheets come together at the anterior and posterior ends of the dorsal opening, the epidermal cells form sheet and finger-like projections (lamellipodia and filopodia, respectively) to establish adhesive contacts (canthi) that eventually zip shut the opening (Hayes and Solon, 2017). The force vectors are schematically summarised in Figure 1.16.

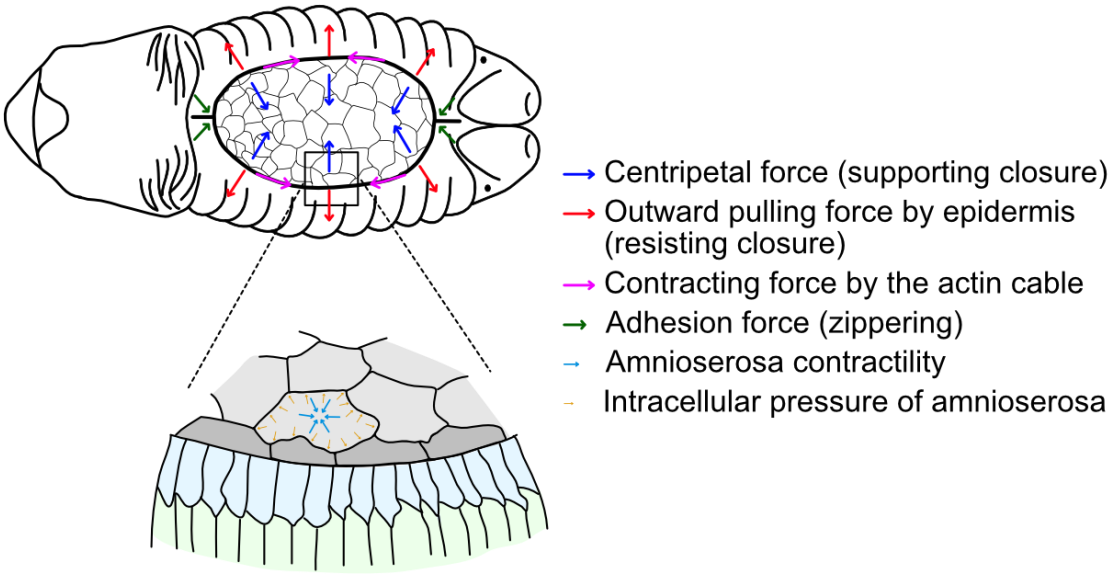

Figure 1.16. Schematic map of various forces active across the AS and the surrounding lateral epidermis tissue during DC. (Adapted and modified from Hayes *et al.*, 2017)

Objectives

We know morphogenetic changes require rapid cell-to-cell communication and a notable degree of cell coordination. In this context, the roles of several mechanomolecules have been studied in detail. However, except few studies with *piezo* in epithelial cells, so far, mechano-gated channels, including *nompC,* have mostly been implicated in neuronal physiology, contributing to balance, hearing and sound response, gentle touch sensation and nociception. Hence, we wonder if cells closely packed in an epithelial tissue also exploit these mechano-gated channels to perceive mechanical changes happening in neighbourhood cells in a way quite similar to touch sensation but at a more cellular level. Amnioserosa comprising a group of highly dynamic and tightly packed epithelial cells, thus, fits to be the model system to test our hypotheses.

In the present study, I aimed

i. to identify if and how NompC has its role in epithelial morphogenesis (at the tissue level).
ii. to better understand how NompC is relevant in mechanical communication between cells (at the cellular level).

CHAPTER 2: Materials and Methods

2.1. Materials

2.1.1. Oligonucleotides used in this study

All lyophilized oligonucleotides were manufactured by Eurofins Genomics. ddH_2O is added to dissolve and store the oligonucleotides with a 100 pmol/µl concentration at -20˚C.

Table 1: List of oligonucleotides used in this study

Oligo name	Sequence 5'→3'	Description
ARC1	GTTTCTGAGTCGGAGTTTGTGT	Forward primer for the 5' flanking region of *nompC*
ARC2	CAAACCAGCTTGCAGTTACTAAG	Reverse primer for the 3' flanking region of *nompC*
ARC3	GTGAGCAAGGGCGAGGAG	*eGFP* forward primer
ARC4	CTTGTACAGCTCGTCCATGC	*eGFP* reverse primer
ARC5	GTGACCACCAATGTAGGTG	Forward primer for the *nompC* gene-specific sequence
ARC6	CTTCGTCCTCGAGGAGTTG	Reverse primer for the *nompC* gene-specific sequence
ARC7	CACGAGTTCGAGATCGAGG	*mTomato* forward primer
ARC8	GAAGGACAGCTTCTTGTAATC	*mTomato* reverse primer
ARC10	TAGTAGATCTGCTAGGCCGGCCTATGGAGCTGGTG	*Sqh* promoter reverse primer for infusion
ARC11	CAGCGCCCTTTGGGAGTTCA	Colony PCR reverse primer for *Sqh* promoter
ARC12	GTACTCCACGAATTCTGGTAGCACAACTGACAATA	*Sqh* promoter forward primer for infusion
ARC13	GAGGCGCGCCGGTACAGCAGTCGATTCACTAGC	Sqh-3' UTR forward primer for infusion

ARC14	CATTATACGAAGTTATGTCTAGAGTTTGATCAGTTGC	Sqh-3' UTR reverse primer for infusion
ARC15	GAGAGCGAAACTCCCATACG	Colony PCR forward primer for *Sqh-3' UTR*
ARC16	CAAATGCGCGGATAAGTAC	Colony PCR reverse primer for *Sqh-3' UTR* and *eGFP-VinD1*
ARC17	CATGACGTACCTACCTCGAC	Sequencing oligo for pattB-GMR-*SqhP-Sqh3'UTR*
ARC18	TAGGCCGGCCTAGCAATGGGCAACAAATGCTGCAGC	*Myr-GCaMP7s* forward primer for infusion
ARC19	GAATCGACTGCTGTATTACTTCGCTGTCATCATTTG	*Myr-GCaMP7s* reverse primer for infusion
ARC20	CGATTTTCAACGGACCCCG	Colony PCR reverse primer for *Myr-GCaMP7s*
ARC21	GCTGCAATGGGTTCTCATC	Sequencing oligo for pattB-GMR-*SqhP-myr-GCaMP7s-Sqh3'UTR*
ARC22	GTGAAGTTCGAGGGCGACA	Sequencing oligo for pattB-GMR-*SqhP-myr-GCaMP7s-Sqh3'UTR*
ARC23	CATAGGCCGGCCTAGCAGGGAATTCATGGTGTCCAAG	*eGFP-VinD1* forward primer for infusion
ARC24	GAATCGACTGCTGTACTAGAGGTACCCTCGAGCTAC	*eGFP-VinD1* reverse primer for infusion
ARC25	CGCCCATTTTAGGCAATGGC	Sequencing oligo for pattB-GMR-*eGFP-VinD1-Sqh3'UTR*
ARC26	CATGGTGCTGCTGGAGTTCG	Sequencing oligo for pattB-GMR-*eGFP-VinD1-Sqh3'UTR*
ARC27	GCTGGTGCAGTTCCTCAAGG	Sequencing oligo for pattB-GMR-*eGFP-VinD1-Sqh3'UTR*; and colony PCR forward primer for *eGFP-VinD1*

ARC43	CGTACTCCACGAATTGGCTTGCTGTTCTTCGCGTTC	*Ubi* promoter forward primer for infusion
ARC47	GTGTTTTAAAAGTGTGATGTG	Colony PCR reverse primer for *Ubi* promoter
ARC50	TTGCATGCAAGAATTCTGGATTATTCTGCGGGCAGA	*Ubi* promoter reverse primer for infusion
ARC51	GAATAATCCAGAATTATGGGCAACAAATGCTGCAGC	*myr* forward primer for infusion
ARC52	TTGCATGCAAGAATTCTGCAGCCGCAGATCTACCGG	*myr* reverse primer for infusion
ARC53	GAATAATCCAGAATTATGGGCAACAAATGCTGCAGC	*GCaMP8s* forward primer for infusion
ARC54	TTGCATGCAAGAATTTTACTTTGCGGTCATCATTTG	*GCaMP8s* reverse primer for infusion
ARC55	CCGAAGGTATATAAACAGCG	Sequencing oligo for pattB-GMR-*UbiP*
ARC56	GGTTAATAGGGGTTTCTCAAC	Colony PCR forward primer for *myr*; and sequencing oligo for pattB-GMR-*UbiP-myr*
ARC57	GCAGCCGCAGATCTACCGG	Colony PCR forward primer for *myr*
ARC58	CGTTGACATCATCAGACCAC	Colony PCR forward primer for *GCaMP8s*; and sequencing oligo for pattB-GMR-*UbiP-myr-GCaMP8s*
ARC59	GTCCAACTCCACCAAAATCG	Colony PCR forward primer for *GCaMP8s*
ARC60	CTGGGACACAATCCTACTGA	Sequencing oligo for pattB-GMR-*UbiP-myr-GCaMP8s*
DK49	CAGGTAATGAATTGCCGCGG	Colony PCR forward primer for *SqhP*, *UbiP*, *GCaMP8s*; Sequencing oligo for *SqhP*, *UbiP*

DK59	GGTTGATTTCAGTAGTTGCAG	Colony PCR reverse primer for *SqhP*, *UbiP*, *GCaMP8s*; Sequencing oligo for *SqhP*, *UbiP*
CB1139	CAGACAATCGGCTGCTCTGA	*Frt* (neomycin) forward primer
CB1140	AAAAGCGGCCATTTTCCACC	*Frt* (neomycin) reverse primer

2.1.2. Instruments used for PCR, nucleic acid quantitation, gel electrophoresis and imaging

Biometra Tadvanced (Analytik Jena GmBH, Germany)

NanoPhotometer NP80 (Implen, Germany)

EC Electrophoresis Dual Power Supply EC 135-90 (Thermo Scientific)

UV transilluminator Biometra TI 1 (Biometra, Germany)

UVP GelSolo Simplified UV Gel Documentation System (Analytik Jena, Germany)

2.1.3. Antibodies used in this study

Table 2: List of primary antibodies

Antibody against	Raised in	Working concentration for staining	Source
DCAD1 (α-catenin)	rat	1:200	Tadashi Uemura
Armadillo (ß-catenin)	mouse	1:50	Hybridoma centre Iowa
Dlg	mouse	1:100	Hybridoma centre Iowa
α-tubulin	mouse	1:5000	Sigma T5168
GFP	Chicken	1:1000	Abcam

RFP	Chicken	1:1000	Abcam

Table 3: List of secondary antibodies

Antibody against	Raised in	Working concentration for staining	Source
Mouse primary antibody	Goat	1:500	Invitrogen
Rabbit primary antibody	Goat	1:500	Invitrogen
Rat primary antibody	Goat	1:500	Invitrogen

Table 4: List of dyes and nanobodies

Name	Target	Working concentration for staining	Source
Phalloidin	Actin	1:500	Invitrogen
DAPI	DNA	1:250	Sigma
GFP nanobody	GFP	1:500	Invitrogen

2.1.4. Flies used in this study

Table 5: Fly stocks used in this study

Name	Genotype	Source
OrR	*+/+*	Großhans
E-Cad-GFP (Knock-in)	*w; DE-Cadherin-GFP[k-in]; +/+*	(Huang *et al.*, 2009)
al dp b pr c px sp	*w; al dp b pr c px sp/CyO; +/+*	Großhans
al dp b px^+ sp^+ E-Cad-GFP/Cyo	*w; al dp b px^+ sp^+ DE-Cadherin-GFP[k-in]; +/+*	Ankit
E-Cad-mTomato (Knock-in)	*w; ECad-mTomato {w+} / CyO; +/+*	Großhans
al dp b px^+ sp^+ E-Cad-mTomato/Cyo	*w; al dp b pr c px s ECad-mTomato {w+}p /CyO*	Ankit
al Bl	*al dp b pr Bl c px sp / SM1*	Großhans
His-GFP	*w ; Histone2Av-GFP{w+}*	Großhans

Tub-Gal4	*w ; tubulin-Gal4{w+}LL7 / TM3, Sb*	Großhans
jGCaMP7s	w; +/+: *UASt-Myr-jGCaMp7s{w+}/ TM3*	J. Troy Littleton
jGCaMP8s	w; +/+: *UASt-Myr-jGCaMp8s{w+}/ TM3*	Adam Matrin
nompC$^{\Delta}$ (Knock-out)	*w; nompC$^{\Delta}$::attP::loxP-3xP3-Ds-Red::loxP/Cyo; +/+* *w; nompC$^{\Delta}$::attP::loxP/Cyo; +/+*	In Droso
Frt^{2L}	*w* ; al dp b pr Frt2L[40A]{neoR, ry+} / CyO, hid{w+}*	S. Luschnig / Münster
nompC$^{\Delta}$ Frt^{2L}	*w;nompC$^{\Delta}$::attP::loxP Frt2L[40A]{neoR, ry+}/Cyo*	Ankit
nompC$^{\Delta}$ Frt^{2L}E-Cad-GFP	*w;nompC$^{\Delta}$::attP::loxP, Frt2L[40A]{neoR, ry+}, DE-Cadherin-GFP[k-in]/Cyo*	Ankit
nompC$^{\Delta}$ Frt^{2L}E-Cad-mTomato	*w;nompC$^{\Delta}$::attP::loxP, Frt2L[40A]{neoR, ry+}, ECad-mTomato {w+}/Cyo*	Ankit
E-Cad-GFP; Moe-RFP	*w; DE-Cadherin-GFP[k-in]; Moe-RFP{w+} / CyO; [ubi-SAS6-GFP, w+] / TM3, Sb*	Großhans Ankit
E-Cad-GFP; Sqh-mCherry	*w; DE-Cadherin-GFP[k-in]; sqhp-Sqh-mCherry {w+}; +/+*	(Martin *et al.*, 2009) Ankit
nompC$^{\Delta}$ Frt^{2L}E-Cad-GFP; Moe-RFP	*w;nompC$^{\Delta}$::attP::loxP Frt2L[40A]{neoR, ry+}/Cyo*	Ankit
nompC$^{\Delta}$ Frt^{2L}E-Cad-GFP; Sqh-mCherry	*w;nompC$^{\Delta}$::attP::loxP, Frt2L[40A]{neoR, ry+}, ECad-GFP/Cyo;]; sqhp-Sqh-mCherry{w+}; +/+*	Ankit
E-Cad-mTomato;Tub-Gal4>jGCaMP7s	*w; ECad-mTomato {w+} / CyO; tubulin-Gal4{w+}LL7, UASt-Myr-jGCaMp7s{w+}/ TM3*	Ankit
E-Cad-mTomato;Tub-Gal4>jGCaMP8s	*w; ECad-mTomato {w+} / CyO; tubulin-Gal4{w+}LL7, UASt-Myr-jGCaMp8s{w+}/ TM3*	Ankit
nompC$^{\Delta}$Frt^{2L}E-Cad-mTomato ;Tub-Gal4>jGCaMP7s	*w;nompC$^{\Delta}$::attP::loxP, Frt2L[40A]{neoR, ry+}, ECad-mTomato {w+}/Cyo; tubulin-Gal4{w+}LL7, UASt-Myr-jGCaMp7s{w+}/ TM3*	Ankit
nompC$^{\Delta}$Frt^{2L}E-Cad-mTomato ;Tub-Gal4>jGCaMP8s	*w;nompC$^{\Delta}$::attP::loxP, Frt2L[40A]{neoR, ry+}, ECad-mTomato {w+}/Cyo; tubulin-Gal4{w+}LL7, UASt-Myr-jGCaMp8s{w+}/ TM3*	Ankit
E-Cad-mTomato; Vinc-D1GFP	*w; ECad-mTomato {w+} / CyO; VinD1-GFP*	Ankit
nompC$^{\Delta}$Frt^{2L}E-Cad-mTomato ;Vinc-D1GFP	*w;nompC$^{\Delta}$::attP::loxP, Frt2L[40A]{neoR, ry+}, ECad-mTomato {w+}/Cyo; VinD1-GFP*	Ankit
nompC-eGFP	*w; nompC-eGFP CRISPR{EGFP}/CyO*	Well Genetics
Tft/CyO	*w ; Tft, c px sp / CyO*	Großhans
Sp/CyO; Dr/TM3	*w; Sp/CyO; Dr/TM3*	Großhans
Gla/CyO,twi>GFP	*w[1118]; In(2LR)Gla, wg[Gla-1]/CyO, P{w[+mC]=GAL4-twi.G}2.2, P{w[+mC]=UAS-2xEGFP}AH2.2*	BDSC

Sp/CyO,twi>GFP; Dr/TM3	*Sp/CyO,twi>GFP; Dr/TM3*	Ankit
ovoD^{2L}	*y w hs-Flp [122]; ovoD Frt2L [40A] / Cyo, hs-hid {w+}; +/+; +/+*	S. Luschnig / Münster
PhiX86Fb	*P{ry[+t7.2]=hsp70-flp}1, y[1] w[*]; +/+; M{3xP3-RFP.attP}ZH-86Fb; M{vas-int.B}ZH-102D; +/+*	(Bischof *et al.*, 2007)

2.1.5. Transgenes generated in this study

For transformation, I used commercial Stellar competent cells (Takara, Japan). LB media and antibiotic-added LB plates were prepared according to the following protocol:
https://wwwuser.gwdg.de/~jgrossh/protocols/microbiology/LB-plates.html

Table 6: Plasmids generated during this study

Name	Method used	Source of the insert
pattB-GMR-SqhP	In-fusion (Takara)	SGMCA
pattB-GMR-SqhP-Sqh3'UTR	In-fusion (Takara)	SGMCA
pattB-GMR-SqhP-myr-GCaMP7s-Sqh3'UTR	In-fusion (Takara)	UAS-myr-GCaMP7s
pattB-GMR-SqhP-GFP::VinD1-Sqh3'UTR	In-fusion (Takara)	UAS-GFP::VinD1
pattB-GMR-UbiP	In-fusion (Takara)	pTK23
pattB-GMR-UbiP-myr	In-fusion (Takara)	myr-GCaMP8s
pattB-GMR-UbiP-myr-GCaMP8s	In-fusion (Takara)	myr-GCaMP8s
PCFD5-PE3-nompC^{E1511K}	Gibson Assembly (NEB)	ds-DNAs to insert peg- and sg-RNAs

2.1.6. Reagents

All standard reagents were ordered from Thermo Fischer Scientific (Waltham, USA), Sigma-Aldrich (St. Lois, USA), Merck (Darmstadt, Germany), Invitrogen (Carlsbad, USA), AppliChem GMBH (Darmstadt, Germany) and/or Carl Roth GMBH (Karlsruhe, Germany) unless mentioned otherwise.

2.1.7. Regular fly food and apple juice plate

64 g of agar was cooked and dissolved homogeneously in 7 litres of water. 0.64 g maize meal, 80 g soya-bean meal, 200 g of baker's yeast, 640 g malt extract and 175 g sugar-beet molasses were added to this. The food was properly mixed and cooked for another 30 min. Thereafter the food was cooled to 55 - 60°C. At this stage, 12g Nipagin (dissolved in 90 ml ethanol) and 75 ml propionic acid were added and mixed well into the food. The food was then filled into the vials and covered overnight with a cotton cloth to cool down and solidify at room temperature. Vials were plugged with sponge plugs the next day. Fly food vials were stored at 4°C. Before use, they were warmed to 18°C.

To prepare one litre of apple juice agar, 17.5g agar was dissolved in 750 ml of water. The solution is then autoclaved. After autoclaving, 25 g of sugar and 250 ml of apple juice were added to the solution. Finally, after adding 1.5g of Nipagin (dissolved in 10 ml of ethanol), the mixture was allowed to cool down to 60°C. Apple juice agar was poured into the Petri dishes, and the plates were stored at 4°C. A little bit of fresh yeast is applied on top of the solidified apple juice agar before feeding the flies in a cage.

5.1.8. General buffers

Table 7: List of buffers used in this study

Name	Constitution/Source
PBS	137 mM NaCl, 10 mM Na2HPO4, 2.7 mM KCL, 1.8 mM KH2PO4, [pH 7.4]
PBT	PBS with 0.1% of Tween-20 or TritonX-100
TE buffer	10 mM Tris/HCl (pH 8), 1 mM EDTA
Blocking buffer	5% non-fat milk or 5% BSA

Squishing buffer	Tris-HCl 10 mM (pH 8.2), EDTA 1 mM, NaCl 25 mM, Proteinase K 200 µg/mL
Embryo fixation buffer	4.5 mL PBS, 5 mL Heptane, 0.5 mL Formaldehyde (37%)
Phusion HF buffer (5x)	Thermo Scientific
Green Taq buffer (10x)	Thermo Scientific

2.1.9. Enzymes and commercial kits

Table 8: List of enzymes and kits used in this study

Name	Source
Fast digest restriction enzymes	Fermentas/Thermo Fisher Scientific, USA; New England Biolabs, United States
PfuS mix DNA Polymerase	Expressed and purified in the Großhans lab
Proteinase K	Roche
Taq DNA Polymerase	Expressed and purified in the Großhans lab
In-Fusion® HD Cloning	Macherey-Nagel, Düren, Germany
NucleoBond Xtra Midi kit	Macherey-Nagel, Düren, Germany
NEBuilder HiFi DNA Assembly	New England Biolabs, United States
MiniElute Gel Extraction Kit	Qiagen,Germany

2.1.10. Microscopy

Spinning Disc microscope: Spinning disc microscope (Zeiss AxioObserver.Z1, Laser rack 405, 488, 561, 635 nm, Photometrics Evolve EMCCD camera, AxioCam MRm CCD camera)

Laser scanning confocal microscope:

Laser ablation system: Rapp Optoelectronic (ROE)

Stereomicroscope: SZX9 Olympus GFP fluorescence microscope, Leica Plan 1.0X, Stemi SV6.

Microinjection microscopes: Zeiss PrimoVert with Eppendorf FemtoJet pressure control system

Others: Zeiss Axiophot (Dark-field imaging), Zeiss AxioObserver.Z1 (DIC imaging)

2.1.11. Software

Zen 3.5 (blue edition)

ImageJ

Fiji

Rapp optoelectronic (ROE) [SysCon Version 1.2.0.4]

IMARIS with IMARIS file converter (version 9.7.2)

Implen Nanophotometer® (version 4.0.6)

Microsoft Excel 2013, Microsoft

Microsoft Word 2013, Microsoft

2.1.12. Other items

Table 9: List of miscellaneous materials used in this study

Name	Source
Centrifuge Multifuge 3 S-R Mikro 200R Biofuge fresco	 Heraeus, Germany Hettich Zentrifugen, Germany Haraeus, Germany
QualexGold Agarose	AGS GmbH
Aquapolymount	Polysciences Inc., USA
Coverslips	Thermo Fischer, Braunschweig, Germany
Fly vials	Greiner, Kremsmünster, Austria

PCR tubes	PCR tubes
DanKlorix	
DNA ladder (1 kb)	Thermo Scientific
dNTPs	Thermo Scientific
Falcon tubes (15 ml, 50 ml)	BD Falcon
Formaldehyde (37%)	Sigma-Aldrich, Th. Geyer GMBH
Glass pipettes (5 ml – 25 ml)	Silber Brandt
Halocarbon oil 700	Sigma-Aldrich
Immersol 518F/W	Zeiss
Microinjection needles TW100F-4	WPI, Science Products GMBH
Parafilm M	Bemis
Pasteur pipettes	Brandt
Petri dishes	Greiner
Yeast	Dr. Oetker
Aquapolymount	Polysciences Inc.

2.1.13. Laboratory services

Eurofins Genomics

Microsynth SeqLab

InDroso

WellGenetics Inc.

2.2. Methods

2.2.1. Fly methods

2.2.1.1. Fly culture and crossing

To raise and breed flies (*Drosophila melanogaster* unless mentioned otherwise), they were kept in big (55 mm) and small (20 mm) food vials. For regular stock keeping, small vials were used. The flies were flipped into a fresh vial at regular intervals (no more than 2 weeks). Each line was maintained in three copies. When needed for experiments, to amplify the flies, they were raised in big vials. The yields of flies in F1 generation in small and big vials are ~60 and ~500, respectively. According to the demand of the experiments, the vials were kept at 18˚C or 25˚C. From egg-laying to ecclosion, it takes ~3 weeks at 18˚C and ~10 days at 25˚C (generation time). Adding a little bit of dry yeast to the food increases the yield significantly. To prevent the food's desiccation, the humidity of the incubator rooms was set to ~60%, and the boxes were closed with a lid.

To set up a cross, virgin female flies were crossed with appropriate males with desirable genotypes. Since females may store sperms over several weeks, it is absolutely required for controlled crosses to separate newly ecclosed male and female flies before they mate. To collect the virgin females, the vials with ecclosing flies were kept at 18˚C overnight and 25˚C during the daytime. Virgins were identified by the presence of green meconium in their abdomen and collected multiple times per day.

For collecting embryos for experiments, flies were mated in cages and allowed to lay eggs on apple juice plates. For small cages, the plates were changed once per day. Collecting embryos for microinjection needs a large number of synchronised embryos. In this case, large cages (95mm) were used, and the plates were changed every 30 mins multiple times daily.

2.2.1.2. UAS-Gal4 system

The UAS-Gal4 system facilitates the facultative expression of a gene of interest in a chosen tissue or the whole organism. Flies expressing the gene of interest under the control of the upstream activation site (UAS) were crossed with flies expressing Gal4 driver under the control of a known protomer. Yeast transcription factor, Gal4 binds with the UAS allowing the activation and expression of the target gene. This approach was used to express the GCaMP7s gene in AS tissue and the whole fly.

2.2.1.3. Meiosis recombination

Recombining two or more genes in a single chromosome allows simultaneous ectopic gene expression. *nompC$^{\Delta}$* (K-in) was crossed with flies carrying recessive markers on the second chromosome (al dp b pr Bl c px sp/SM1). The heterozygous females were then crossed with al dp b pr c px sp/SM1. The $al^{+}dp^{+}$ males of the F1 generation were collected and crossed with *Frt^{2L}*(neomycin) flies containing the same recessive markers. The stable recombinant lines were established by crossing single male flies expressing *nompC$^{\Delta}$*, *Frt^{2L}* with Tft/CyO. Subsequently, *Ecad-GFP* (K-in) was similarly recombined together with *nompC$^{\Delta}$* and *Frt^{2L}* on the second chromosome. The meiosis recombination approach was also used for combining *Tub-Gal4* and *UAS-GCaMP7s* on the third chromosome.

2.2.1.4. Generating germline clone

Germline clones were generated according to Chou and Perrimon's protocol with minor modifications (Chou and Perrimon, 1996; Perrimon, 1984). The induction of flippase was achieved by heat-shocking the first-instar larvae at 37˚C for an hour per day for two consecutive days (48 and 72 hours after hatching).

2.2.1.5. Cuticle preparation

~100 mutant embryos were nicely arranged in rows and columns in an apple juice agar plate and were kept at 25˚C for 48 hours. After 48 hours, only the unhatched embryos were collected. The embryos were transferred into a net where they were washed, dechorionated with 50% Klorix and thoroughly washed with water. Dechorionated embryos were then gently transferred with a fine brush to a drop of the mixture of Hoyer's medium and lactic acid on a clean slide. The embryos were mounted with a clean coverslip and left at 65˚C overnight. Some weight is applied on the coverslip to press the sample. Images were acquired with a dark field objective. For WT embryos, before cuticle preparation, I kept them at 25˚C for 20-22 hours.

2.2.1.6. Survival assay

~100 embryos were nicely arranged in rows and columns in an apple juice agar plate and were kept at 25˚C. The distinction between the homo- and heterozygous genotypes were made based on GFP expression. A little bit of dry yeast is added to the agar. Hatched first instar larvae are counted and transferred to a small food vial. The development was followed closely, and the number of pupae and eccolosed adult flies was counted to perform the survival rate analysis.

2.2.1.7. Touch sensitivity analysis

~100 embryos were nicely arranged in rows and columns in an apple juice agar plate and were kept at 25˚C with a regular supply of yeast so that the hatched embryos could develop on the plate. The third instar larvae were collected and transferred to a fresh apple juice place. They were touched with an eyelash at one side of the thoracic segment, and their responses to this stimulus were observed under the dissection microscope. The behavioural responses were scored as follows: 0, no response; 1, pause; 2, recoil or turn; 3,

single reverse contraction; 4, multiple reverse contractions. Each larva was touched four times, and the values were summed up as the final score (Kernan *et al.*, 1994).

2.2.1.8. Embryo Fixation

The flies were allowed to lay embryos overnight on the apple juice plate at 22˚C. The next morning embryos were dechorionated on the plate by adding 50% Klorix for 2 minutes and collected on a net. The net was carefully dipped into a scintillation vial containing 5 ml heptane, 4.5 ml 1x PBS and 0.5 ml formaldehyde (37%) to transfer the embryos into the fixation solution. The embryos were fixed for 20 minutes with constant shaking. Then the formaldehyde was removed, and the embryos were properly washed three times. To this, methanol was added and vortexed vehemently to remove the vitelline membrane. The embryos were transferred to 1.5 ml Eppendorf tubes with methanol and stored at -20˚C until further use for immunostaining. The embryos were fixed with 8% formaldehyde for 1 hour for phalloidin staining. The vitelline membrane was removed manually by a sharp needle. The embryos were collected into PBS and stored at 4˚C until further use for staining. For microtubule staining, the embryos were fixed with 37% formaldehyde. Before immunostaining, these embryos were permeabilised by incubating them in 0.5% TritonX-100 for 2 hours.

2.2.1.9. Immunohistochemistry

Embryos stored in methanol were rinsed three times and washed once for 15 min with 1 ml 1x PBS/0.1% Tween (PBT). Afterwards, embryos were blocked by incubating them in 500 µl PBT containing 5% BSA at room temperature for one hour. Primary antibodies were added to 500 µl of PBT with 1% BSA in their respective dilutions. The embryos were incubated with the primary antibody solution for 2 hours at room temperature or overnight at 4˚C.

The embryos were rinsed thrice and washed four times (15 minutes each with rotation) with 500 µl PBT. All incubations were done under constant rotation. Appropriate secondary antibodies or dyes were diluted in their indicated ratio in 500 µl PBT. Incubation with secondary antibodies and the following washing steps were performed using the same procedure (repeating rinsing and washing steps). Finally, embryos were stained with DAPI (1:250, 0.2 mg/ml) for 5 minutes, rinsed thrice, and washed once for 5 minutes with PBT. Mounting was done by using an Aquapolymount medium.

2.2.1.10. Generation of transgenic flies

Site-specific insertion of transgenes was generated using the attB/phi-C31 system having high integration efficiency. The target plasmid was generated and diluted to 0.1-0.2 µg/µl. Pattb flies (Pattb-86Fb) were amplified in the meantime, and a big cage was prepared with the newly hatched adults. The flies were fed with yeast and kept at 25˚C. The apple juice plates were changed frequently to synchronize the developmental stages of the embryos. Staged pre-blastoderm embryos were collected, dechorionated with 50% Klorix, and washed thoroughly to remove the bleach. The embryos were aligned on a piece of apple juice agar and transferred to a glued coverslip. The embryos were dried for 10 minutes in a desiccation chamber and then covered with 10S voltalef halocarbon oil, allowing embryos to respire. The plasmid was injected using 10x objective. The injected embryos were kept at 18˚C in a humid chamber. The hatched larvae were collected and put into a small food vial. After the adult flies ecclosed, they were crossed with y,w- flies. All the F1 flies with red eyes were collected. A single F1 fly was made to breed with the balancer flies to establish a stock.

2.2.2. Imaging methods

2.2.2.1. Spinning Disc imaging

The flies were let to lay embryos overnight at 22˚C. The next morning, the embryos at stage 12 of development were picked up and dechorionated by treating them with 50% Klorix for 2 mins (with gentle swirling). After dechorionation, the embryos were collected in a net and thoroughly washed to get rid of the bleach completely. Thereafter the embryos were lined on a piece of agar with their dorsal side up, as the amnioserosa is on the dorsal surface. The embryos were transferred to a glued coverslip, and a small drop of halocarbon 10S oil was added to cover them (prevents desiccation, and allows respiration) before imaging. Time-lapse recording was done using the 25x oil immersion objective. Multiple z-stacks (79) were recorded for each timepoint to cover the whole amnioserosa tissue, as it is an ellipsoidal structure in 3D. The interval between two z-stacks was set to 1 μm. The time interval between the two frames was set to 30 s. The movies were recorded for ~2.5 hours, encompassing part of the germband retraction phase, the complete stationary phase and the beginning of the DC phase.

2.2.2.2. Large-scale image segmentation: 'Dynome' analysis

After recording of time-lapse images, all the z-stacks were merged using maximum intensity projection by FIJI. Because of the ellipsoidal topology of amnioserosa, the yolk underlying the tissue hinders the cell junction signal. This leads to erroneous segmentation. To solve this problem, the noise from the yolk was masked using IMARIS and followed by maximum intensity projection. These images were further used for segmentation (described schematically in Figure 3.33).

The tracking of dynamic amnioserosa cells requires a sensitive and fairly accurate segmentation. The number of cells per embryo is ~150. To count all

150 cells over at least 100 time-frames for 10 embryos, add up to 150000 cells. Using Tissue analyzer (TA) for segmenting such long movies yields results requiring a lot of manual correction before analysis. To handle this issue, I collaborated with Matthias Haering (AG Fred Wolf, Dept. of Theoretical Neurophysics, Max-Planck-Institute for Experimental Medicine, Göttingen, Germany), who developed an improved image segmentation approach, known as cycle-GAN (Cycle-consistent generative adversarial networks). This method uses neural-network-based deep machine learning to achieve a significantly higher detection accuracy (more true positives, fewer false positives and false negatives) than TA.

2.2.2.3. Laser-scanning confocal imaging

Laser-scanning microscopy (Zeiss LSM980) was used to record live movies, take images of the immunostained specimens and perform the laser ablation experiments. Settings were adjusted according to the convenience and requirements of the experiments. The Airyscan2 detector was used to adjust sensitivity, resolution and speed. Airyscan processing and deconvolution were used to post-process the images for better resolution.

2.2.2.4. Laser ablation

Junctional recoil can be measured by nano-dissection of single junctions. The flies were allowed to lay embryos overnight at 22˚C. The next morning, the embryos at stages 12-13 of development were picked up and dechorionated by treating them with 50% Klorix for 2 mins (with gentle swirling). Embryos were lined with the dorsal-up orientation on an apple juice agar block and transferred to a 24 mm x 24 mm glued coverslip by pressing them gently against it. Double-sided tape attached the coverslip to a metal holder, and the embryos were kept in a desiccation chamber for ~5 minutes. Thereafter they were immersed in a drop of 10S oil before further imaging at room temperature. The imaging was done with a 63X oil-immersion objective

(NA = 1.4) of Zeiss LSM980 confocal microscope, and all the junction cut experiments were performed with an independent ROE-SysCon-Zen system parallelly associated with the imaging system. The tissue cuts involving bigger lengths were performed with a 40X water-immersion objective. Before tissue cuts, the embryos were dried for ~8-10 minutes. Tissue cuts were meant to isolate AS from the lateral epidermis. The images were obtained from a single z-plane with a time interval of 0.5 s. The ablations were carried out using 4-5% of 355 nm laser power with an exposure time of 150 ms.

The recoil is measured by the displacement of the vertices of the ablated junction from each other. The displacement was manually measured using Fiji/Image J. The curve-fitting of the displacement-time plots was performed based on the Kelvin–Voigt fibre model formula on GraphPad Prism (version 8.1) (Liang *et al.*, 2016).

$$y=(v_i/k)\,(1-e^{-kx})$$

y: displacement, d
v_i: initial recoil velocity
k: viscoelasticity
x: time, t

2.2.2.5. Neighbour cell response assay upon wounding

To measure the area variance of the neighbouring cells after the junction cut, the embryos were prepared in the same manner as described for the junction cut. 5% of 355 nm laser was used to target cell junctions. Two cells sharing their junction were affected due to this cut. The recording was stopped immediately after the ablation. A few z-stacks were set to cover the entire surrounding of the wounding site (all the neighbouring cells of the two affected cells), and the recording was resumed. The area variation of the neighbouring cells was measured after the wounding with a 10 s interval for 15 minutes.

2.2.2.6. Cell wounding

The embryos were prepared following the same protocol used for junction cut experiments. Instead of targeting cell junctions, the 8% laser was pointed in the middle of the AS cells. The intensity of the GCaMP7s of the neighbouring cell junctions was measured with a time interval of 5 s.

2.2.2.7. Particle image velocimetry

The embryos were prepared similarly to prior experiments. The sample was dried for 8 minutes. The imaging was done with a 40X water immersion objective of the LSM980. A 120 μm straight line was drawn in the middle of AS tissue. This length was triggered with a 5% intensity of 355 nm laser. The experiments were carried out with an exposure time of 150 ms, and the imaging was performed at every 1 s interval. The initial recoil was measured using square interrogation windows of 200 pixels sides by PIVLab in MATLAB.

2.2.3. Molecular Biology methods

2.2.3.1. Genomic DNA isolation from single adult fly

A single adult male *Drosophila* was collected in a 0.5 ml Eppendorf tube and kept at -20˚C for 30 minutes. The fly was then smashed as homogeneously as possible in 50 μl of Squishing buffer. Proteinase K was added to the buffer before using it. The fly in the buffer was incubated at 37˚C for 30 minutes. Proteinase K was inactivated by heating it to 95˚C for 2 minutes. The sample was then stored at 4˚C for months to use genomic DNA for PCR amplification.

2.2.3.2. Polymerase chain reaction (PCR)

Taq-polymerase was used for general PCR reactions for amplicon length ~500 bp (like for colony PCR *etc*.). PfuS-based PCR reactions were used for high-fidelity product amplification for molecular cloning *etc*.

Reagents used for Taq-based PCR reaction

Forward primer (0.5 µM)	2 µl
Reverse primer (0.5 µM)	2 µl
dNTP mix (10 mM)	1 µl
10X Green Taq Buffer	5 µl
Taq polymerase	0.5 µl (0.3 U/ µl)
DNA template	50–200 ng
Adjust to 50 µl by ddH_20	

Reagents used for PfuS-based PCR reaction

Forward primer (0.5 µM)	2 µl
Reverse primer (0.5 µM)	2 µl
dNTP mix (10 mM)	1 µl
5X Pfusion Buffer	5 µl
PfuS polymerase	0.15 µl (0.3 U/ µl)
DNA template	50–200 ng
Adjust to 50 µl by ddH_20	

The following program was used for general PCR amplification

Initial denaturation	95˚C	2 min	
Denaturation	95˚C	30 s	25x
Annealing	55–60˚C	1 min	
Extension	72˚C	1 kb/ min (Taq)	
		1 kb/15-30 s (PfuS)	
Final extension	72˚C	10 min	
Pause	4˚C	∞	

2.2.3.3. In-fusion cloning

Site-directed mutagenesis was performed using In-fusion cloning approach. In-Fusion cloning is advantageous as it exploits the power of In-Fusion technology together with inverse PCR, a method facilitating rapid *in vitro* amplification of the DNA sequences flanking a region of a known sequence. The transgenes for this study were generated mostly using In-fusion cloning protocol as described by the manufacturer (Takara).
https://www.takarabio.com/documents/User%20Manual/In/In-Fusion%20HD%20Cloning%20Kit%20User%20Manual_102518.pdf

2.2.3.4. DNA sequencing

DNA sequencing was carried out by the sequencing facility of Microsynth Seq-Lab, Goettingen. The oligos for sequencing were designed and premixed with the plasmid sent for sequencing.

2.2.3.5. Prime editing

Prime editing is a modified version of the classical CRISPR system. I used prime editing to introduce a point mutation, E1511K mutation in the pore forming region of NompC protein. In comparison to homology-directed repair (HDR) and CRISPR/Cas9, prime editing offers reduced genomic mistakes, such as insertion and deletions (indels) at on-target and off-target sites (Bosch and Perrimon, 2022). I designed two ds DNAs containing pegRNA and sgRNA using the PrimeDesign (https://drugthatgene.pinellolab.partners.org/) software.

#dsDNA1 (5'→3')

CGGGTTCGATTCCCGGCCGATGCAGAGAAGAAGAACCGAAATAGGTTTTAGAGCTAGAAATAG
CAAGTTAAAATAAGGCTAGTCCGTTATCAACTTGAAAAAGTGGCACCGAGTCGGTGCAACAAA
GCACCAGTGGTCTAGTGGTAGAATAGTACCCTGCCACGGTACAGACC

#dsDNA2 (5'→3')

AACAAAGCACCAGTGGTCTAGTGGTAGAATAGTACCCTGCCACGGTACAGACCCGGGTTCGAT
TCCCGGCTGGTGCATTTGTCAACTTGCGTTTGCTGTTTTAGAGCTAGAAATAGCAAGTTAAAA
TAAGGCTAGTCCGTTATCAACTTGAAAAAGTGGCACCGAGTCGGTGCGGACAAACGACGACCa
aaCAAACGCAAGTTGTTTTTTGCCTACCTGGAGCCTGAG

I used the Gibson assembly protocol from NEBuilder to generate plasmid (*PCDF-5-PE3-nompCE*^{1511K}) containing both the peg- and sgRNAs. I am currently injecting the plasmid to generate the transgenic flies.

CHAPTER 3: Results

The project was initiated by Dr. Deqing Kong based on his experiments where he observed the expression of mechanosensitive ion channels (Tmc, NompC, Piezo) in AS tissue by expressing GFP-reporter under the control of ion channel promoters. I focused on the NompC channel, being structurally classified and known to interact with microtubules. In this study, I performed all the biological experiments, time-lapse imaging, laser ablations, wounding assays, molecular cloning, fly genetics, FIJI and MATLAB-based quantifications, among many more. The AS movies were segmented via a deep-learning neural network-based segmentation pipeline called Cycle-GAN developed by Matthias Häring (Göttingen Campus Institute for Dynamics of Biological Networks, Georg August University). Large-scale computational analysis (morphodynamic and morphometric) was performed by Dr. Matthias Häring.

3.1. Expression

NompC is expressed in epithelial tissue

I received *nompC-eGFP* (K-in) flies, commercially generated using the CRISPR technique by WellGenetics. They could be maintained as a homozygous stock in our lab. The eGFP is knocked in at the C-terminal end of the construct; see Figure 3.1.

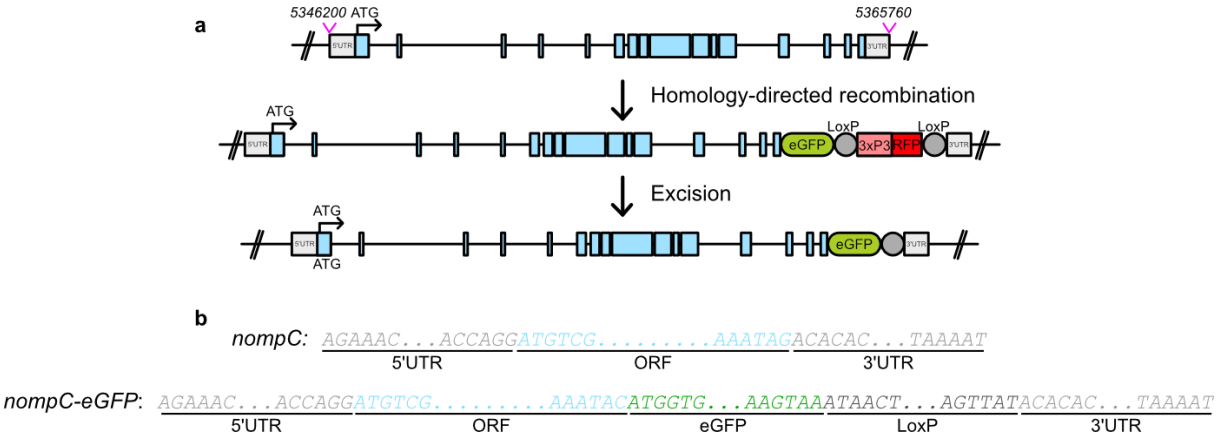

Figure 3.1. Generation of *nompC-eGFP* construct. a.Scheme of CRISPR-mediated insertion of *eGFP-loxP-3xP3 RFP-loxP* at the 3'-end of *nompC* gene. The floxed sequence flanked between two loxP sites

(*loxP-3xP3 RFP-loxP*) was then excised to get *nompC-eGFP* flies. b. DNA sequences of *nompC* and *nompC-eGFP* genes with annotations.

I recorded live images of *nompC-eGFP*-expressing *Drosophila* embryos with 63x oil objective using Zeiss LSM980. I observed bright parallel strips on the epidermal wall of the late-stage embryos, see Figure 3.2.b. These are verily the group of neurons of the chordotonal organ (regulator of locomotion, responsive to vibration stimuli) of *Drosophila*. Other groups previously reported high levels of functional NompC expression in these neurons (schematically shown in Figure 3.2.a). I also detected the expression of NompC in a cluster of cells appearing to be epithelial, see Figure 3.2.b. To understand the expression pattern of NompC in epithelial cells, I looked at the dorsal surface of the embryos undergoing stages 12-13 of development. The dorsal surface consists of two types of epithelial tissue, the amnioserosa (AS) and the lateral epidermis (LE). I detected highly mobile punctate GFP signals from both the tissues (Figure 3.2.c,d) of *nompC-eGFP* embryos but not of w^{1118} (WT) ones, confirming the expression of NompC not only in the neuronal cells but also in the epithelial tissues.

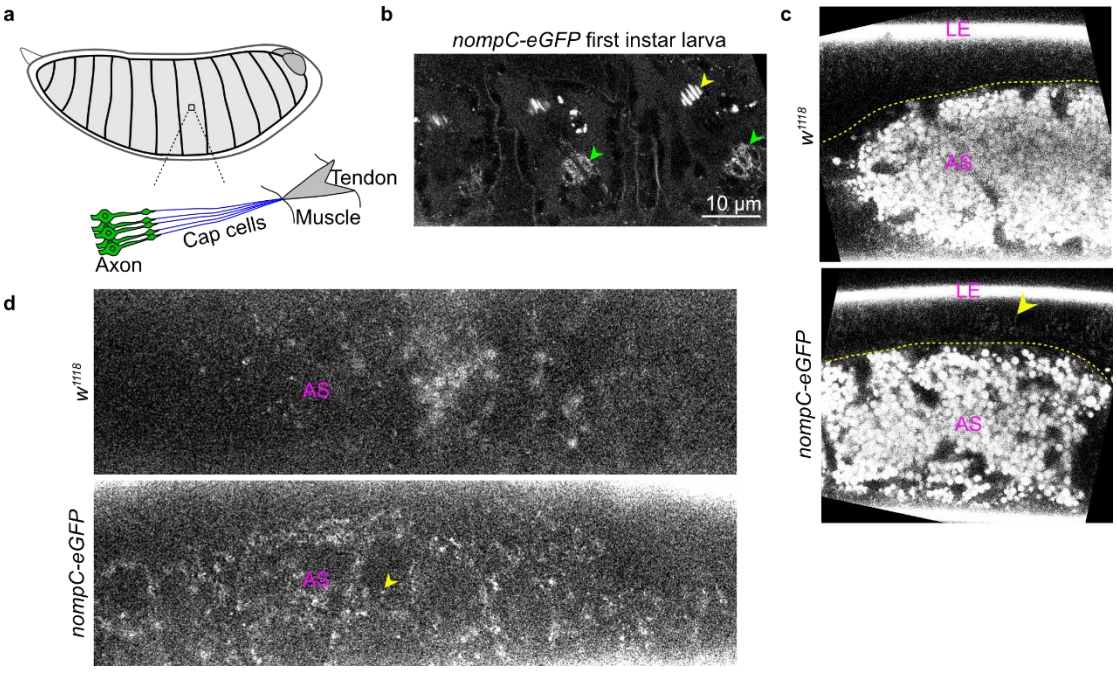

Figure 3.2. NompC is expressed in the epithelial tissues. a. Schematic representation of location and structure of the *Drosophila* chordotonal organ. b. Chordotonal neurons of late-stage *Drosophila* embryos express NompC (indicated by yellow arrowheads), as detected by the GFP signal from the NompC-GFP

fused proteins. Apparently, a group of epithelial cells also express the protein (green arrowheads). c. LE from stage 13 embryos exhibits GFP signals (yellow arrowheads). The strong signal from the AS indicates autofluorescence from the yolk cells. d. AS cells express punctate GFP signals quite distinctly. These punctae are highly dynamic in nature.

I went on to classify the nature of NompC molecules in AS cells, as these cells are highly dynamic and experience a lot of mechanical forces, which may need mechanosensory proteins to get transduced across cells. I marked the cell junctions with E-cadherin-mTomato. I could detect the GFP signals from the apical domain and also along the adherens junctions, see Figure 3.3.a. As the cells and the proteins were highly dynamic, there was a time lag in imaging between the two channels. However, the GFP signals detected along the junctions tend to form stable clusters, see Figure 3.3.b. We know that the clustering of four NompC subunits together builds a functional ion channel.

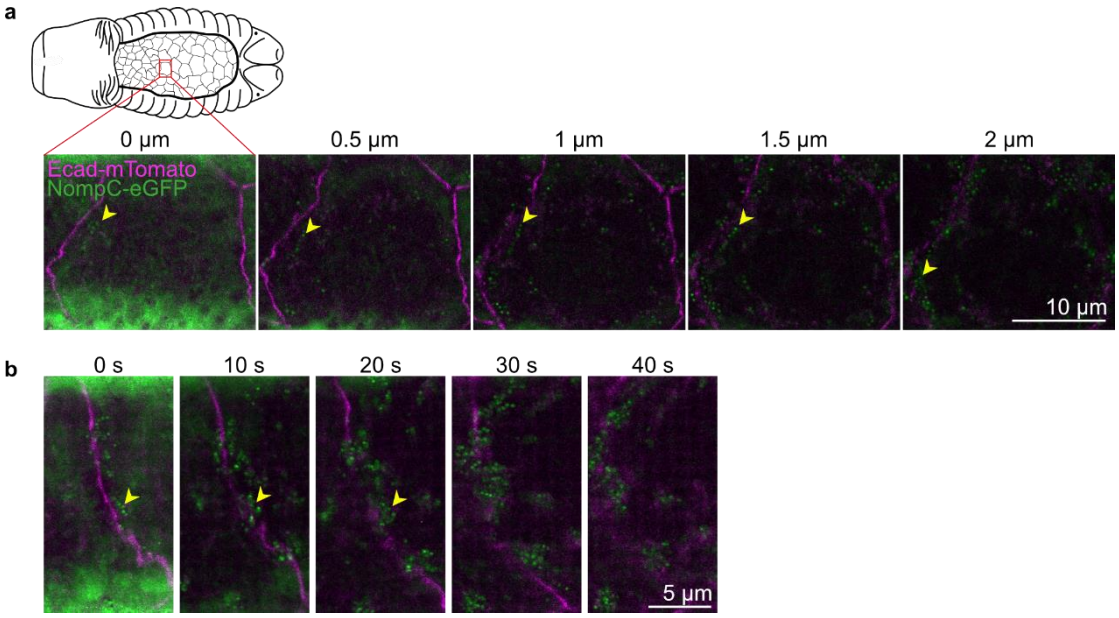

Figure 3.3. Highly mobile NompC clusters are expressed in AS tissue. a. z-stacks with 0.5 µm interval show a broad span of distribution of NompC proteins from the very apical surface to the depth even below the adherens junctions. b. A time-lapse of the maximum intensity projected single AS cell junction with an interval of 10s. The cells are dynamic and hence, susceptible to moving beyond the set focus. Yellow arrowheads indicate NompC clusters.

I then attempted to know the localisation of the molecules in the AS cells. When I fixed the embryos with 4% formaldehyde and stained the embryos with GFP antibody, I could not detect conspicuous other than dispersed signals from the cells, see Figure 3.4.a. 4% formaldehyde was insufficient to maintain the Tubulin structure. On the other hand, when I fixed the embryos with 37% formaldehyde, I could preserve the microtubule cytoskeleton and observe distinct signals from the cortex, especially along the cell junctions, see Figure 3.4.a. This could be because NompC proteins interact with microtubules in the cytoskeleton. Figure 3.4.c highlights the distribution of the GFP signals across the z-stacks starting from the cortex.

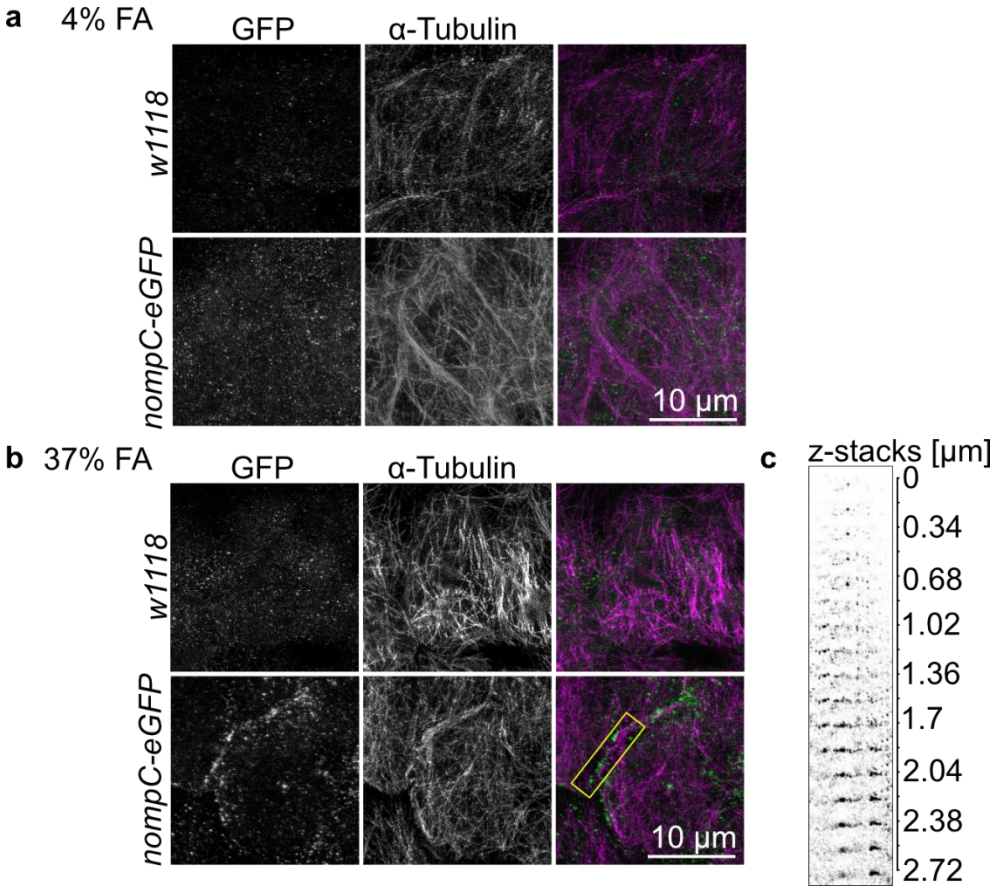

Figure 3.4. Detection of cellular localisation of NompC signals depends on the staining procedure. a. 4% formaldehyde staining did not preserve the microtubules. Also, I could not detect localised GFP signals in the AS cells. b. 37% formaldehyde staining preserved the microtubule structures. In the *nompC-GFP* embryos, I detected GFP signals along the cell borders, though not uniformly across the

tissue. The images were generated after airy-scan postprocessing (dispersed=45) with deconvolution. c. z-stacks showing the depth-wise distribution of the distinct GFP clusters.

3.2. Genetics and phenotypes

Generation of *nompC*-knockout germline clones to get maternal and zygotic null embryos

The mutant variants of *nompC* include three nonsense (*nompC*^{1}, *nompC*^{2}, *nompC*^{3}) and one missense mutation (*nompC*^{4}), see Figure 3.5.a. None of the mutants shows absolute embryonic lethality except the germline clones of *nompC*^{4}. This could be because *nompC*^{4} had a second site hit or it was an antimorphic allele. All the mutants abolish or reduce mechanoreceptor currents in the adult fly bristles. To investigate the role of NompC in *Drosophila*, if at all, I worked with CRISPR knock-out *nompC* (*nompC*$^{\Delta}$) generated in association with InDroso. The entirety of the *nompC* gene had been replaced by *attP-loxP*, see Figure 3.5.b.

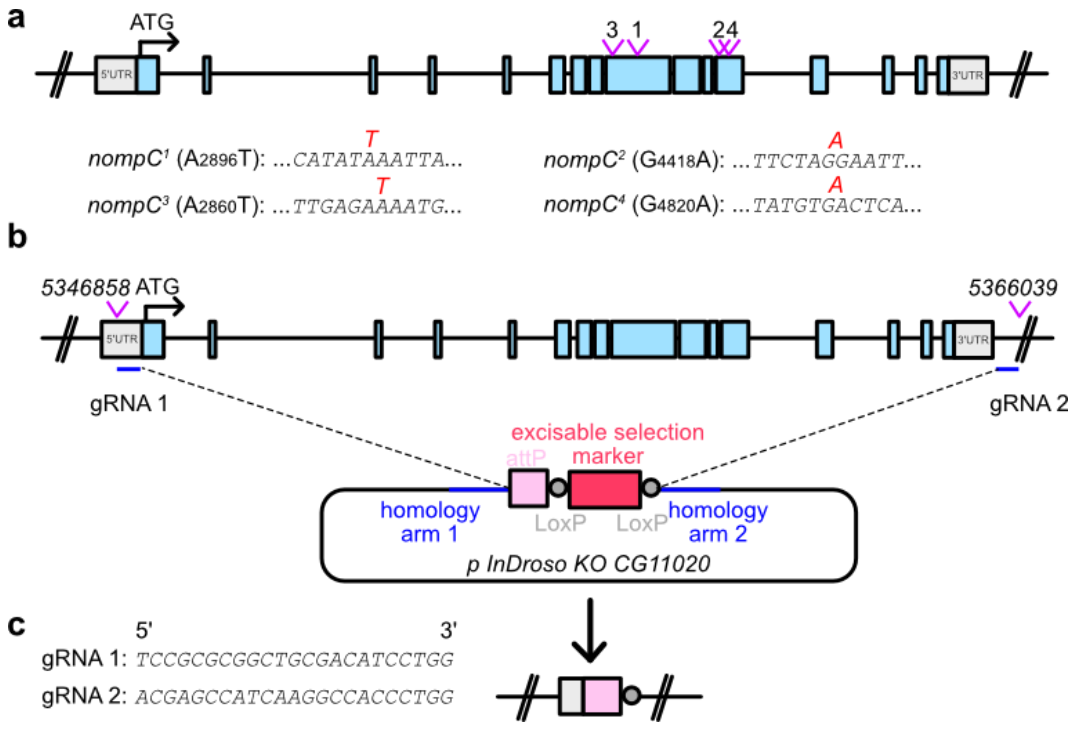

Figure 3.5. Generation of *nompC*$^{\Delta}$ (KO) transgenic flies. a. Four point mutations at the *nompC* locus. b. CRISPR-mediated deletion of nompC locus and simultaneous insertion of attP-loxP is shown schematically. c. Sequence of the gRNAs used for the CRISPR knock-out from nt 5346858 – 5366039.

All the adult flies were only heterozygous when raised as stock in laboratory conditions. The homozygous flies seemed not to survive until the adult stage. Hence, getting embryos devoid of maternal (m) and zygotic (z) contributions of the NompC protein is impossible. To get $m^{-/-}z^{-/-}$ embryos, I generated germline clones based on the method described in the previous section. To facilitate the recombination while generating the germline clones, I recombined *Frt* in the second chromosome alongside *nompC$^{\Delta}$*. I also recombined Ecad-GFP on the second chromosome to serve cell imaging purposes, see 3.6.a. The $m^{-/-}z^{-/-}$ embryos were distinguished from the $m^{-/-}z^{+/-}$ ones by the Twist-driven expression of GFP, as shown in Figure 3.6.b. These embryos were used for survival rate and cuticle phenotype assessment.

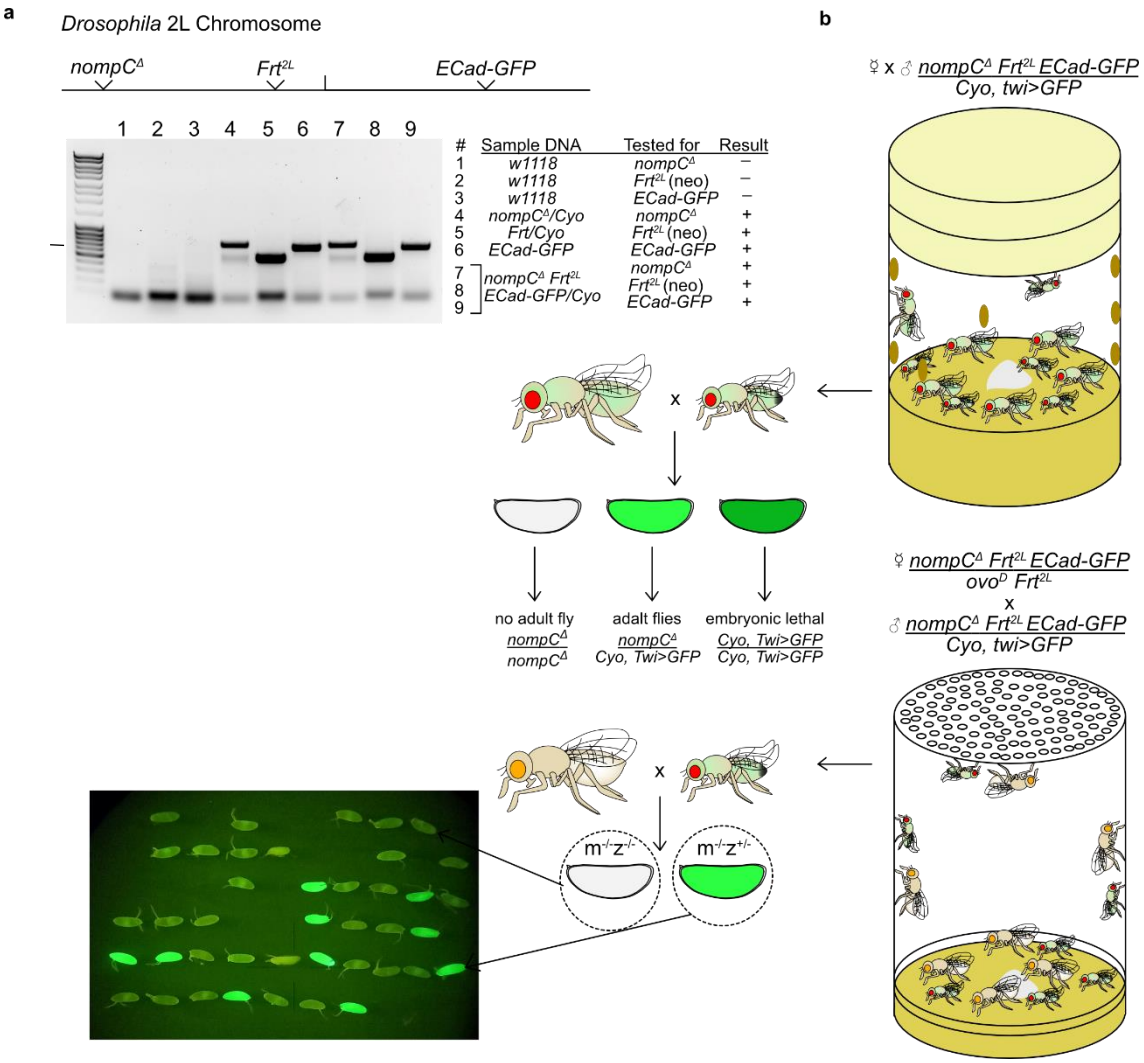

Figure 3.6. Scheme of generating germline clones of *nompC$^{\Delta}$*. a. PCR confirming incorporation of *nompC$^{\Delta}$*, *Frt^{2L}* and *Ecad-GFP* in the second chromosome of *Drosophila* (Ladder: Thermo Fischer,

SM0403). b. Because in laboratory conditions, heterozygous flies are the only adult survivors, the embryos can never be free of NompC. Maternal contribution still remains. Females of germline clones are somatically heterozygous, but their primordial germ cells are homozygous for the gene *nompC$^{\Delta}$*. c. The embryos were arranged in rows and columns on a fresh apple juice agar plate. Under the GFP fluorescence microscope, the $m^{-/-}z^{-/-}$ embryos were distinguished from the $m^{-/-}z^{+/-}$.

nompC$^{\Delta}$ flies are developmentally slowed down and have a significantly lower survival rate

I closely observed the *nompC$^{\Delta}$* embryos for the whole development span from embryos to adult flies. I compared $m^{-/-}z^{-/-}$, $m^{-/-}z^{+/-}$, and OrR (as WT control). The development process takes longer in *nompC$^{\Delta}$* ($m^{-/-}z^{-/-}$) flies. For OrR and *nompC$^{\Delta}$* ($m^{-/-}z^{+/-}$), the time from egg-laying to ecclosion was ~10 days at 25˚C, whereas *nompC$^{\Delta}$* ($m^{-/-}z^{-/-}$) formed pupae only after two weeks. I observed ~31% larval lethality (lethal larvae/hatched larvae) in *nompC$^{\Delta}$* ($m^{-/-}z^{-/-}$).

The rest of the larvae went on to form pupae. I observed ~54% pupal lethality (lethal pupae/total pupae). In summary, only ~38% of adult flies ecclosed out of all the hatched larvae, see Figure 3.7.a,b.

a

Genotype	laid embryos	hatched embryos	Pupae	Adult
w^{1118}	115	115	115	115
nompC$^{\Delta}$ ($m^{-/-}z^{+/-}$)	98	98	98	96
nompC$^{\Delta}$ ($m^{-/-}z^{-/-}$)	95	92	63	35

b

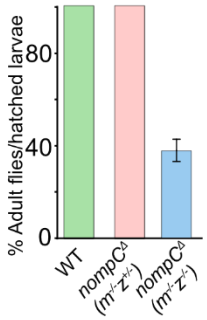

3.7. *nompC$^{\Delta}$* flies have a lower survival rate. a. Table showing the total number of embryos analysed in three replicates. The embryos were aligned in a tabular form on apple juice agar plates. b. Only ~38% of adult flies ecclosed out of all the hatched larvae. Most of the flies died during the larva or pupal stage of development. (Data presented as Mean±SD)

The *nompC*$^{\Delta}$ ($m^{-/-}z^{-/-}$) larvae had severe locomotion defects with complete curling phenotype, see Figure 3.8.a. All the escaper adults were, in fact, unable to walk or fly, see Figure 3.8.b. This indicated that, in laboratory conditions, when the homozygous and heterozygous flies were raised together in the same food vial, the heterozygous flies outcompeted the weaker homozygous ones.

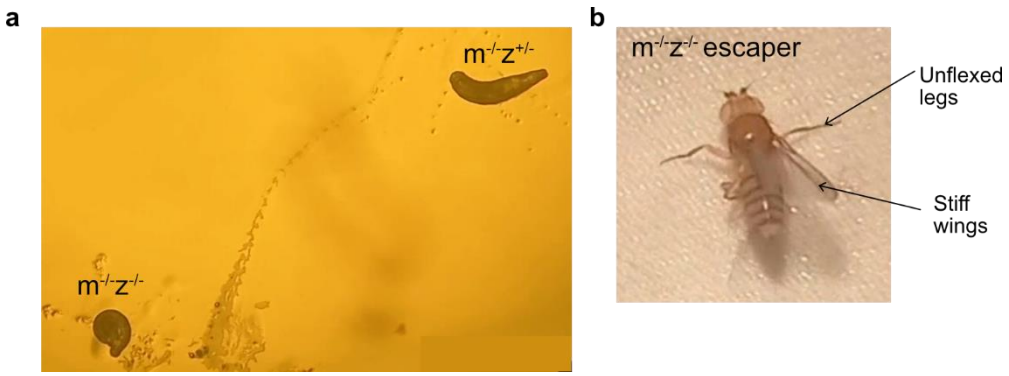

Figure 3.8. *nompC*$^{\Delta}$ ($m^{-/-}z^{-/-}$) flies have defective locomotion. a. *nompC*$^{\Delta}$ ($m^{-/-}z^{-/-}$) larvae showed loss of directionality and curling around the body phenotype. b. *nompC*$^{\Delta}$ ($m^{-/-}z^{-/-}$) escaper adult flies exhibit uncoordinated locomotion, impaired or no movement, and no flight activity, making them susceptible to sticking to food.

nompC$^{\Delta}$ larvae are touch-insensitive

NompC has been described to confer gentle touch sensitivity in Drosophila (Yan *et al.*, 2013). To test if the absence of NompC leads to the impairment of touch responses, I performed nociception scoring with the larvae following the protocol described in Figure 3.9.a. The larvae lost their reflex to gentle touch stimuli to a great degree, see Figure 3.9.b.

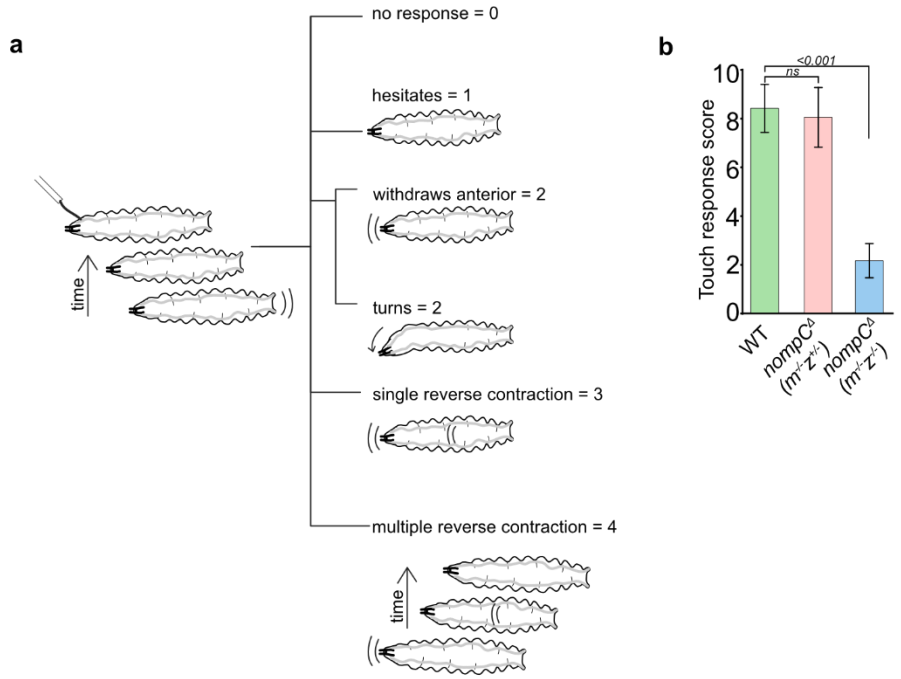

Figure 3.9. The absence of NompC leads to touch-insensitivity in *Drosophila* larvae. a. The protocol and scoring method are summarised. b. There was no difference between WT (OrR) and *nompC*$^{\Delta}$ ($m^{-/-}z^{+/-}$). However, the double-null *nompC*$^{\Delta}$ ($m^{-/-}z^{-/-}$) larvae showed significantly reduced touch response. (WT, N= 60; *nompC*$^{\Delta}$ ($m^{-/-}z^{+/-}$), N=44; *nompC*$^{\Delta}$ ($m^{-/-}z^{-/-}$), N=56; Statistical significance was calculated by Student's t-test) (Data presented as Mean±SD)

nompC$^{\Delta}$ embryos showed cuticle defects

Cuticle is the insect's exoskeleton, produced by the secretion of the epidermal cells. Cuticle phenotypes often reflect developmental anomalies due to a mutation. I analysed the cuticles of the unhatched *nompC*$^{\Delta}$ ($m^{-/-}z^{-/-}$) embryos. They showed a range of cuticle defects, including disorganised denticles, head malformation and holes in the cuticles. This shows perturbed epithelial integrity in the unhatched NompC-depleted embryos, see Figure 3.10.

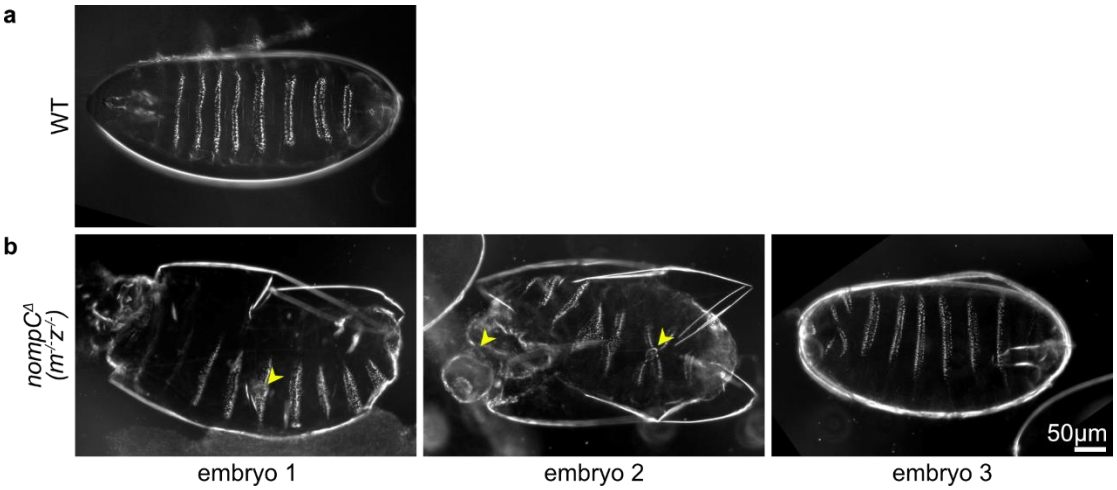

Figure 3.10. Cuticle phenotype in embryos. a. ~20-22 hours old w^- (WT) and unhatched embryo. b. three unhatched *nompC*$^{\Delta}$ ($m^{-/-}z^{-/-}$) showing cuticle phenotypes. Yellow arrowheads indicate cuticle holes, defective head skeletons, and improper denticle patterns.

nompC$^{\Delta}$ embryos displayed no visible germband extension defects

Which stage of embryonic development was affected was still an open question. In order to address that, I recorded time-lapse DIC images of early *Drosophila* embryos. The DIC movies encompassed four critical morphogenetic events, cellularisation, germband extension, germband retraction and dorsal closure.

I measured the time taken for the germband to extend ~2 times to reach the cephalic furrow. The span was comparable in *nompC*$^{\Delta}$ ($m^{-/-}z^{-/-}$), *nompC*$^{\Delta}$ ($m^{-/-}z^{+/-}$) and WT (Ecad-GFP) embryos, see Figure 3.11.a,b. In one of the 13 *nompC*$^{\Delta}$ ($m^{-/-}z^{-/-}$) embryos imaged, I found an incomplete germband extension phenotype, culminating in the death of the embryo, see Figure 3.11.c. However, I did not go into the cellular detail to check if the neighbour cell exchange via T1 transitions were similar to the WT.

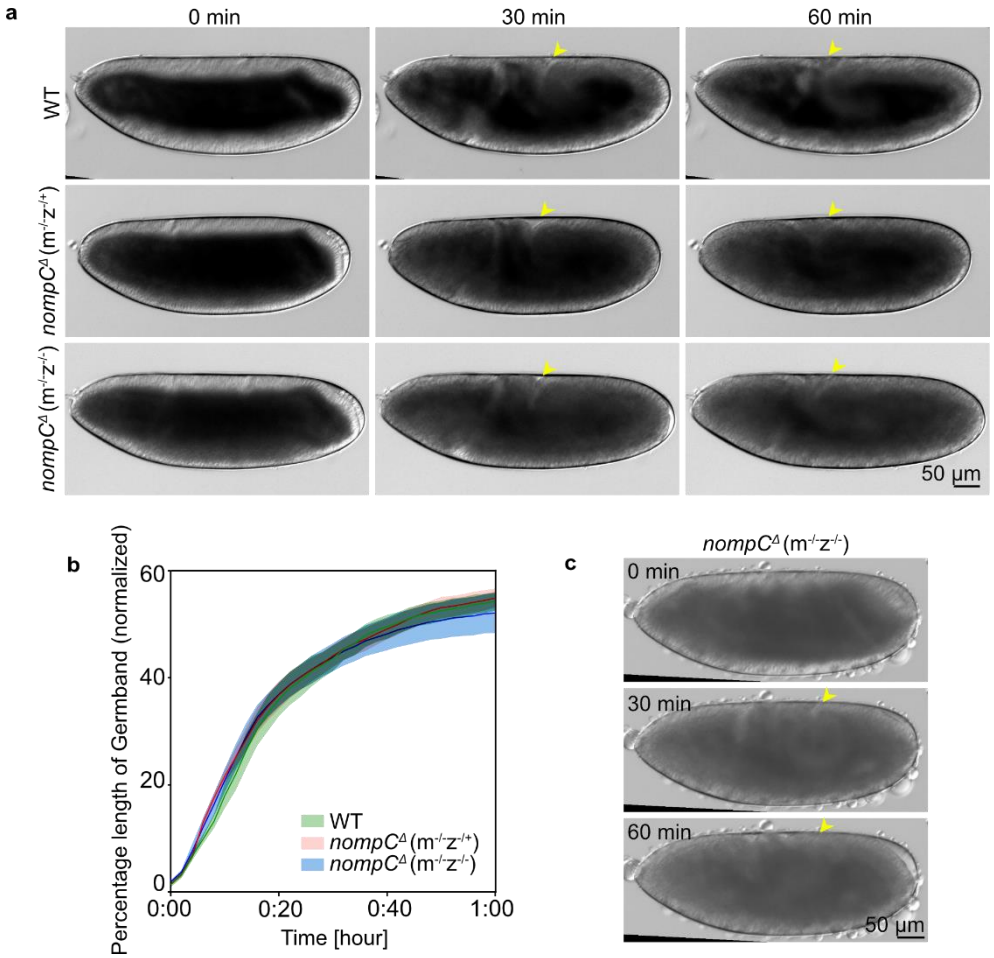

Figure 3.11. The germband extension has no visible changes in the absence of NompC. a. Snapshots from different time points of germband extension. I measured the distance traversed by the germband in an interval of 2 minutes between each frame. b. A displacement-time curve showing how the germband extends to cover more than 50% length of the embryo. c. The example where the germband stopped migrating after half an hour. The embryo failed to develop any further, as expected. If not otherwise denoted, $m^{-/-}z^{-/-}$ embryos are denoted simply as *nompC*$^{\Delta}$ for the rest of the content.

nompC$^{\Delta}$ embryos exhibited dorsal closure phenotype

Next, I tested if the absence of NompC affects the latter morphogenetic events. To do so, I recorded movies covering the entire stages 12, 13 and 14 (encompassing the period from germband retraction to dorsal closure) of the embryonic development of *Drosophila*. I used the 25 x oil immersion objective of the spinning disc microscopy to record the movies. The cell junctions were marked with Ecad-GFP.

I observed critical morphogenetic defects during both the germband retraction and dorsal closure phases. I found the germband retraction incomplete, and during the closure, the AS cells were uncommonly stretched, no/ectopic canthi formed, followed by a dramatic tissue rupture instead of closure. Figure 3.12 summarises a few main snapshots of events and compares them with the WT (Ecad-GFP) counterparts.

After the germband retraction, the AS becomes elliptical, and the anterior end of the tissue remains open. With time, the length of this open-end shortens as the actin cables separating the lateral epidermis of both sides from the AS approach close to each other until they converge at the anterior end of the tissue. This convergence marks the beginning of the dorsal closure. To better understand the anomalous DC phenotype, I quantified the convergence speed. *nompC$^{\Delta}$* embryos had significantly less span of elliptical phase. They tend to enter the DC faster than the WT, see Figure 3.13.b,c. However, the width (maximum distance across the middle) of the AS tissue in the *nompC$^{\Delta}$* embryos increased compared to that of the WT, see Figure 3.13.e. Figure 3.13.f represents the number of AS cells for each embryo at a specific time point in the DC phase. The increased number of cells matches the increased width of the AS tissue. However, the average AS cell area of the WT embryos was smaller compared to the *nompC$^{\Delta}$* embryos during the entire period of elliptical phase.

Taken together, the results indicate anomalous coordination between morphogenetic events due to the loss of NompC.

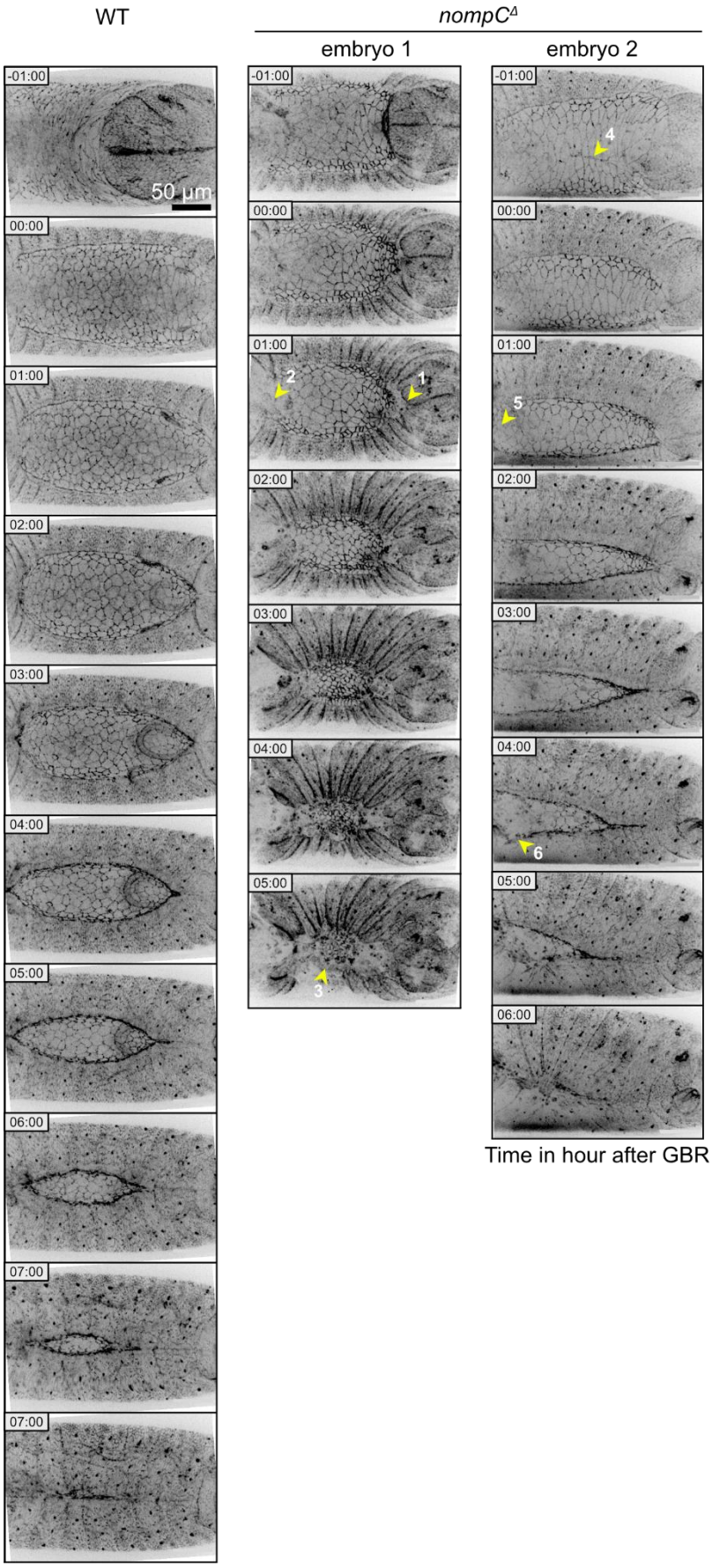
WT
nompC^Δ
embryo 1
embryo 2
-01:00
50 μm
00:00
01:00
02:00
03:00
04:00
05:00
06:00
07:00
1
2
3
4
5
6
Time in hour after GBR

Figure 3.12. Defects in dorsal closure of *nompC$^{\Delta}$* mutant embryos. NompC-depleted embryos exhibited 1. incomplete germband retraction, 2. No formation of anterior canthus, 3. Rupture of AS tissue from the lateral epidermis, 4. Uncommonly elongated cells failed to retract with the germband, 5. No canthae, 6. Formation of ectopic canthus. Ecad-GFP marked the junctions.

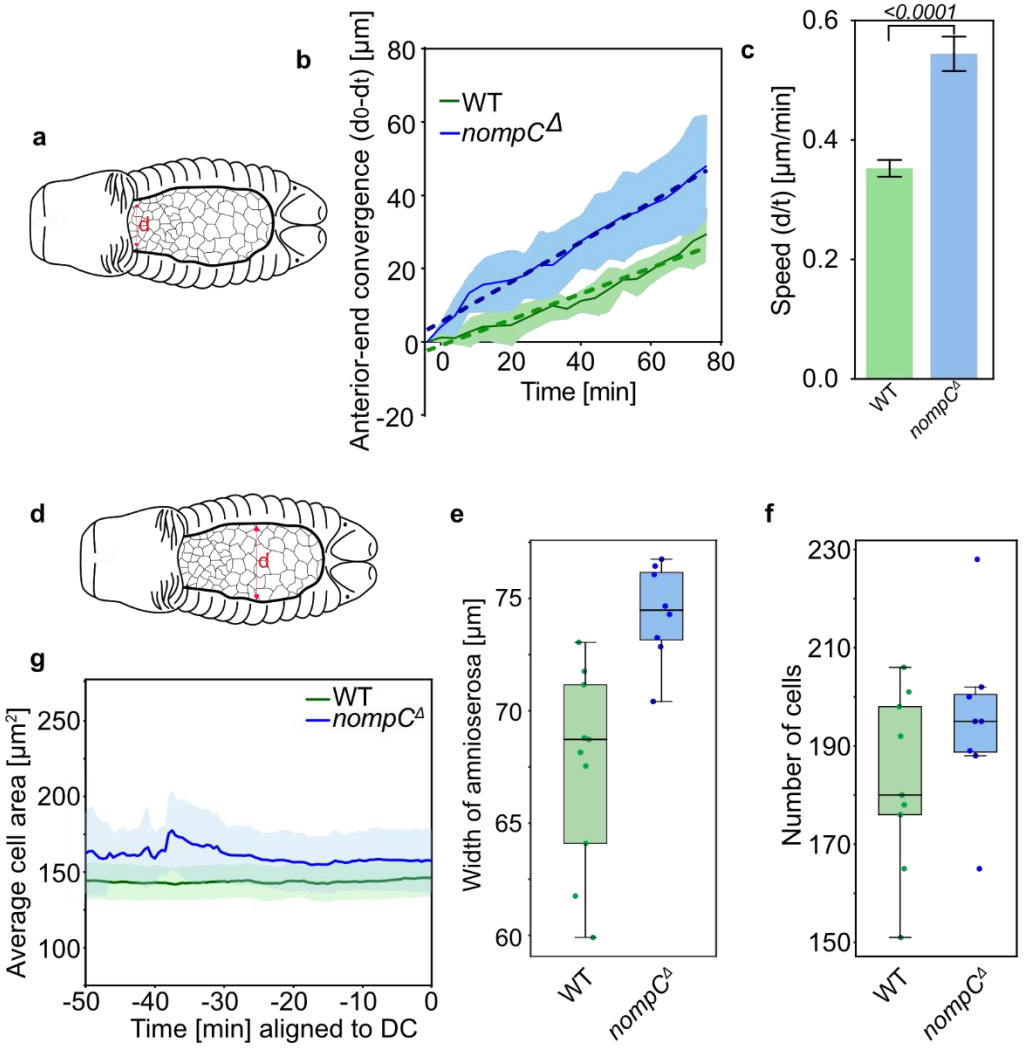

Figure 3.13. *nompC$^{\Delta}$* embryos enter into the dorsal closure stage faster than the WT. a. Scheme of elliptical phase embryos of *Drosophila*. d is the distance between two actin cables. b. displacement-time plot showing the convergence of actin cables with time. The distance was measured every 4 minutes. The solid line indicates the mean, the shaded area represents 95% confidence interval, and the dotted line is the linear fitting curve. (WT, N=10, $R^2 = 0.8920$; *nompC$^{\Delta}$*, N=8, $R^2 = 0.7884$). c. The convergence rate (speed) was significantly greater in the *nompC$^{\Delta}$* embryos. Statistical significance was calculated by Student's t-test. (Data presented as Mean±SD) d-e. Width, d is the maximum lateral span of the AS tissue. The loss of NompC prevents the tissue to become smaller even if the DC onsets. (Data presented as

Mean±variance) f. Boxplot indicates the total number of AS cells in each embryo (Mean±variance). Each dot represents one embryo. g. Average AS cell area was plotted over the time axis. Time 0 indicates onset of DC.

Based on the evidence that NompC is present in AS epithelium and depletion of it leads to various behavioural and morphogenetic defects, including DC, I wondered if NompC acts as a mechanosensitive ion channel in AS cells.

3.3. Calcium (Ca^{2+}) influx

Absence of NompC leads to decreased Ca^{2+} influx upon wounding

To measure the Ca^{2+}-influx, I utilised Tubulin-Gal4 driven expression of Myr-GCaMP7s, a fluorescence reporter of junctional Ca^{2+}. I considered the mean intensity across the ROI as the reporter molecules are not limited to the adherens junctions but to the cell membrane as a whole. In unperturbed conditions, *nompC$^{\Delta}$* embryos showed a significant reduction in GCamP7s signal intensity compared to their WT counterpart, see Figure 3.14.

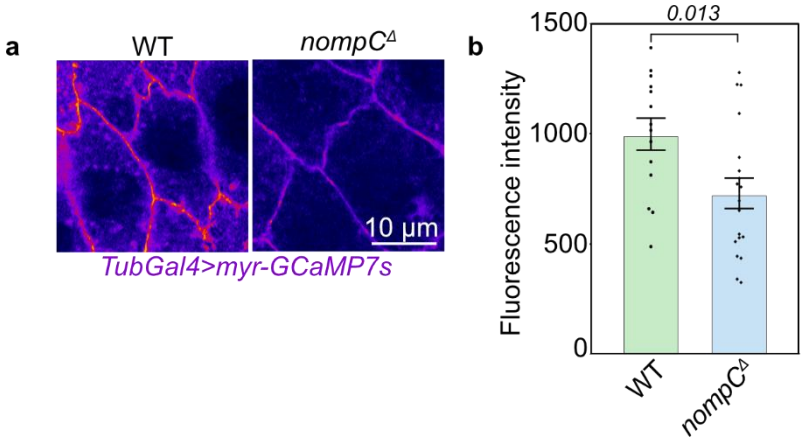

Figure 3.14. *nompC$^{\Delta}$* showed a reduction in Ca^{2+}-influx in the unwounded epithelium. a. The expression of Myr-GCaMp7s was introduced by recombining *Tub-Gal4* with *UAS-myr-GCaMP7s* in the third chromosome of the flies. The AS cells of the stage 13 embryos were imaged under 63x oil objective by LSM980. b. A significant decrease in the overall intensity of the calcium signal in *nompC$^{\Delta}$* mutants was observed compared to the WT embryos. (The data is shown in mean ± SD; WT, N=14; *nompC$^{\Delta}$*, N=16; Statistical significance was calculated by Student's t-test; p=0.013)

Laser-induced wounding allows us to perturb a tissue in single-cell resolution mechanically. Wounding single AS cells with 8% 355 nm laser leads to a significant increase in Ca^{2+}-influx in the wounded cell and the junctions of the immediate neighbouring cells, see Figure 3.15.a. I applied the wounding-based Ca^{2+}-response assay in the *nompC*$^{\Delta}$ embryos and found that the relative intensity of Myr-GCaMP7s at the neighbouring cell junction around the wounding site increased far less (~4 fold) than what was evoked by the WT control, see Figure 3.15.b.

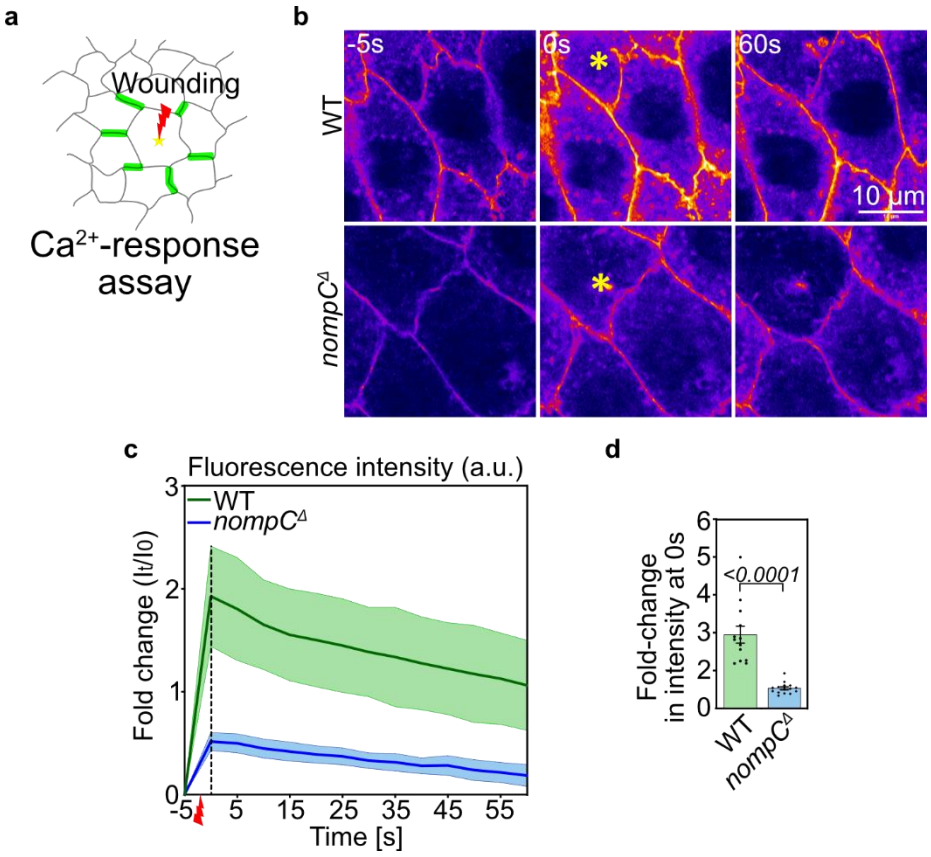

Figure 3.15. Wound-induced neighbour cell Ca^{2+} dynamics are perturbed in *nompC*$^{\Delta}$ mutants. a. Single AS cells in the middle of the tissue were targeted, and the subsequent increase in the neighbouring cell junctions was measured over time. If the cells are affected by a mechanical perturbation in their neighbourhood, they are expected to allow Ca^{2+}-influx, one of the mediators of which is, of course, the mechanosensitive channels. b. Snapshots showing the Ca^{2+} dynamics before and after the wounding (-5s, 5 seconds before wounding; 0s, time-point immediately after wounding; 60s, 1 minute after wounding). The recording was done at 5s intervals by 63X oil objective of LSM980. The target cell is

marked with a yellow star. c. The normalised mean fluorescent intensity in fold change was plotted over time (indicated by the solid line). (WT, N=13; *nompC*$^{\Delta}$, N=14). The shaded area represents the 95% confidence interval. The red thunder sign at the time-axis indicates the time of wounding. d. Statistical significance of mean fold-change immediately after wounding was calculated by Student's t-test. (Data presented as Mean±SD)

Imaging Ca^{2+} as a novel indicator of epithelial cell dynamics

I generated a fly line having Tubulin-Gal4 driven expression of the membrane-bound version of GFP-based calcium sensor GCaMP7s. I recombined Tub-Gal4 alongside Myr-GCaMP7s on the third chromosome to drive a constitutive expression of the calcium sensor.

I recorded time-lapse images of WT AS cells expressing Myr-GCaMP7s with a frame rate of 30 s. I analysed the area change over time. As the cells are pulsating, I obtained a sinusoidal area-time curve. I measured the mean GFP signal intensity of these cells over time. I normalised the intensity with the area of the cell concerned to get the calcium density per unit cell area at each time point. I observed a similar sinusoidal pattern of Ca^{2+} density over time. However, there was a decline of the absolute signal intensity over time due to bleaching.

I observed two cell pairs, one sync. and the other anti-sync. The Ca^{2+} signal intensity was negatively correlated with the cortical area of the AS cells. The increase in Ca^{2+} density was followed by a decrease in the cell area and vice versa, see Figure 3.16. However, I have not investigated Ca^{2+} oscillation in the embryos with *nompC*$^{\Delta}$ background.

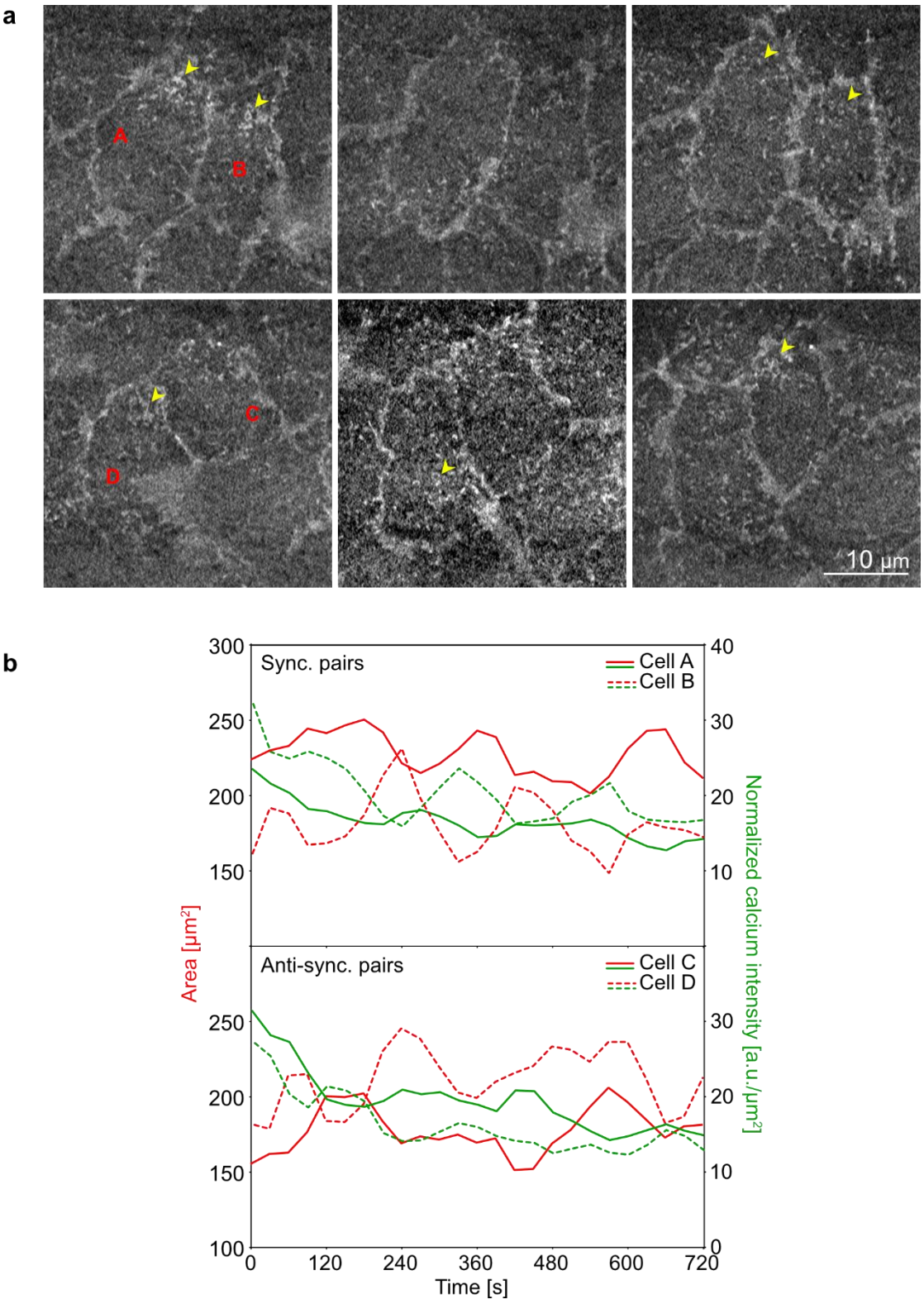

Figure 3.16. Ca^{2+} density is a readout of dynamic cell behaviour. a. Top panel shows cells A and B having synchronized oscillation. Bottom panel shows cells C and D having anti-synchronized oscillation. b. The plots exhibit the area and the respective Ca^{2+} density oscillations over time.

3.4. Wounding

Loss of NompC led to the loss of cell-to-cell relay of mechanical stimuli

To test whether NompC plays any role in sensing a mechanical stimulus by AS cells, I ablated the junction between two AS cells. This laser-induced ablation acted as a mechanical stimulus. The immediate effect of this should be reflected by the immediate neighbouring cells. To measure this effect, I analysed the oscillation behaviour of the neighbouring cells in terms of area variance for the first 3 minutes, as wound healing response was triggered after that. To understand the expanse of the impact, I also analysed the same for the next-next neighbours and cells further away from the site of the junction cut (as control). The experiment is schematically shown in Figure 3.17.a.

Neighbouring AS cells of WT embryos responded to the mechanical injury by significantly lowering their oscillation. However, the next-to-next neighbours behaved like the control cells by not responding to the signal. In *nompC*$^{\Delta}$ mutant embryos, the next neighbours continued to oscillate without much changes in amplitude. The next-to-next neighbours behaved similarly to the control cells by continuing oscillation. Figure 3.17.c,d summarise the results.

However, the overall oscillation amplitude of the AS cells in *nompC*$^{\Delta}$ mutants was significantly reduced than in the WT. This led me to ask if the oscillation pattern is different in *nompC*$^{\Delta}$ mutants than in the WT.

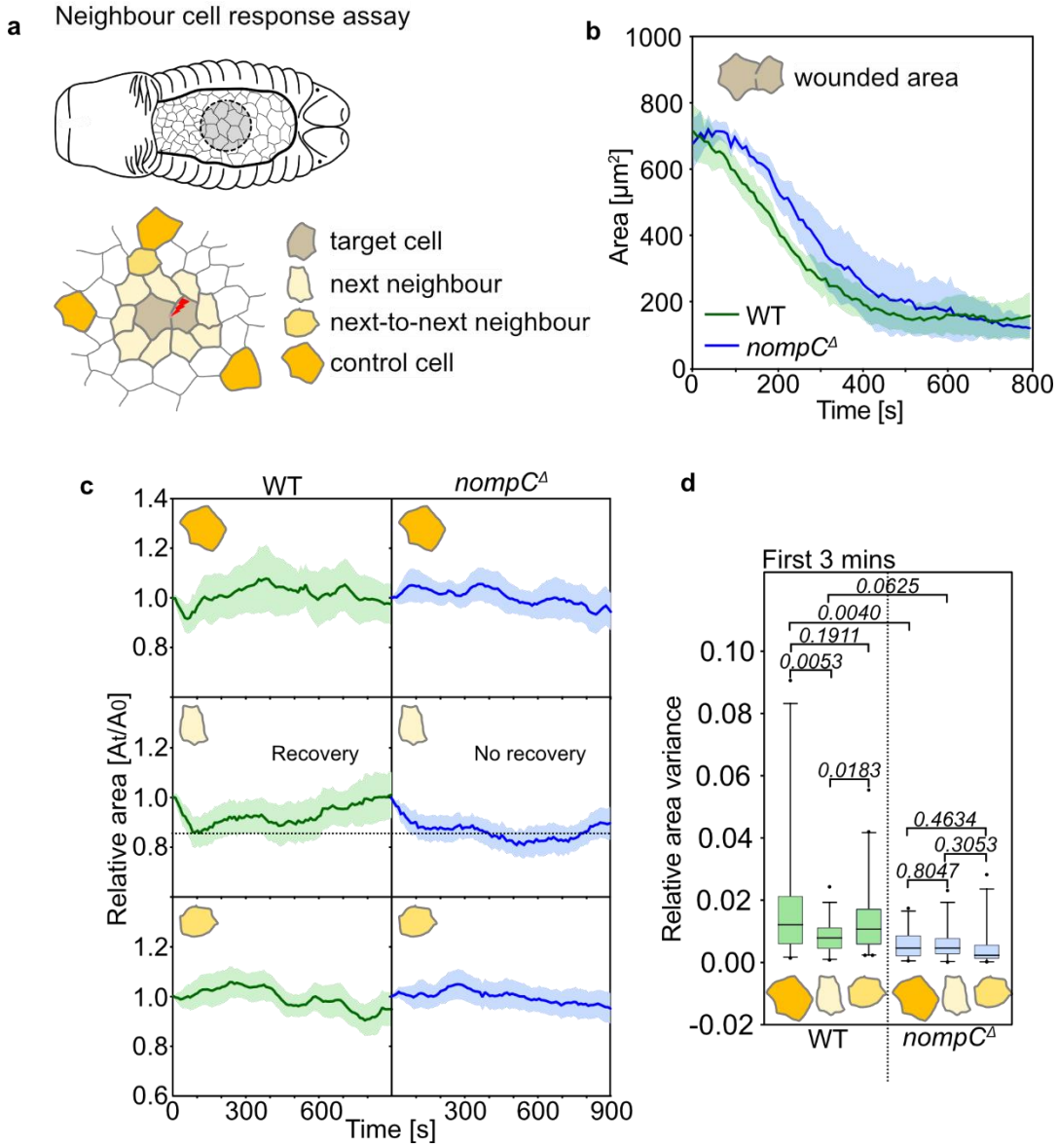

Figure 3.17. Analysis of area variance of neighbouring cells after the laser-induced ablation of a single junction. a. A region of interest in the middle of the AS tissue was selected. The junction between the two cells was ablated by the 355 nm pulsed laser. The area variance of the next-neighbours, next-to-next neighbours and control cells was calculated after the ablation. The cells were differentially colour-coded. b. Wound healing begins immediately after the wounding. The neighbouring cells actively involve in closing the wounded area. Wound healing happens even in the absence of NompC but at a slower pace. d. First, second and third panels showed the oscillation patterns of control cells, next-neighbours and next-to-next neighbours, respectively. The area (μm^2) was calculated for individual cells and normalised over their initial area. The area was measured for 15 mins after the laser cut. The area of the neighbouring cells dropped immediately after the cut in the WT and underwent a fast recovery. However, in the *nompC*$^{\Delta}$ embryos, the response in less pronounced and the cells persisted with their contracted area

over time. (The solid line represents the mean, and the shaded area represents the 95% confidence interval) d. The comparison of area variance (μm^4) indicated that the oscillation of the next-neighbours reduced significantly in WT embryos, but in the absence of NompC, the effect is less obvious. Interestingly, area variance was significantly reduced even in the control cells of *nompC$^{\Delta}$* embryos than their WT counterparts. (WT, Control cells, N=30; Next-neighbours, N=31; Next-to-next-neighbours, N=46; *nompC$^{\Delta}$*, Control cells, N=24; Next-neighbours, N=34; Next-to-next neighbours, N=32; Statistical significance was calculated by Student's t-test) (Data presented as Mean±5-95% CI)

I closely observed the wound-healing phenomenon. In the WT embryos, the neighbouring cells stopped oscillation and elongated toward the wounded site to repair it. In the absence of NompC, this effect was more pronounced. The cells merely depended on increasing their anisotropy and acted like a fluid to close the wound. This is sometimes accompanied by exchanging neighbouring cell junctions at the wound edge. This behaviour, absent in WT, strongly suggests the increased fluidity of the AS tissue, see Figure 3.18.

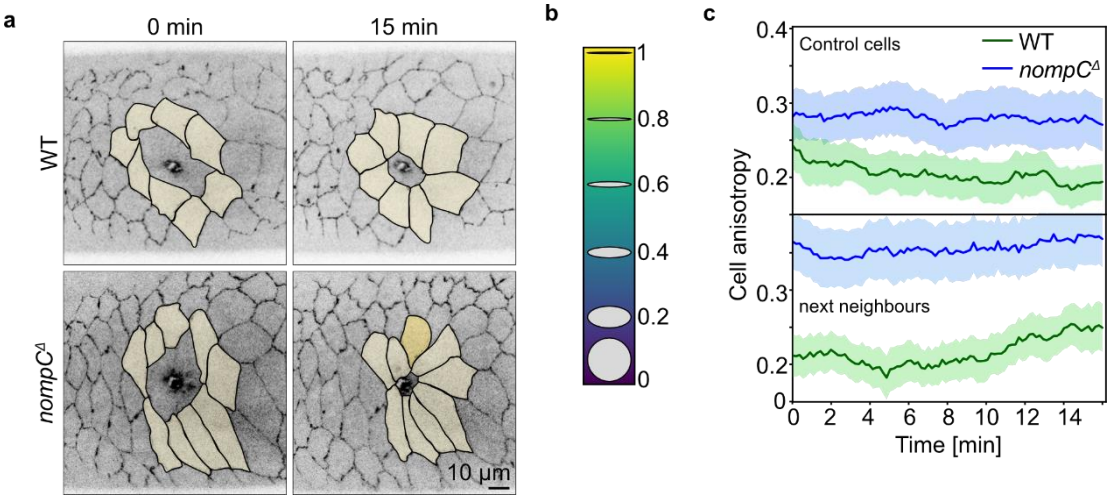

Figure 3.18. Neighbouring cell behaviour to facilitate wound healing. a. Wound closure mechanism in the WT and *nompC$^{\Delta}$* embryos. The neighbouring cells in the WT, instead of changing their shape much, concertedly contract toward the wounded site to facilitate closure. AS cells in the *nompC$^{\Delta}$* mutants, on the contrary, passively elongate toward the wounded region, exhibiting increased fluidity of the tissue. The given example shows one neighbouring cell lost contact with the wound edge. b. On the scale of anisotropy, 0 stands for a perfect circle, and 1 means a straight line. c. Dynamics of neighbouring cell anisotropy after wounding. Neighbouring cells of *nompC$^{\Delta}$* embryos were more anisotropic all along. Strikingly, the control cells of the *nompC$^{\Delta}$* mutants are more anisotropic than the WT.

3.5. Morphometry and morphodynamics

Anisotropic AS cell morphology in *nompC$^{\Delta}$* embryos

When the AS tissue got exposed after the germband retracted in WT embryos, the cells appeared to be highly elongated in the lateral direction (towards the lateral epidermis). However, with time the cells became more isotropic (having dimensional symmetry).

In *nompC$^{\Delta}$* embryos, the AS cells were stretched towards the lateral epidermis like the WT embryos after the germband retraction. But, unlike the WT embryos, the cells remained anisotropic even in the elliptical phase, see Figure 3.19. The beginning of dorsal closure was defined as time 0.

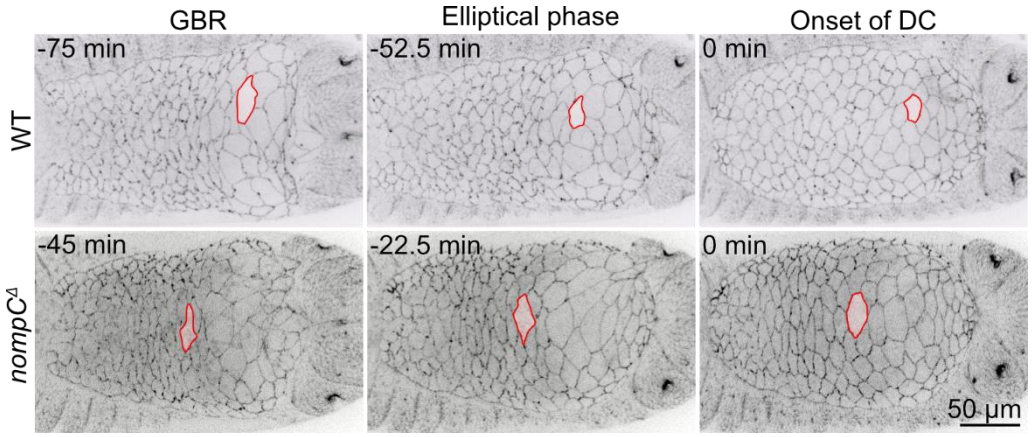

Figure 3.19. Gradual cell shape changes were affected in *nompC$^{\Delta}$* embryos. Snapshots of the time-lapse movies recorded with 25X oil objective of the spinning disc microscope. In WT embryos, the AS cells gradually transition from anisotropic to isotropic morphology. AS cells of *nompC$^{\Delta}$* embryos remained anisotropic even at the onset of the dorsal closure phase. The junctions were marked by Ecad-GFP. The embryos were aligned to the onset of DC (time=0).

To measure the asymmetrical cell shape, the anisotropy index was calculated by circular eccentricity (e; e=0, perfectly circular; e=1, perfectly linear). I analysed the anisotropy index of the AS cells averaged over all the embryos. The comparison between the average anisotropies of WT and *nompC$^{\Delta}$* embryos during the elliptical phase is shown in Figure 3.20.b. I also found that the AS cells in the middle of the tissue

were comparatively more anisotropic than those at the periphery. To distinguish the middle cells from the peripheral cells, a region of interest (ROI) was selected based on the size and shape of the tissue, see Figure 3.20.c.

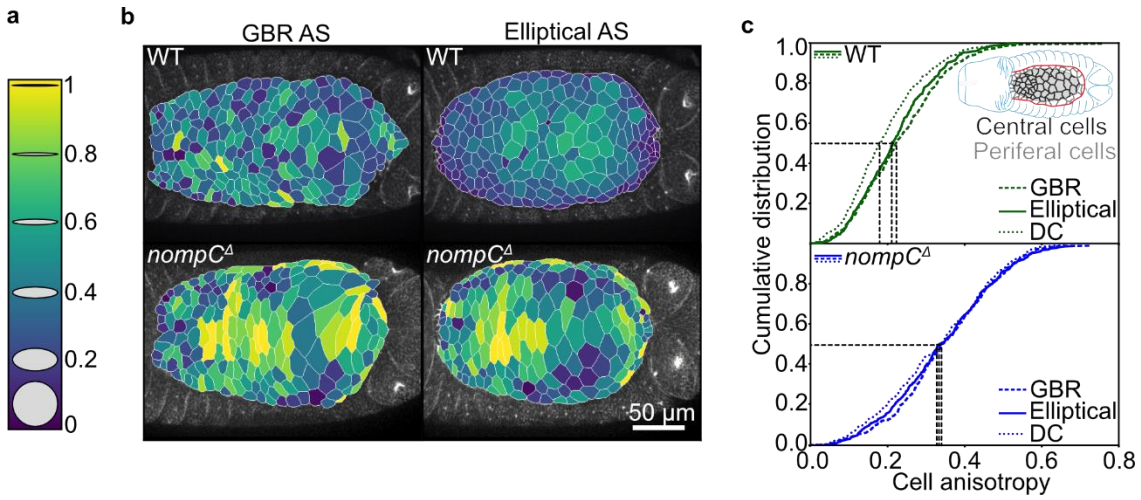

Figure 3.20. Quantification of spatiotemporal transition of AS cell anisotropy. a. On the scale of anisotropy, 0 stands for a perfect circle, and 1 means a straight line. b. heat-map representation of AS cell shapes. False colour was annotated as per the anisotropy scale. c. Cumulative distribution of anisotropy index of all the middle AS cells during different phases of the embryos. The curves for *nompC*$^{\Delta}$ embryos were overall right-shifted, showing a consistently high degree of anisotropy throughout the morphogenetic phases. (WT, N=10; *nompC*$^{\Delta}$, N=8; N= number of embryos. The solid line indicates the mean, and the shaded area refers to the 95% confidence interval)

Another important parameter representing the direction of anisotropy is the 'cell angle'. The cell angle for the cells oriented axially was 0˚ and 90˚ for those with lateral orientation. The cell angle was calculated and compared similarly to cell anisotropy. Figure 3.21. indicates that the anisotropic cell shape was biased to the lateral direction.

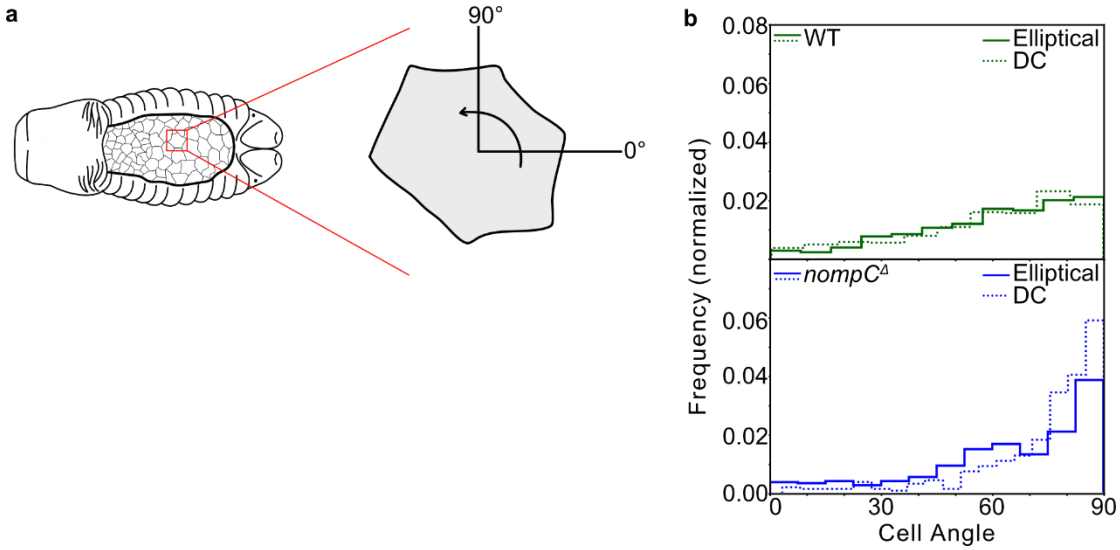

Figure 3.21. Quantification of the orientation of AS cell anisotropy. a. Schematic representation of the orientation of AS cell axis with respect to the anterior-posterior axis of the embryo. b. The angle of orientation of the cell axis was calculated for the AS cell over multiple embryos. The frequency of cell angles was normalised with the total number of cells analysed.

The absence of NompC inhibits AS cell oscillation

Any oscillation has attributes like periodicity (time^{-1}), wavelength and amplitude. Although the periodicity was almost unchanged, the absence of NompC protein hugely affected the oscillation amplitude. I recorded time-lapse images of live AS coexpressing Ecad-GFP and Sqh-mCh (Sqh, myosin regulatory light chain) to measure the cell area and cortical myosin intensity over time. The cells underwent contraction immediately after the myosin foci formed. The time point with the maximum myosin intensity was set as time 0. The area and myosin intensity were normalised by their respective values at time 0. Figure 3.22.b. summerises the observation and analysis. The cortical area oscillation is dampened in *nompC*$^{\Delta}$ embryos. The corresponding myosin oscillation was also reduced compared to the WT cells.

To check if this observation with a few selected cells is valid for all the AS cells, I performed an ensemble analysis based on the dynome data. I calculated the coefficient of variation of all the AS cell areas over 10 WT and 8 *nompC*$^{\Delta}$ embryos. The coefficient was significantly reduced in *nompC*$^{\Delta}$ embryos, suggesting a relatively less dynamic AS tissue, see Figure 3.22.c.

Another important parameter for a sinusoidal curve is the time period. In the context of cell oscillation, this time period is the measure of how long a cell takes to finish a complete cycle of contraction-relaxation (from one contraction to the next contraction with relaxation in between). The time period when compared between the dynome data of the WT and *nompC*$^{\Delta}$ embryos, I found that the depletion of NompC led to a faster oscillation kinetics indicated by a significant reduction of the time period, see Figure 3.22.d. The time-period for the WT embryos was 5.47 ± 0.19 min, whereas that of the *nompC*$^{\Delta}$ embryos was 4.99 ± 0.19 min.

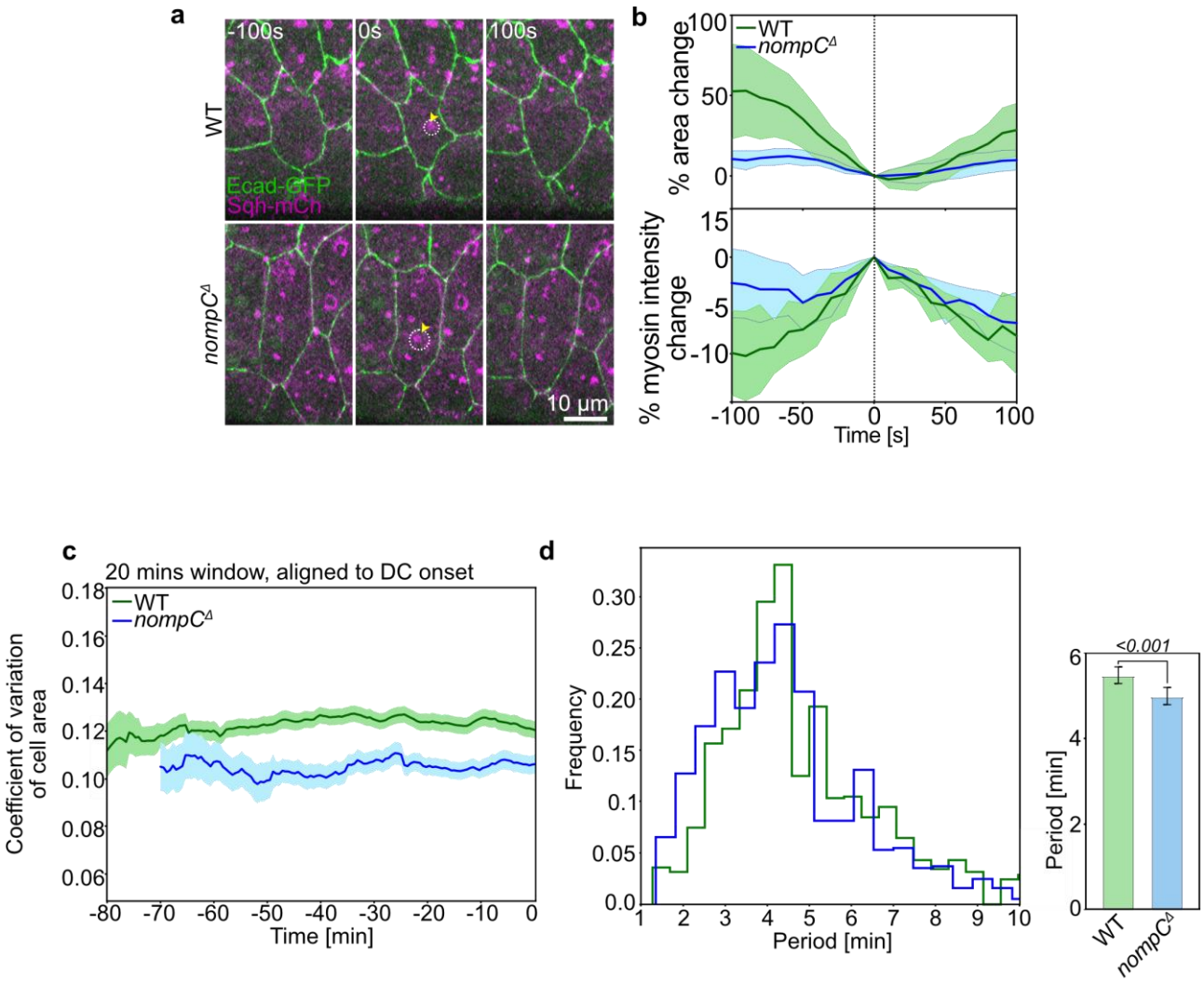

Figure 3.22. The oscillation amplitude of single AS cells. a. The movies of AS cell oscillation were taken with a time interval of 10s. Ecad-GFP marked the cell junctions, and Sqh labelled with m-cherry was used to observe the myosin dynamics. Myosin has two different populations. Some signals appeared stationary, whereas others were highly dynamic. This dynamic myosin formed foci (aggregates) at the

cortical domain of the cell. Building up of these cortical myosin foci led to cell contraction. b. The area and the corresponding myosin accumulation were measured over 200s. The solid line indicates the mean, and the shaded area indicates the 95% confidence interval. The area change and myosin intensity change were lower in the *nompC$^{\Delta}$* embryos. The oscillation amplitude was significantly reduced. (WT, N=8; *nompC$^{\Delta}$*, N=8). c. The coefficient of variation of AS cells was calculated as a ratio of the standard deviation to the mean. A higher coefficient of variation implies a higher fluctuation during oscillation. The oscillation amplitude of AS cells in *nompC$^{\Delta}$* embryos was consistently and significantly smaller than the WT ones. The point of onset of DC was considered to be time 0. The solid line indicates the mean, and the shaded area refers to the 95% confidence interval). d. The distribution of the time period of AS cells undergoing oscillations. The bar diagram shows the statistical significance of the time period between the two groups. (WT, N=1684; *nompC$^{\Delta}$*, N=1202; N= number of cells considered for calculation). (Statistical significance was calculated by Student's t-test).

3.6. Cytoskeleton

Actin cytoskeleton is altered in *nompC$^{\Delta}$* embryos

Actin is a major cytoskeleton component that provides a cell with both stability and dynamics. To investigate if NompC regulates actin organisation in epithelial cells, I stained stage 13 embryos with Phalloidin. I measured the actin density (intensity/cell area) of individual z-sections to cover a depth of ~3 μm from the cortex to the interior of the cells. The first 7 stacks were cumulatively taken as the representative of the cell cortex. The deeper actin network stands for the basolateral actin population. The overall density distribution changed in the *nompC$^{\Delta}$* embryos. While in the WT embryos, the density distribution is more or less homogeneous, the absence of NompC caused a loss in both cortical and basolateral actin populations, leading to a skewed distribution, see Figure 3.23.a-c.

I also analysed the orientation of actin in the cell cortex using the OrientationJ plugin of FIJI (Rezakhaniha *et al.*, 2012). The orientation did not differ much between the WT and *nompC$^{\Delta}$* embryos. Most of the cortical actin was oriented toward the lateral epidermis, see Figure 3.23.d-f.

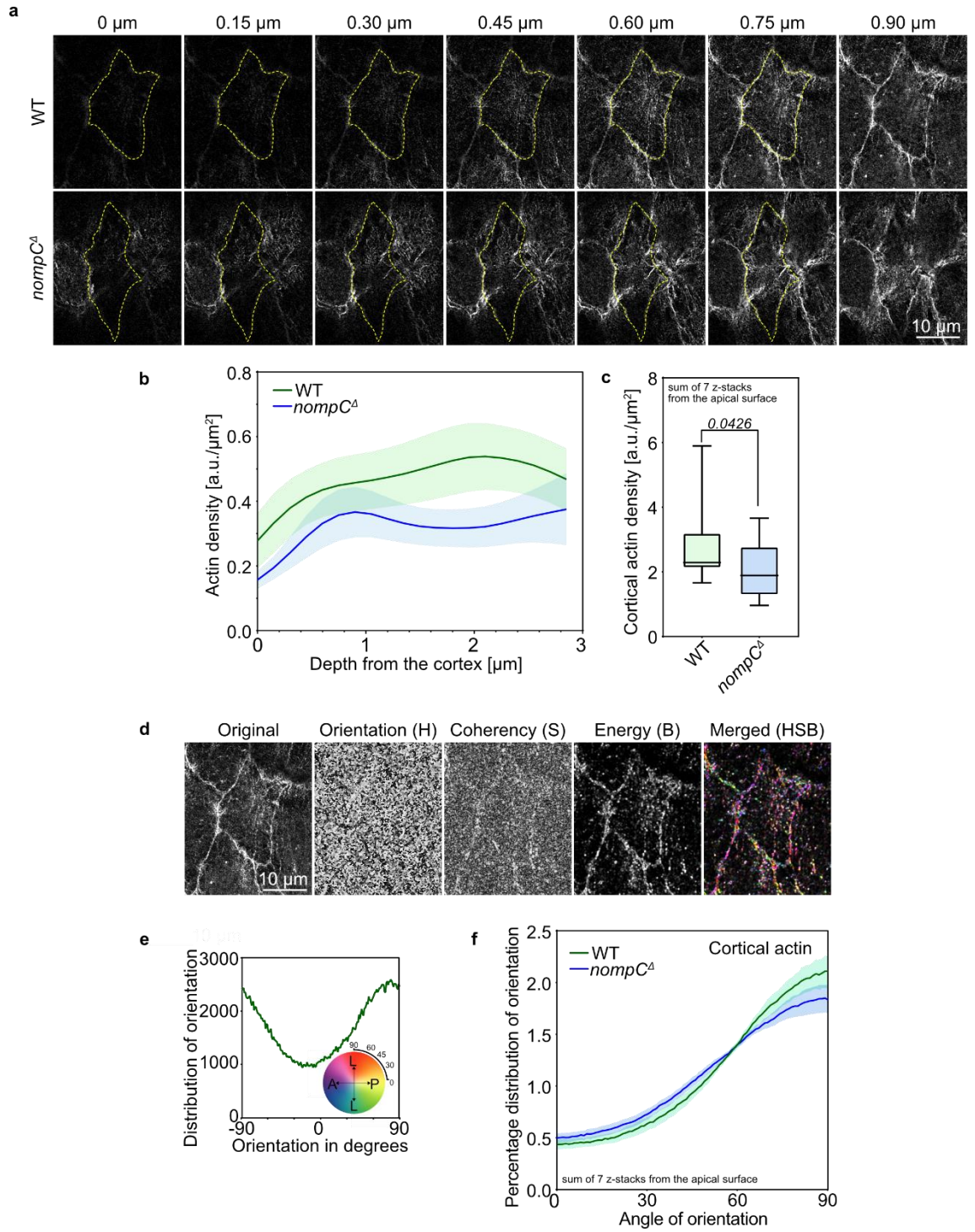

Figure 3.23. Actin distribution but not the orientation is regulated by NompC. a. Z-stacks from the most apical surface to ~1 µm deep inside the AS cells. b. The distribution of actin density along the z-axis of the cells. c. Cortical actin density was significantly higher in the WT than in *nompC*$^{\Delta}$ embryos. (WT, N=15; *nompC*$^{\Delta}$, N=17; N=number of cells analysed) (Data presented as Mean±5-95CI) d.

OrientationJ projects the data in HSB colour-coded format. Hue (H)= orientation in degrees, Saturation (S)= coherency, Brightness (B)= energy. e. Example distribution of orientation plot obtained running OrientationJ analysis. f. No difference in actin orientation between the WT and *nompC$^{\Delta}$* embryos.

I recognised that there are conspicuously thick and long bundles of actin filaments distributed across the z-axis of the cells. The number of such fibers was significantly more in the cortical section of *nompC$^{\Delta}$* AS cells than in the WT ones, see Figure 3.24.b. In WT cells, these fibers were scarce. However, if present, their lengths do not vary much, see Figure 3.24.c. In the AS cells of *nompC$^{\Delta}$* embryos, the orientation of these fibers was more axial (toward anteroposterior). In contrast, in the WT cells, they are mostly lateral (toward the lateral epidermis), see Figure 3.24.e,f. The comparison failed to show significance as the number of such fibers was too low in the WT embryos. To validate my observation with stained samples, I looked into the live embryos expressing Moesin-RFP. I observed a big population of very stable cortical actin fibers in the *nompC$^{\Delta}$* AS cells. In the WT embryos, they were much fewer in abundance, see Figure 3.24.g.

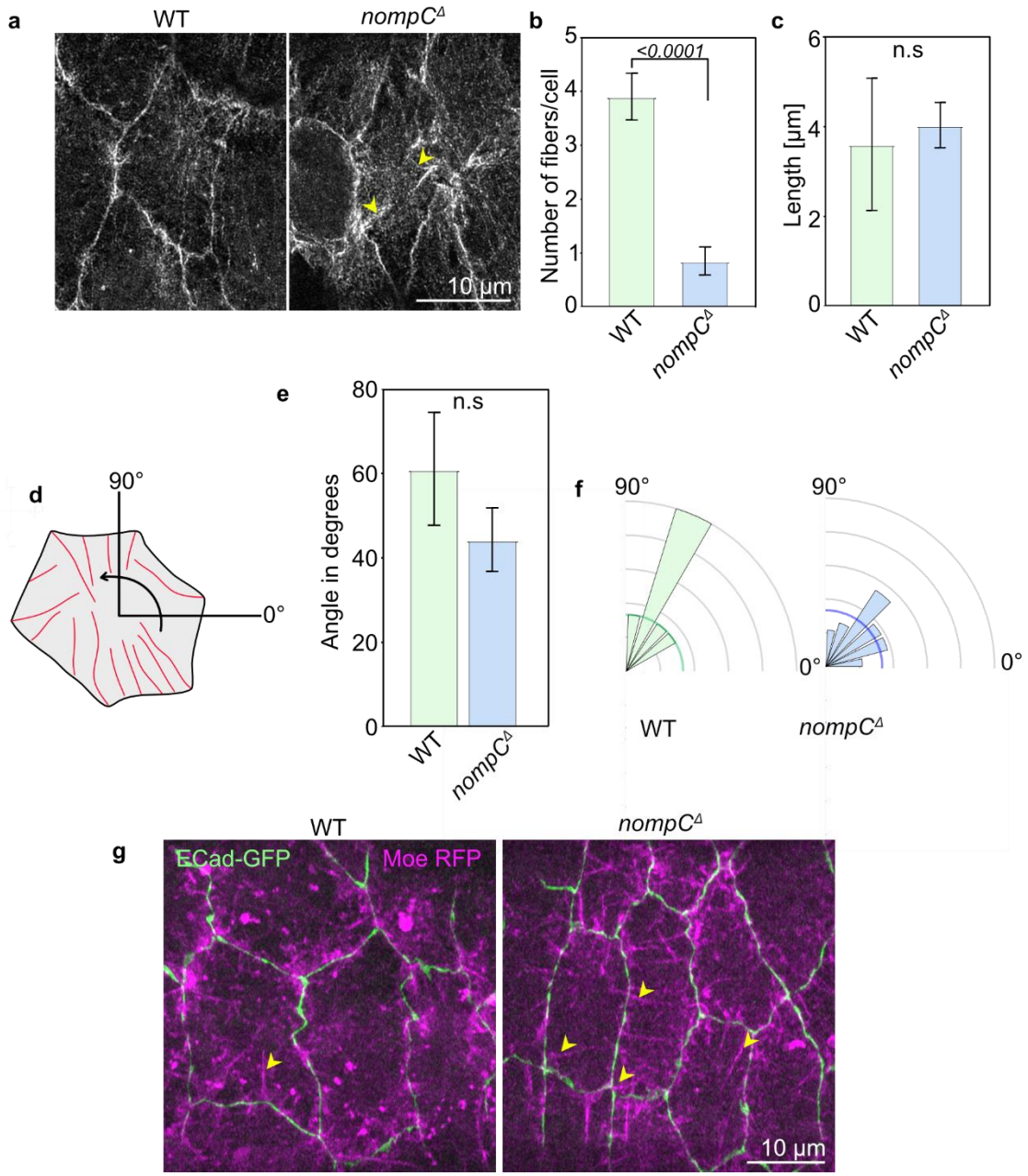

Figure 3.24. Actin fibers were prominent in *nompC$^{\Delta}$* embryos. a. First 7 z-stacks were merged to have the images. Yellow arrowheads point b. The number of actin fibers was significantly higher in the absence of NompC. (Data presented as Mean±SD) c. The length of such fibers was consistent in both the WT and *nompC$^{\Delta}$* embryos. (Data presented as Mean±5-95%CI)) d. Schematic representation of angle of orientation for actin fibers. The fibers were manually selected, and the length and Feret angle were calculated using FIJI. e-f. WT embryos had fewer actin fibers, but if present, they were mostly laterally

oriented. (Data presented as Mean±5-95% CI) g. Snapshots from live images (with max-projected z-stacks) showing stable, cortical actin fibers. Yellow arrowheads point to the actin fibers.

Tubulin orientation corresponded to elongated cell morphology

Microtubule dynamics within the plane of the tissue is one of the fundamental morphogenetic processes required for epithelial cell reshaping. During *Drosophila* pupal wing development, collective cell elongation in a particular axis is facilitated by the proximal-to-distal alignment and formation of a transcellular network of microtubules. Interestingly, myosin contractility in these cells is low. Hence, microtubules in these cells are stiff and meant to bear compressive forces.

To probe into the distribution of microtubules in AS cells, I collected embryos of elliptical and dorsal closure phases and stained them for α-tubulin. I imaged the AS tissue with 63X oil immersion objective of LSM980 using airy-scan. The images were then post-processed by deconvolution. By this method, I could detect microtubules in single fibre resolution. Using the FIJI plugin, Orientation J, I determined the frequency of tubulin fibers belonging to a range of angles, from 0˚, being axially oriented, to 90˚, being laterally oriented, see Figure 3.25.a,b.

The WT AS cells showed a transition in the orientation of the tubulin fibers from the elliptical to the DC phase. In the elliptical phase, the fibers were oriented laterally in the same direction of cell anisotropy. However, the fibers became randomly distributed as the cells became more isotropic in the late DC phase. In the *nompC*$^{\Delta}$ embryos, on the contrary, the fibers continued to remain anisotropically distributed in the same direction of cell elongation, see Figure 3.25.c,d.

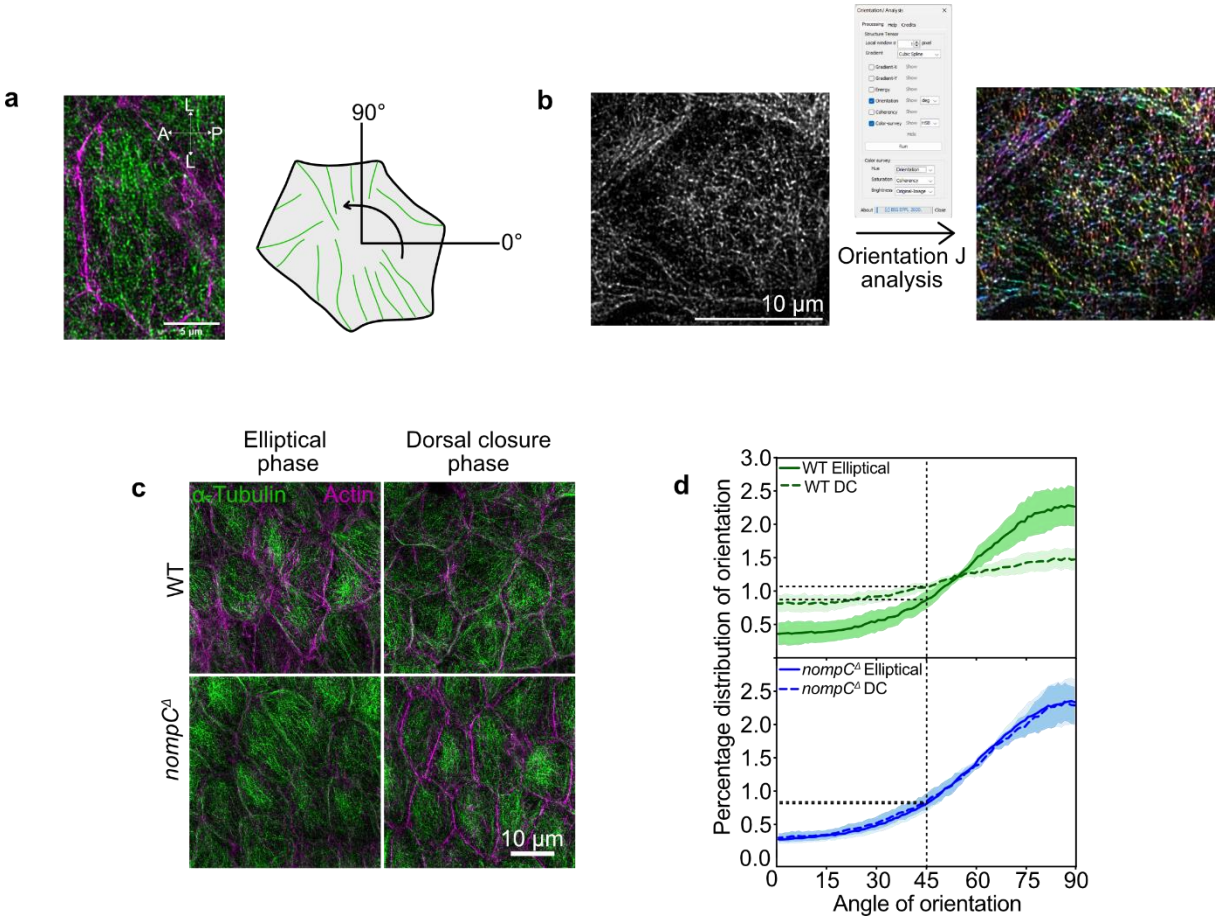

Figure 3.25. Quantification of the orientation of tubulin fibers in AS cells. a. The example of a single AS cell stained with α-tubulin antibody and phalloidin (F-actin). b. The angle of orientation of tubulin filaments was automatically measured by OrientationJ. c. In the WT embryos, tubulin fibers became more isotropic in the DC phase. In the *nompC*$^{\Delta}$ embryos, AS remained anisotropic and oriented laterally parallel to the axis of elongation of the cells. c. The frequency of fibers corresponding to 0˚ to 90˚ angles was calculated and normalised by the total fibers analysed. The distribution was flattened in WT DC cells, whereas in *nompC*$^{\Delta}$ cells, the distributions of elliptical and DC phases overlapped, showing consistent anisotropy. (WT, elliptical phase, N=10; DC phase, N=15; *nompC*$^{\Delta}$, elliptical phase, N=13; DC phase, N=10; N=number of cells analysed. The shaded area signifies the 95% confidence interval).

3.7. Force balance

AS cell junctions exhibited anisotropic force distribution

Based on the anisotropic AS cell shapes in *nompC*$^{\Delta}$ embryos, I enquired if the absence of NompC also affects the mechanical properties (force distribution) across the tissue. A usual approach for estimating the mechanical tension experienced by the membrane or junction of a cell is by laser-induced ablation of the junction and measuring the recoil of the adjacent 3X vertices with time. The recoil velocity immediately after the ablation is directly proportional to the tension experienced by the concerned junction.

I used a 355 nm pulsed laser to cut the junctions for all my experiments. I cut single AS junctions in each embryo (at the elliptical phase) and recorded them at a rate of twice per second. The junctions oriented towards the anterior-posterior axis of the embryo were called axial junctions, and those oriented towards the lateral epidermis of both sides of the embryo were called lateral junctions. The displacement of the 3X vertices was measured using FIJI. Initial recoil velocity was calculated by fitting and determining the slope of the displacement-time curve for the first 5 s after ablation.

WT embryos have a higher lateral junction tension

I performed laser-induced cuts at the junctions oriented axially and laterally of the WT embryo. Lateral cell junction tension in WT embryos was significantly higher than the axial junction tension. However, the viscoelasticity (parameter referring to the rate of decay) for these two junctions was detected to be comparable, see Figure 3.26.

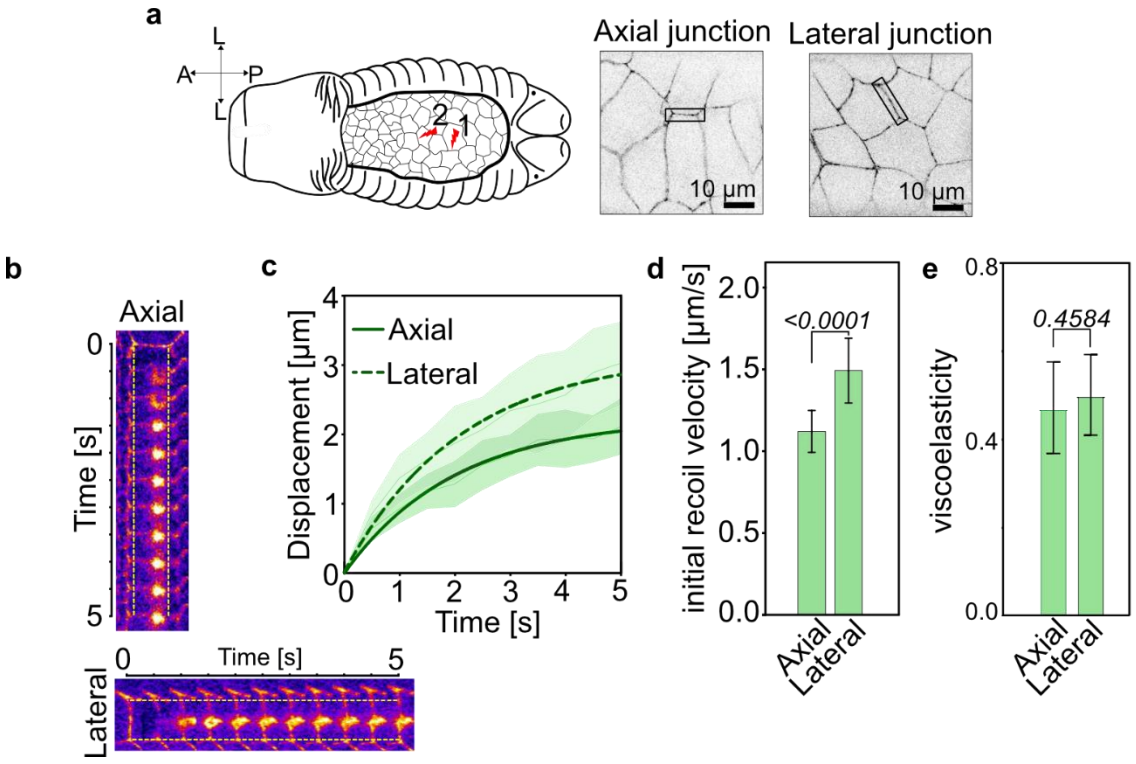

Figure 3.26. The recoil velocity of the lateral AS cell junctions in the WT embryos was higher than that of the axial junctions. a. Scheme of a dorsally posed embryo and an exemplary live image showing the junctions directed towards the anterior-posterior axis of the embryo were defined as axial junctions (1). The junctions oriented toward the lateral epidermis are the lateral junctions (2). b. The kymograph for the ablation of junctions with axial and lateral orientation. c. The trajectory of the displacement of 3X vertices followed in multiple embryos. The thin solid line indicates the mean, and the shaded area indicates the 95% confidence interval. The fitting is shown with the thick solid curve. (WT, Axial junction N=13, Lateral junction, N=13). d. The bar chart shows the mean with SD of the calculated initial recoil velocity across multiple embryos. (Statistical significance was calculated by Student's t-test). e. The bar chart shows the mean with SD of the calculated viscoelasticity across multiple embryos. (Statistical significance was calculated by Student's t-test) (Mean±SD).

nompC$^{\Delta}$ embryos have an increased axial junction tension

I performed laser-induced cuts at the junctions oriented axially and laterally of the *nompC*$^{\Delta}$ embryo. Axial cell junction tension in *nompC*$^{\Delta}$ embryos was significantly higher than the lateral junction tension (~2.5 times). Moreover, the viscoelasticity of the axial junction was also significantly higher than the lateral junction tension, suggesting heterogeneity in the material property across the tissue, see Figure 3.27.

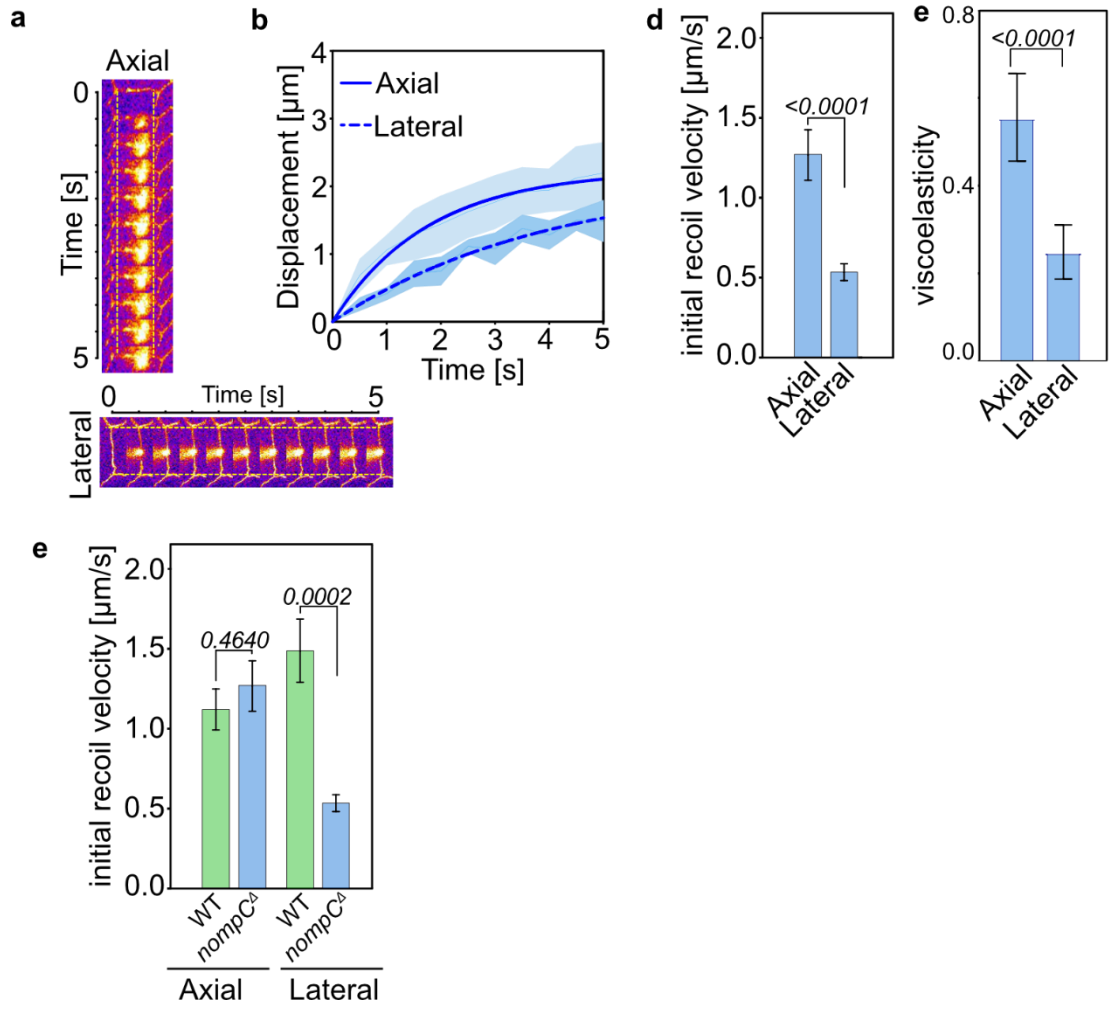

Figure 3.27. The recoil velocity of the axial AS cell junctions in the *nompC*$^{\Delta}$ embryos was higher than that of the lateral junctions. a. The kymograph for the ablation of junctions with axial and lateral orientation. b. The trajectory of the displacement of 3X vertices followed in multiple embryos. The thin solid line indicates the mean, and the shaded area indicates the 95% confidence interval. The fitting is shown with the thick solid curve. (WT, Axial junction N=11, Lateral junction, N=12). d. The bar chart shows the mean with SD of the calculated initial recoil velocity across multiple embryos. (Statistical

significance was calculated by Student's t-test). e. The bar chart shows the mean with SD of the calculated viscoelasticity across multiple embryos. (Statistical significance was calculated by Student's t-test) (Mean±SD). f. Comparison of initial recoil velocities between the WT and *nompC*$^{\Delta}$ embryos for the junctions with similar orientations. (Mean±SD) (Statistical significance was calculated by Student's t-test).

The junction cuts suggested that the lateral junction tension is higher than the axial junction tension in WT embryos. In the absence of NompC, the situation was reversed. The lateral junction tension significantly decreased. I hypothesised that instead of generating a resistive force against the pulling force from the lateral epidermis, the AS cells orient themselves towards the direction of the pulling force, causing the anisotropic morphology of the cells. To know the pulling force from the lateral epidermis, I cut the lateral junctions of the first row of lateral epidermal cells.

Tension at the lateral junction of the lateral epidermal cells

I cut the lateral junctions of the lateral epidermis to know if the absence of NompC also affects the pulling tension from the lateral epidermis. The tension, inferred from the initial recoil velocity, was, in fact, comparable between the WT and the *nompC*$^{\Delta}$ embryos, see Figure 3.28.

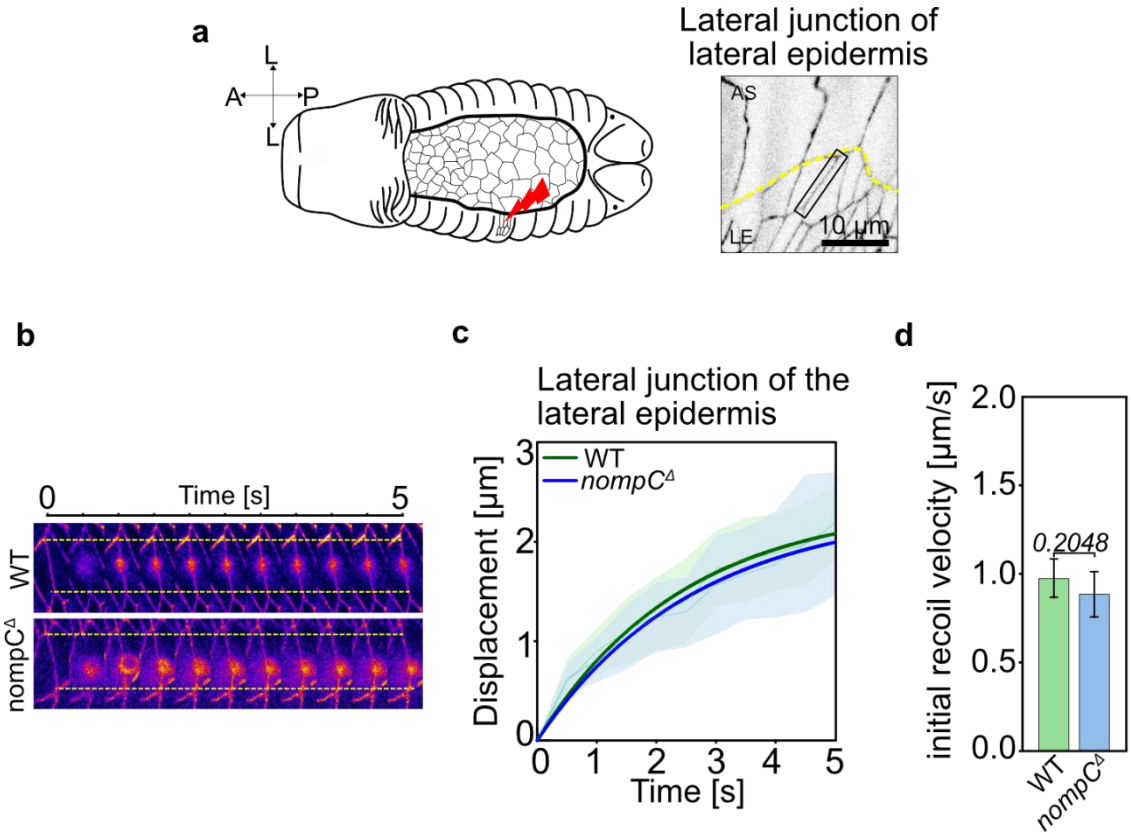

Figure 3.28. Recoil velocity at the lateral junctions of the lateral epidermis was comparable in the WT and *nompC$^{\Delta}$* embryos. a. Scheme of a dorsally posed embryo and an exemplary live image showing the lateral junctions of the lateral epidermis of the embryo. b. The kymograph for the ablation of a junction with lateral orientation. c. The trajectory of the displacement of 3X vertices followed in multiple embryos. The thin solid line indicates the mean, and the shaded area indicates the 95% confidence interval. The fitting is shown with the thick solid curve. (WT, N=10, *nompC$^{\Delta}$*, N=10). d. The bar chart shows the mean with SE of the calculated initial recoil velocity across multiple embryos. (Statistical significance was calculated by Student's t-test)

Lateral junction tension after tissue cut

I physically isolated the AS tissue from the lateral epidermis via laser induced tissue cut to distinguish the intrinsic and extrinsic contributions to the AS junction tension. Immediately after the tissue cut, I cut and probed the lateral junction tension of the AS cells, a few cells away from the tissue cut. In the WT embryos, the initial recoil velocity measured strongly decreased (<1 μm/s). Interestingly, the lateral junction tension in the *nompC*$^{\Delta}$ embryos was not significantly changed after the tissue cut, see Figure 3.29.

This suggested that the WT AS cells were responsive to the pulling force exerted by the lateral epidermis and intrinsically generated force to oppose the same. The AS tissue became loose and unresponsive as the lateral epidermis contribution was lost upon the tissue cut. On the other hand, AS cells in the *nompC*$^{\Delta}$ embryos could not sense the loss of pulling force from the lateral epidermis after the tissue cut. This indicates that the cells could not intrinsically generate force against tension exerted by the lateral epidermis. Instead, they chose to get elongated towards the direction of the lateral epidermis, as revealed by the anisotropy analysis.

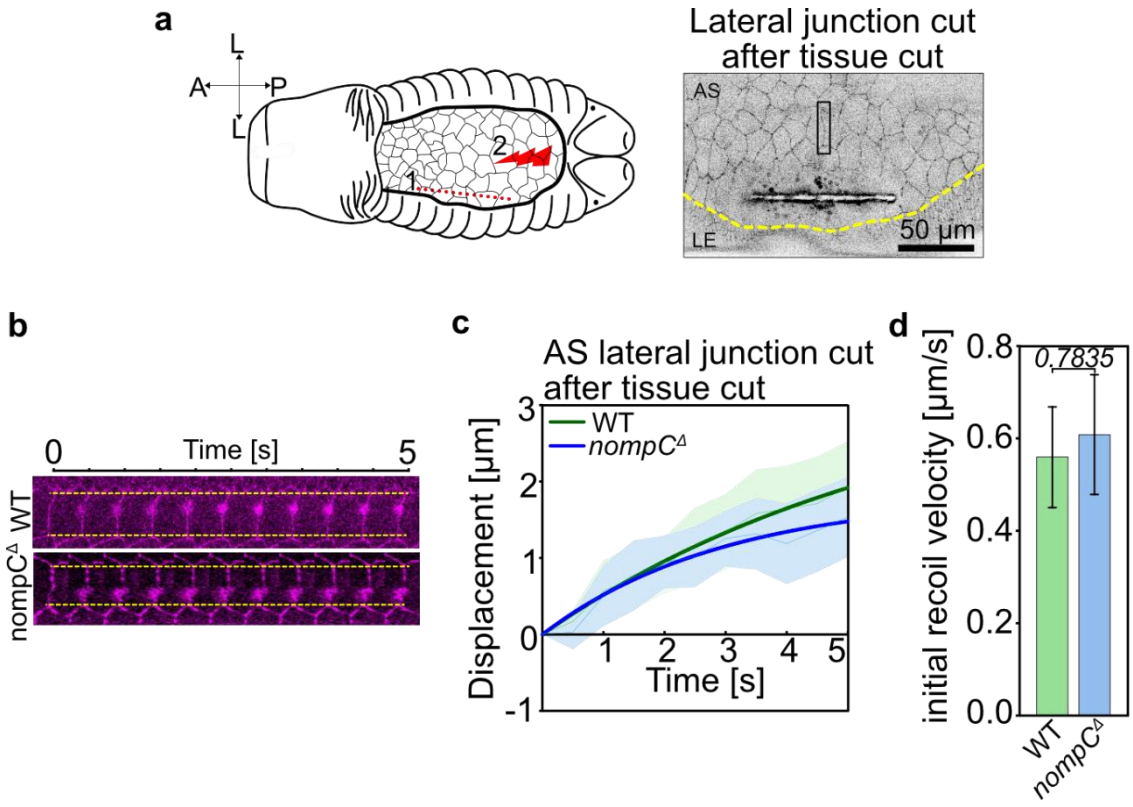

Figure 3.29. Recoil velocity of the lateral AS junctions after the isolation of LE from AS was comparable in the WT and *nompC$^{\Delta}$* embryos. a. Scheme of a dorsally posed embryo and an exemplary live image showing the target lateral AS junction after the lateral epidermis was cut off from the AS tissue. b. The kymograph for the ablation of a junction with lateral orientation. c. The trajectory of the displacement of 3X vertices followed in multiple embryos. The thin solid line indicates the mean, and the shaded area indicates the 95% confidence interval. The fitting is shown with the thick solid curve. (WT, N=11, *nompC$^{\Delta}$*, N=11). d. The bar chart shows the mean with SE of the calculated initial recoil velocity across multiple embryos. (Statistical significance was calculated by Student's t-test)

The temporal transition of tissue-wise tension distribution in the WT embryos

As in the WT embryos, the anisotropic AS cells during the elliptical phase gradually became more and more isotropic with time, I asked if the tissue-scale force distribution has some temporal factor in it. To resolve this, I cut the AS tissue axially in the middle (along a straight line of 120 µm) and performed PIV analysis to calculate the initial recoil velocity. The measurements revealed a larger initial recoil velocity at the elliptical phase than at the DC phase, see Figure 3.30.

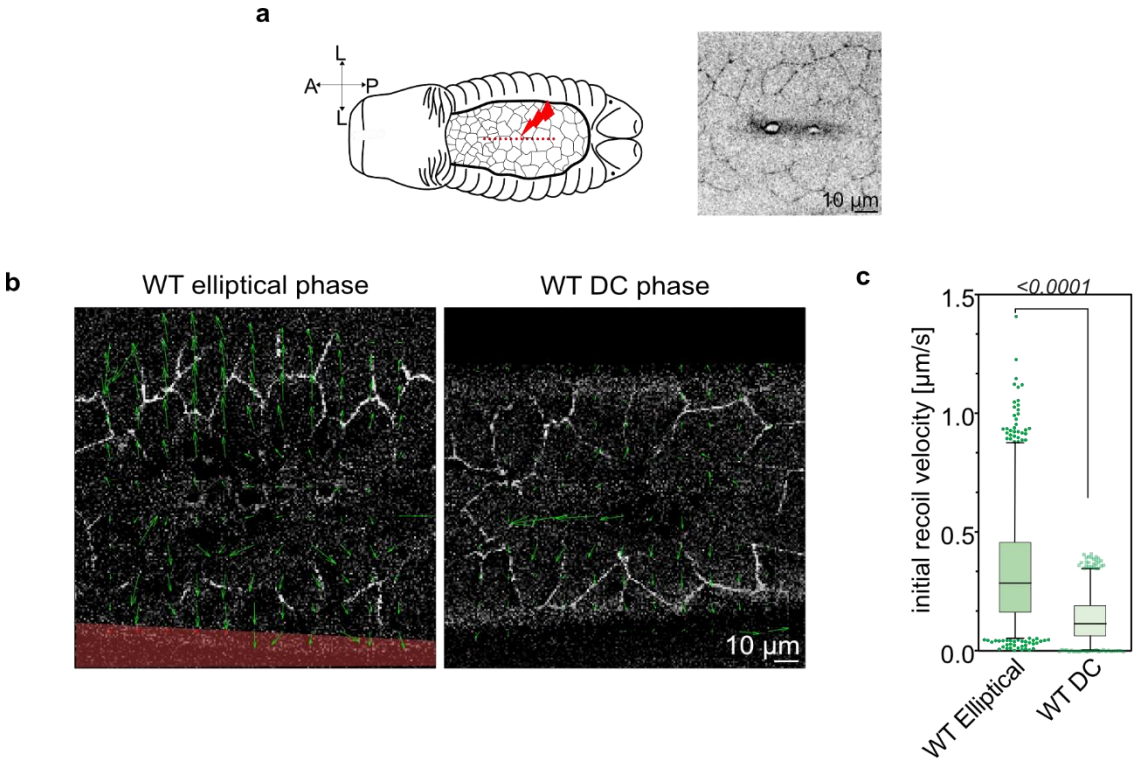

Figure 3.30. AS tissue-wide ablation of a fixed length revealed a temporal change in the tension across the tissue. a. Scheme of a dorsally posed embryo and an exemplary live image showing a 120 µm long cut in the middle of the AS tissue. b. Images from the time-lapse recording after the cut. E-CadGFP outlines cells. The green arrows indicate the velocity vectors determined by particle image velocimetry (PIV) analysis. The length of the vectors represents the magnitude of the recoil velocity. c. The bar chart shows the mean with a 95% confidence interval of the calculated initial recoil velocity across multiple embryos. (Statistical significance was calculated by Student's t-test). Five embryos from each phase, N=731 particles from the elliptical phase, and N=549 particles from the DC phase.

Loss of NompC leads to loss of temporal transition of tissue-wise tension distribution

I repeated similar ablation experiments with the *nompC*$^{\Delta}$ embryos. During the elliptical phase, the initial recoil velocity was significantly reduced from the WT. There was, however, no difference between the recoil velocities of elliptical and dorsal closure phases, see Figure 3.31. These show a lack of transition of tissue-wide tension distribution in the mutant embryos.

It is evident from the single junction cut experiments that the tension in the lateral direction was greatly reduced in the *nompC*$^{\Delta}$ embryos. The tissue-wide cutting also supports the same directionality of force distribution that was affected due to the loss of NompC.

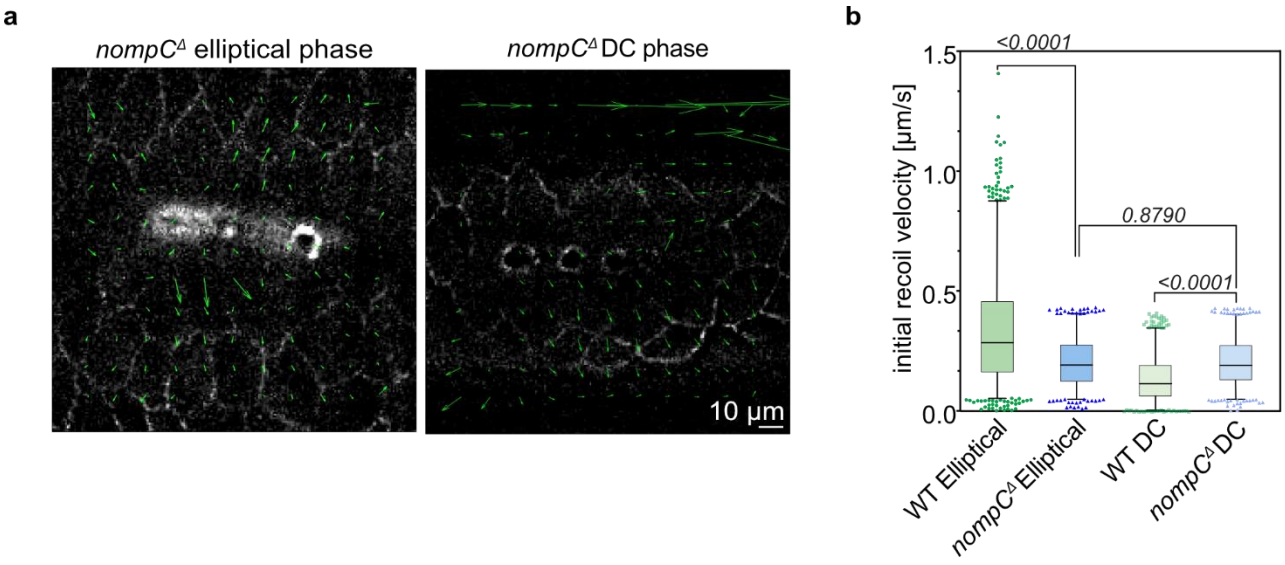

Figure 3.31. Loss of NompC leads to loss of temporal transition of tissue-wise tension distribution
a. Images from the time-lapse recording after the AS tissue cut in the *nompC*$^{\Delta}$ embryos. E-CadGFP outlines cells. The green arrows indicate the velocity vectors determined by particle image velocimetry (PIV) analysis. The length of the vectors represents the magnitude of the recoil velocity. c. The bar chart shows the mean with a 95% confidence interval of the calculated initial recoil velocity across multiple embryos. (Statistical significance was calculated by Student's t-test). Five embryos from each phase, N=431 particles from the elliptical phase, and N=475 particles from the DC phase.

3.8. Cell-cell coordination

Loss of NompC disrupts cell-cell coordination

So far, my studies are based on the assessment of parameters for single cells. But, a more direct way to study mechanical signalling is by studying the pairwise behaviour of neighbouring cells. AS tissue being a congregation of ~200 oscillating cells, holds the potential to be utilised as a model system.

To study cell-cell coordination in AS tissue, I quantified the temporal coupling of a pair of AS cells in contact. Synchronised (sync.) cell pairs showed an in-phase cortical area fluctuation, whereas the anti-synchronised (anti-sync.) pairs showed the opposite, see Figure 3.32.

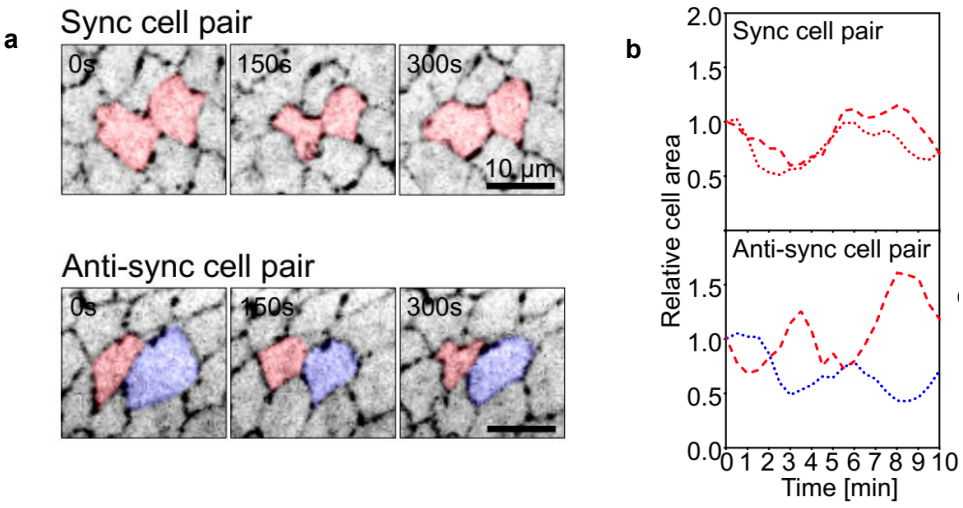

Figure 3.32. Example of pair of sync. and anti-sync. AS cell pairs. a. Two adjacent cells established sync. coupling when both of them underwent contraction and relaxation simultaneously. In anti-sync. coupling, when one cell contracts, the neighbouring cell relaxes and *vice versa*. b. Quantification of the sync. and anti-sync. coupling behaviour of AS cells. The relative area is the area of the cell normalised over the initial area of respective cells.

Hence, studying coupling between cell pairs is an effective means to study cell-cell coordination. However, quantifying all possible cell pairs (~500 per embryo, 8 to 10 embryos per genotype) over a period of 2 hours was the real challenge. Therefore, I

took advantage of the deep-learning-network-based automated segmentation approach (Cycle-GAN, designed by Dr. Matthias Haering), followed by manual proofreading and subsequent big data analysis, see Figure 3.33 for a brief overview of the operating pipeline.

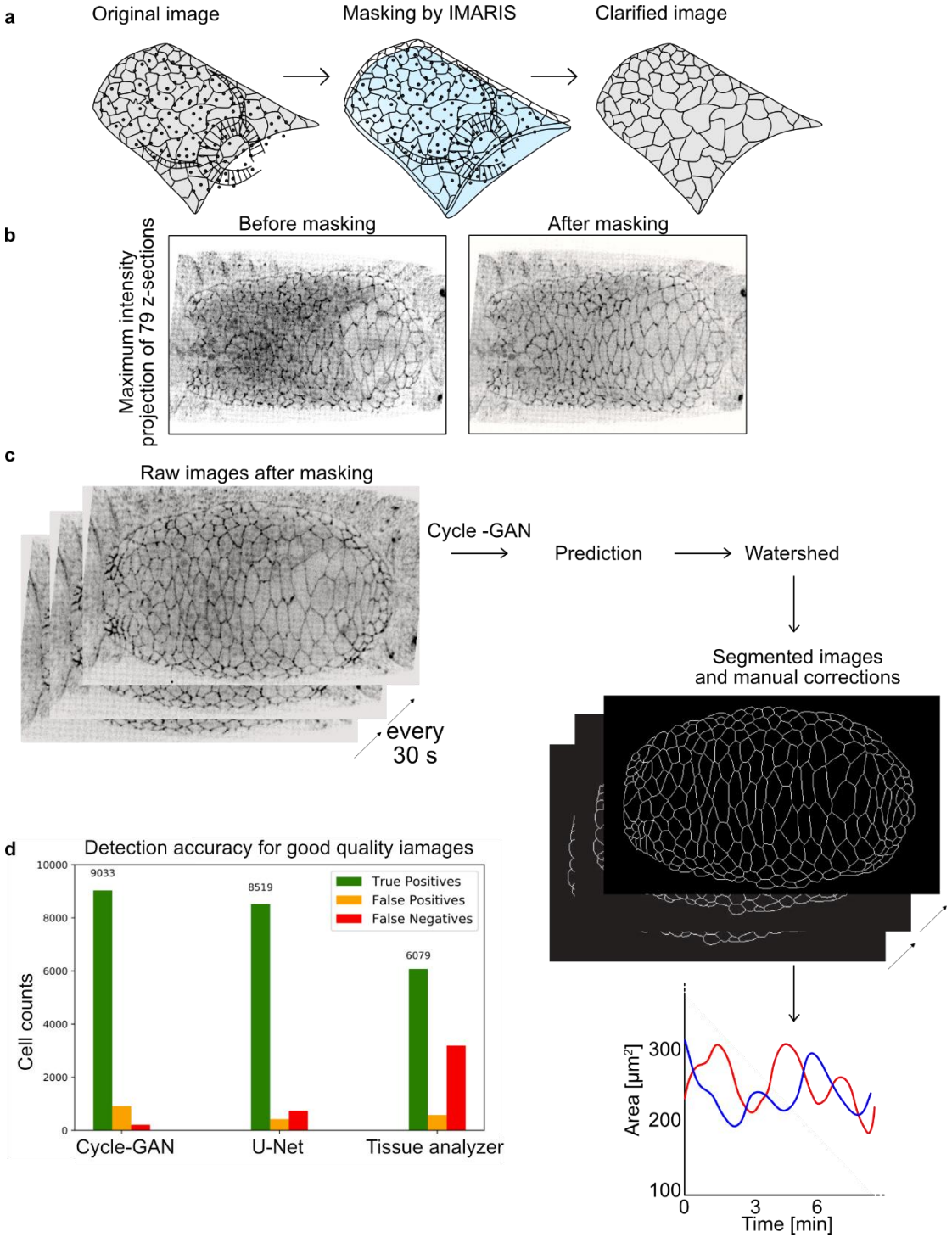

Fig 3.33. Deep learning neural network-based Segmentation approach. a. The raw 3D images were obtained by the spinning disc microscopy. The interfering signals from the yolk and gut was enclosed by a solid mask using IMARIS. The image reconstructed by masking was then maximum-intensity projected to convert into 2D and ready-to-use. (done by me) b. An example showing 2D projected AS tissue before and after masking. Masking reduces the signal/noise ratio to a great extent. c. Example of an entire AS tissue during the elliptical phase of WT embryos (maximal intensity projected) for each time-point. Two time points had an interval of 30 s. The flow chart describes the pipeline for computational image analysis and segmentation by cycle-consistent generative adversarial networks (GAN). Like artificial intelligence, the program undergoes a self-training with manually created ground truth images to attain proficiency in segmenting cell junctions, in our case. The segmented images were thereafter used for the tissue-scale analysis of cellular dynamics. d. Tracking performance was compared between Cycle-GAN segmentation and two classical methods (U-Net and watershed-based segmentation from the Tissue Analyzer) during AS oscillations. Cycle-GAN minimises the occurrences of false positive (adding a false cell junction) or false negative (ignoring a genuine cell junction) cell tracking. With manual proofreading at the end of the pipeline (done by me), the tracking reaches >90% accuracy. (Adapted and modified from (Häring *et al.*, 2018)

The intercellular coordination of oscillating AS cells was analysed using iso-correlation subsampling to characterise the coupling types of AS cell pairs. Maximal subsamples exhibiting positive or negative correlations were selected from the entire population of the reconstructed cell pairs. The cell pairs physically sharing the cell junctions were positively (correlated), negatively (anti-correlated), or neutrally coupled. Without coordination between a pair of cells, the correlation coefficient (c) is 0, whereas sync. pair is assigned by any value of c between 0 to 1. Anti-sync. pairs, on the contrary, have $-1 < c < 0$. The value of c also reflects the strength of the coupling. Using this principle, I compared the sync. and anti-sync. populations of WT and *nompC*$^{\Delta}$ embryos. Figure 3.34 summarises my observation.

Neutral population denotes the cells that were neither positively nor negatively synchronised throughout the elliptical phase (insignificant). Only cell pairs having a consistent sync. or anti-sync. nature were considered significant. Though the fraction cells that were coupled (significant to insignificant ratio) did not change much in the *nompC*$^{\Delta}$ embryos, the coupling strength (inferred from sync. to anti-sync. ratio) dropped with certitude.

a

Type	Sync.	Anti-sync.	Neutral	Sync. / Anti-sync.	Sig. / Insig.
WT	1207	725	6659	1.66	0.29
nompC$^{\Delta}$	649	834	4918	0.77	0.30

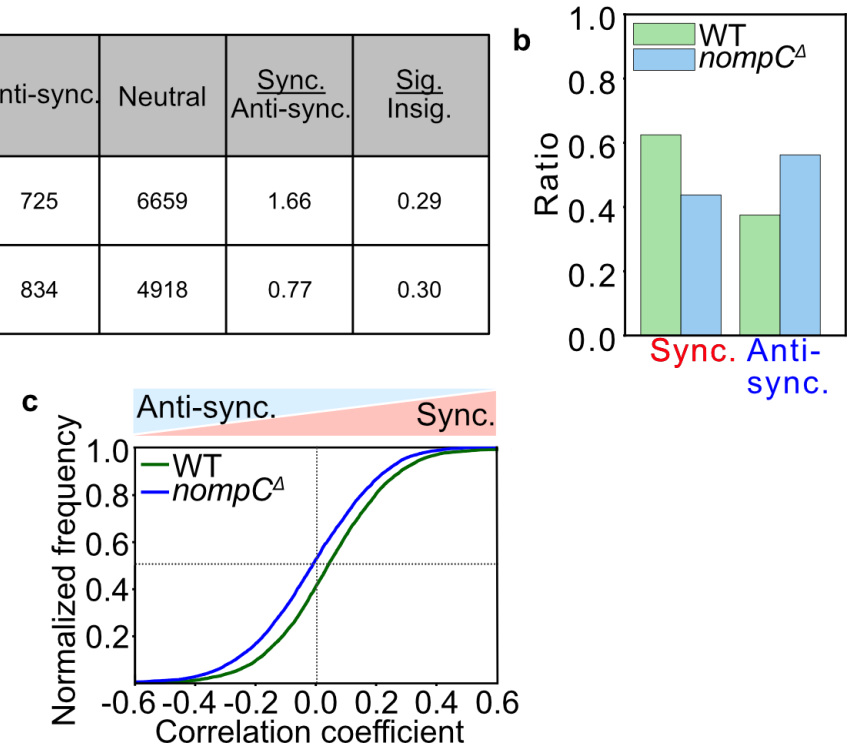

Figure 3.34. Intercellular coupling between cell pairs was affected due to a lack of NompC. a. Table showing genotypes and the number of samples analysed. The neutral coupling means statistically insignificant coupling. Only statistically significant couplings were grouped into two categories, i.e. sync. and anti-sync. b. Bar diagram representing the ratio of sync. and anti-sync. coupling among cell pairs with statistically significant coupling. c. Cumulative distribution of the correlation coefficients of all the cell pairs computed over the entire elliptical phase of AS. (WT, N=10; *nompC*$^{\Delta}$, N=8 for all the morphometric and morphodynamic analysis)

Spatial distribution of coupling types was affected in *nompC*$^{\Delta}$ embryos

Interestingly, the coupling types were not uniformly distributed over the WT AS tissue. The correlation coefficients were calculated and averaged over all 8-10 embryos. If there had been no spatial patterning of coupling types, no hotspots should exist upon averaging. However, there were hotspots where the probability of finding sync. pairs were significantly higher than finding anti-sync. pairs and *vice versa*. In the WT embryos sync. pairs (red) appeared mostly at the anterior half of the tissue, whereas

in *nompC*$^{\Delta}$ ones, this population was lost and replaced by anti-sync. (blue) region. To assess the specificity of the patterns, the coefficients were averaged after scrambling their positions *in silico*. Upon randomisation, the hotspots still persisted, confirming the spatially separate existence of two different types of coupling populations, see Figure 3.35.b.

To assess the significance of the observed pattern, pixel-wise confidence intervals for the correlation maps were calculated using bootstrap subsampling over multiple embryos. This indicated that the anterior sync. patterns in WT and overexpression of anti-sync. patterns in *nompC*$^{\Delta}$ were indeed statistically significant, see Figure 3.35.c.

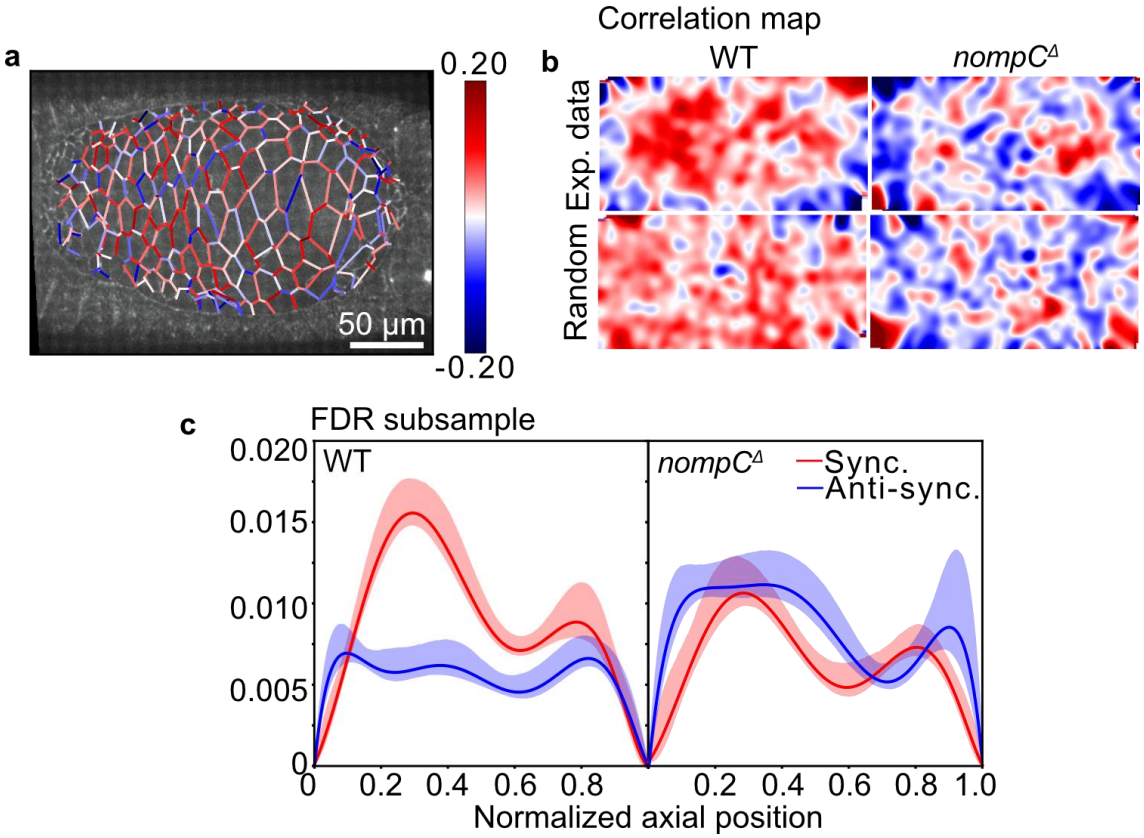

Figure 3.35. The loss of NompC led to the loss of spatial distribution of coupled cell population. a. Assignment of the correlation coefficient to the cell junctions shared by a pair of AS cells. Single AS tissue with colour-coded junctions according to the correlation coefficients averaged over the whole movie. The scale indicates the strength of coordination. b. Maps with all correlation coefficients averaged over each genotype. Colour coding represents average correlation. To interpret the specificity of the

pattern, coefficients were averaged after scrambling the positions, so-called randomisation. c. A subsample of cell pairs was picked up by controlling the local false discovery rate (FDR subsample). Spatial density profile of FDR subsampled pairs. Confidence bands were computed via bootstrapping over embryos.

CHAPTER 4: Discussion

4.1. Mechanosensitive ion channel NompC is expressed in AS epithelial cells in *Drosophila*

Mechanosensitive ion channels are integral membrane proteins that are responsible for transducing mechanical forces (tensile, compressive, shear) either from the lipid bilayer or from the cytoskeleton. They are evolutionarily old and ubiquitously present from archaea to bacteria to eukaryotes (Haswell *et al.*, 2011). Since their pioneering discovery in eukaryotic cells, till today scientists have been investigating their molecular structures and biophysical principles underlying the gating mechanisms (Cox *et al.*, 2019). But most of the research had been carried out in specialised mechanosensory neurons, mainly in the context of sensory neurobiology (Ranade *et al.*, 2015). However, there roles in epithelial cells are not well characterised except a few experiments documenting their presence and the ion conductance activity in cell lines (Li *et al.*, 2015) and in adult midgut cells (Gong *et al.*, 2023). However, their function in epithelial cells in early embryonic development has yet to be explored in detail.

NompC is one of the earliest identified mechanogated channels belonging to the TRP superfamily, that plays crucial roles in sensation of gentle touch, hearing, balance and locomotion of *Drosophila* larvae and adult flies (Wang *et al.*, 2021). When I expressed EGFP-tagged NompC in *Drosophila*, I found the bright distinguishable signals from the typeIII chordotonal neurons, as it was reported to express NompC (Figure 3.2.a,b). As per Fly cell atlas project, the gene is also expressed in various epithelial and epidermal cell types in medium quantity (http://flybase.org/reports/FBgn0016920.html).

NompC is structurally unique with its 29 ankyrin repeats-long helical cytoplasmic domains (Jin *et al.*, 2017; Zhang *et al.*, 2015). The active NompC channels are formed by cluster of 4 proteins. Because the signals were sparsely distributed, compared to the large dimension of AS cells. I detected clusters of GFP signals in the AS cells. Some of these clusters were highly dynamic. The distribution was on or around the cell junctions (marked with ECad-mTomato) (Figure 3.3). However, because the cells and channel proteins were highly dynamic, there was a technical shortcoming and a resultant delay between imaging the two channels (GFP and mTomato). Both the

channels were imaged in 10 s. From both the fixed (Figure 3.4) and the live embryos, it was clear that the proteins were largely distributed along the junctions and also on the cortex.

4.2. Absence of NompC leads to poor survival and developmental defects

In the homozygous situation, the point mutations (*nompC^{1}* and *nompC^{3}*) of *nompC* were previously identified to cause larval lethality at the third instar stage, while *nompC^{1}* showed a stronger phenotype by showing larval lethality at the first instar stage (Hunter, 2012). However, the exact defective phenotypes causing the lethality in these stages were not documented by previous researchers.

For my experiments, I used *nompC$^{\Delta}$* flies, where the whole *nompC* gene is deleted and replaced by *attp::loxP*. As expected, I could not find any surviving adult flies in the vials of fly culture. The heterozygous flies were balanced over CyO, twi>GFP. I generated the germline clones to get homozygous embryos devoid of both maternal and zygotic contribution of the NompC protein. When the maternal-zygotic null ($m^{-/-}z^{-/-}$) embryos were raised together with maternal null-zygotic heterozygous ($m^{-/-}z^{+/-}$) ones in the same vial, only the $m^{-/-}z^{+/-}$ flies ecclosed as adults.

In order to investigate the lethal phenotype more carefully, I raised the $m^{-/-}z^{-/-}$ and $m^{-/-}z^{+/-}$ embryos separately on different agar plates. All the $m^{-/-}z^{+/-}$ embryos hatched, and most of the $m^{-/-}z^{-/-}$ hatched as well, with only ~3% embryonic lethality (Figure 3.7). I collected all the unhatched embryos and did the cuticle preparation. They showed a spectrum of cuticle defects ranging from cuticular holes to disorganised denticles to defective head skeletons (Figure 3.10). In summary, as opposed to point mutants, *nompC$^{\Delta}$* flies show that during early embryonic development, the penetrance of the lethal phenotype caused by the absence of NompC is not so high, and the expressivity is also diverse, causing multiple phenotypes. The cuticle hole phenotype was common in ~50% of the unhatched embryos, indicating compromised epithelial integrity (Bachmann *et al.*, 2001).

Out of the hatched $m^{-/-}z^{-/-}$ larvae, more than half of them were lethal in larval or pupal stage. Adult escapers, however, were unable to move or fly, let alone mating (Figure 3.8.b). Also, they showed severe twitching phenotype, indicating to the critical

role of NompC in the sensory nervous system. The overall time required from egg-laying to ecclosion also increased by 5-10 days than the WT, indicating a comparatively slowed down developmental processes in $m^{-/-}z^{-/-}$ flies.

From these assays, I infer that the absence of NompC is a classic example of biological competition. When raised with the zygotic rescued flies, there are no adult $m^{-/-}z^{-/-}$ flies in the vials. But, when raised separately, ~38% of flies escaped the lethal fate. It shows that the $m^{-/-}z^{-/-}$ flies are weaker and outcompeted by the zygotic rescued ones.

4.3. Depletion of NompC leads to perturbed touch sensitivity

NompC was described to transduce mechanical stimuli, including tactile and sound and vibrational signals in *Drosophila* larvae (Zhang *et al.*, 2013). Mutant larvae show defective response to touches, and adult flies show complete loss of mechanoreceptor potential in the bristles. Premature nonsense mutants (*nompC*^{1}, *nompC*^{2}, *nompC*^{3}) led to a complete loss of mechanosensory currents. Missense mutant (*nompC*^{4}) resulted in faster adaptation kinetics for adult flies. Response to sounds or vibrational stimuli was significantly perturbed in adults and larvae of *Drosophila*.

In order to measure gentle touch sensitivity in $m^{-/-}z^{-/-}$ larvae, I followed the same protocol used by Kernan *et al.*, 1994 (Kernan *et al.*, 1994). They used this method to test the touch sensitivity in the larvae mutant for uncoordinated (unc) and uncoordinated-like (uncl) genes. Using the same assay, scientists studied the role of DmPiezo in mechanical nociception (Kim *et al.*, 2012). Though the response to noxious stimuli were affected in the absence of Piezo, gentle touch sensation was observed to be normal.

I deployed this simple assay and found that the $m^{-/-}z^{-/-}$ larvae showed a highly reduced (~4 times) response to gentle touch compared to both the WT (OrR) and the $m^{-/-}z^{+/-}$ ones (Figure 3.9). There was no significant difference in behavioural response between the WT and zygotic rescued larvae. The $m^{-/-}z^{-/-}$ larvae showed an usual curling phenotype without any stimulation. Instead of moving in a straight line, they were stuck in one place, curling around and hitting their own body (Figure 3.8.a).

It was reported that in the *Drosophila* larvae, the body wall is tiled by the class III and IV of sensory neurons. DmPiezo is enriched in class IV neurons and is responsive to noxious stimuli. NompC, on the other hand, is highly expressed in class III neurons and is required for gentle touch sensation. NompC, when ectopically expressed in class IV neurons, turned them touch-sensitive (Yan *et al.*, 2013).

My experiment with the null allele confirms the previous observation by the other groups using point mutations and further describes the touch-insensitivity phenotype in detail. Based on my observations, it would be an interesting model for neurophysiologists to study nociception both in larvae and adults. It is worth looking into the expression of NompC in muscles (though expressed in low quantity in muscles based on Fly cell atlas project) as well and if it controls the nerve-muscle coordination.

4.4. NompC is an essential regulator of the dorsal closure

Because absence of NompC does not cause an absolute lethality at the early embryonic development, but an array of cuticle phenotypes in unhatched embryos, I went on to investigate this further. Mutation in the mechanosensitive DEG/ENaC ion channel subunit *Ripped pocket* (*rpk*) was reported to affect both germband extension and DC (Hunter *et al.*, 2014) in *Drosophila*. I recorded time-lapse DIC images of embryos to investigate the early developmental stages. I measured the length of germband extension phase. I found no significant difference in the $nompC^{\Delta}$ embryos from the WT control. However, only one in 13 $m^{-/-}z^{-/-}$ embryos observed failed to complete germband extension and the subsequent phases.

Hunter *et al.* previously reported essential roles of two ion channels, namely *ripped pocket* (*rpk*) and *dtrpa1* during the DC process in *Drosophila*. Blockade of these channels led to defective force generation via actomyosin structures (Hunter *et al.*, 2014). Acute knockdown of *nompC* by amnioserosa-specific Gal4-driven *nompCRNAi* expression could not cause embryonic lethality or morphological defects during DC . However, the RNA interference is not the choicest way to suppress the gene of interest, sometimes it has off-target effects (Chen *et al.*, 2021). Also mere zygotic knockdown in AS tissue is likely not sufficient for *nompC*, as even the zygotic rescued ($m^{-/-}z^{+/-}$) embryos did not show a lethal phenotype.

Taking these information on background, I recorded time-lapse images of the *nompC*$^{\Delta}$ embryos, having cell junctions marked with Ecad-GFP. I found no significant difference in the duration of germband extension between the WT and *nompC*$^{\Delta}$ embryos. I, then, tracked the entire GBR phase until the end of the DC phase. I detected multiple morphogenetic changes, including incomplete GBR, no or ectopic formation of canthi, unusually stretched AS cells, and complete dissociation of AS from LE tissue as the worst-case scenario (Figure 3.12). The rupture of tissue occurred only one in five embryos. Instead of the other morphogenetic defects, other embryos could complete the DC successfully. These observations made me think that the force distribution across the AS tissue is affected in the absence of NompC.

The onset of DC phase is marked by the merging of two actin cables from both sides of the embryo at the anterior end. I measured the rate of how fast the two cables meet each other. In the *nompC*$^{\Delta}$ embryos, the speed of anterior-end convergence was significantly (~1.5 times) faster than that of the WT. However, the width of the AS tissue remained comparatively higher than the WT during the entire elliptical phase (Figure 3.13). This means that the AS tissue undergoes DC without spending the time required in the elliptical phase, indicating a lack of orchestration in tissue dynamics.

4.5. NompC regulates Ca^{2+}-influx in AS cells

I then asked if NompC acts as a channel in AS cells, and if yes, what response it shows to external mechanical stimuli.

Transient receptor potential (TRP) channels, in general, act both as a Ca^{2+}-channel and a nonselective cation channel influencing voltage-gated or store-operated influx of Ca^{2+} (Vangeel and Voets, 2019). NompC is at least 2 times more permeable to Ca^{2+} than the monovalent cations (Na^{+}, K^{+}, Cs^{+}) (Li *et al.*, 2021). Chordotonal class III neurons of *nompC* heterozygous point mutant larvae do not respond to a low level of sound vibration that was otherwise sufficient to trigger a Ca^{2+} response in a WT counterpart (Zhang *et al.*, 2013). However, a higher sound intensity can elicit a response, revealed by Ca^{2+} imaging, but not as much as the WT, holding the possibility of some redundant channel activity.

I used myristoylated (membrane-bound) GCaMP7s (Zhang *et al.*, 2023) as a live Ca^{2+}-sensor driven by tubulin-Gal4 to image the Ca^{2+} in AS cells. Without any mechanical manipulation, I compared the basal level of GCaMP7s signal intensity in the AS cells of the WT and *nompC$^{\Delta}$* embryos. The signal in the *nompC$^{\Delta}$* embryos was significantly decreased (Figure 3.14). This shows that NompC has a constitutive channel activity in the AS cells.

Epithelial wound results in an immediate rise of cytosolic Ca^{2+} in the wounded cell (Antunes *et al.*, 2013; Sammak *et al.*, 1997). This is followed by a spreading of Ca^{2+} waves to the neighbouring cells. In *Drosophila* wing disc epithelium, such Ca^{2+} waves are generated by applying mechanical pressure that facilitates opening of mechanogated Ca^{2+} channels (Restrepo and Basler, 2016). Laser-induced ablation of single cell of *Drosophila* pupal abdominal epithelium, causes a propagation of Ca^{2+} wave in a circular fashion across the neighbouring cells (Lehne *et al.*, 2022). Previous experiments in our lab showed a significant reduction of Ca^{2+} response in the neighbouring AS cell junctions of embryos mutant for TMC, a putative mechanogated channel (Richa, 2019).

I did laser-induced wounding of single AS cells in the WT and *nompC$^{\Delta}$* embryos and measured the Ca^{2+}-dynamics at the neighbouring cell junctions with a 5s interval. There is a sharp increase in relative intensity (after/before wounding) followed by an exponential decline in the WT AS cells. In the *nompC$^{\Delta}$* embryos, the rise in Ca^{2+} intensity was ~4 times less than the WT (Figure 3.15). This showed that the NompC is indeed important for the epithelial cells to respond to a mechanical stimulus.

4.6. Mechanical communication among epithelial cells depends on NompC

I asked if NompC acts as a mechanosensitive channel in the AS cells. If it does, the mechanical signal transmission between neighbouring cells must be affected in absence of NompC.

Wounding is a strong mechanical perturbation to which the neighbouring epithelial cells respond by migrating, proliferating or intercalating to facilitate healing (Leoni *et al.*, 2015; Zechini *et al.*, 2022). Experiments by Dr. Deqing Kong in our lab

showed that the neighbouring AS cells stopped or slowed down oscillation following laser-induced junction ablation.

I performed laser-induced ablation of single AS junction per embryo and tracked the oscillation amplitude of the neighbouring cells in the WT. I also followed the same of the next-to-next neighbours to estimate the span of mechanical coupling and cells far away from the site of ablation as internal control. I observed the area variance (for the first 3 mins post-wounding) of the neighbouring AS cells reduced significantly compared to the control cells. Next-to-next neighbours behaved more or less similar to the control cells. This indicates that the immediate neighbouring cells are most sensitive to a wound in AS epithelium (Figure 3.17.b,c).

When I repeated the same experiment with the *nompC$^{\Delta}$* embryos, I found that the area variance of the immediate neighbours was comparable with that of the control cells. However, the area variance or the oscillation amplitude of the control cells itself was significantly lower than their WT counterparts. Also, after ~3 minutes, while the WT cells almost recovered to continue their oscillation, the *nompC$^{\Delta}$* cells never failed to recover again. These results suggest that in absence of NompC, neighbouring cells failed to respond to the mechanical input in the tissue (Figure 3.17.c,d). It may also be possible that the intrinsically low oscillation amplitude does not allow the variance to drop further down, leaving room for ambiguity.

I observed the wound-healing process for a span of 15 minutes post-wounding. I measured the area of the wounding site (involving two cells) for 15 minutes after the junction cut. In the *nompC$^{\Delta}$* embryos, there was a sudden increase in the wounding area after the cut, followed by an exponential decrease. In the WT, the area decreased continuously after the injury (Figure 3.17.b). This suggests that the energy released due to the wounding takes more time to dissipate in the absence of NompC, causing an initial inflation of area. Viscoelastic dissipation has been reported to stabilize the cell shapes during tissue morphogenesis, however, the exact molecular mechanism remains to be an open question (Clément *et al.*, 2017).

Thereafter I also measured the anisotropy of the cells neighbouring the wound (Figure 3.18). In the WT embryos, the cells decreased oscillation and gradually attempted to repair the wound. However, their shape did not change significantly over time. In the *nompC$^{\Delta}$* embryos, on the other hand, the cells elongated toward the

wounded site in order to close it. I observed an abnormal incidence of cell intercalating at the wound edge. Combined, this results suggests an increased fluidization of the cells, that was previously reported for an impaired wound healing process and a subsequent loss of epithelial integrity (Zechini *et al.*, 2022). I observed that it is not only the neighbouring cells that became anisotropic to cause wound healing, but the control cells in the *nompC*$^{\Delta}$ embryos also remained more anisotropic than their WT counterparts. This impelled me to analyse this anisotropic morphometry in further detail.

4.7. Isotropic cell shape transition before DC depends on NompC

AS cells are highly anisotropic in the WT embryos after the germband retraction phase. However, there is a slow transition from an anisotropic to isotropic cell morphology as the embryos approach to the DC phase. AS cells in the *nompC*$^{\Delta}$ embryos remained anisotropic even after the complete retraction of the germband and dorsal-ward movement of the AS tissue (Figure 3.19-21). The anisotropy was toward the lateral epidermis from both the sides of the AS tissue. There was also a spatial difference between anisotropy among the AS cells. Though the cells in the middle of the tissue failed to adapt to an isotropic morphology over time in the absence of NompC, the cells at the periphery stayed comparatively isotropic, same as the wild type embryos. It is not surprising that the peripheral cells despite having the same genotype as the middle cells behaved differently. As the morphogenesis involves two highly dynamic tissues exerting and experiencing forces from each other, the spatial differences in the cell shape could be simply influenced by a position-dependent manner.

In the WT embryos, as DC progresses there is an increase in the contractile forces from the AS tissue resisting the pulling forces from the lateral epidermis. This intrinsic forces from the AS cells somehow enables the cells to adapt to an isotropic morphology in the WT embryos. The anisotropic morphology in the absence of NompC, suggests either an increase in the pulling force from the lateral epidermis or a decreased counteractive contraction of the AS cells. The anomalous DC phenotypes are possibly because of the force imbalance due to a loss of communication between the two epithelial tissues.

Interestingly, individual loss of two more ion channels Tmc and Piezo also caused an anisotropic AS cell morphology, however to a lesser extent (revealed by other colleagues in our lab).

4.8. NompC is a vital regulator of AS cell contractility

Contractile activity of epithelial cells mainly depends on the unique capacity of non-muscle II to form filaments sliding movement of which along the actin filaments propels contraction (Verin and Bogatcheva, 2006). In order to drive an oscillatory cell behaviour, there must be a robust mechanism for force sensing, transduction and response. In the presence of mechanical stimuli, the cells can intrinsically drive generation of forces via the sub-cellular organisation of the contractile cytoskeletal meshwork (Martin and Goldstein, 2014; Solon *et al.*, 2009). In the AS of *Drosophila*, reducing myosin activity prevents cell shape oscillation and eventually DC. Increasing myosin activity, on the contrary, increases the oscillation amplitude of the AS cells and promotes DC (Duque and Gorfinkiel, 2016).

Cycle-GAN-based temporal reconstruction of the entire AS tissue allowed the big-data analysis of dynamic cell behaviour of the ensemble of AS cells. The major period of the oscillation of the cross-sectional area of the AS cells was determined via autocorrelation function. The cell oscillation was faster in the AS cells of NompC-depleted embryos. Faster oscillations suggests that the cells are unable to induce efficient cell contractions and relax sooner. This may be due to a less actomyosin assembly or a reduced stability of the actomyosin foci.

When I compared the oscillation amplitude (in terms of area variance) of all the AS cells during the elliptical phase, for the $nompC^{\Delta}$ embryos, it was significantly lower than the WT ones (Figure 3.22.c). Then, I measured the area change and an associated myosin oscillation in a few AS cells. In the absence of NompC, the myosin pulses are less strong to drive an equivalent area change as in the WT AS cells (Figure 3.22.a,b). The average AS cell area was higher in the $nompC^{\Delta}$ embryos (Figure 3.13.g) and previous studies showed that cell area and contractility is inversely proportionate in AS cells (Fischer *et al.*, 2014).

It was reported that local Ca^{2+} flashes induce Rho flares that drives epithelial cell contraction in *Xenopus laevis*. Inhibition of mechanosensitive ion channels, reduces the amplitude of Ca^{2+} flashes and the Rho flares (Varadarajan *et al.*, 2022). Laser-induced uncaging of chelated-Ca^{2+} in *Drosophila* AS cells drives cell contractility via non-muscle myosin II activation (Kong *et al.*, 2019). I found that the intrinsic as well as wound-induced increase in Ca^{2+} significantly reduced in the absence of NompC channel. Taken together, I infer that NompC, being a Ca^{2+} channel is an important regulator of the myosin and the resultant contractile activity of the AS cells. By establishing Ca^{2+}-sensor lines, I am trying to find a direct correlation between Ca^{2+} influx and the epithelial cell contractility. As a first step to establish an approach, I have already found a positively correlated pattern of Ca^{2+} dynamics (using TubGal4>MyrGCaMP7s) and the cell area oscillations in the AS tissue (Figure 3.16). Currently I am investing my time to generate a transgenic line constitutively expressing Myr-GCaMP8s, a more sensitive Ca^{2+}-sensor (Zhang *et al.*, 2023) under the Ubi-promoter. My aim is to record sufficiently good quality movies of the AS cells the junctions of which can be segmented based on the raw GCaMP signal. This will end the need for another Ecad-based fluorescence marker for the cell junctions and will avoid the technical issues with the time lag while imaging two channels.

I showed that NompC drives Ca^{2+} influx in response to external mechanical stimuli. To resolve whether it is the channel function only or some other mechanism that is responsible for the downstream effects on cell dynamics, I am currently generating a transgenic line with a single point-mutation at the pore-forming region of NompC. This mutation was previously reported to impede the channel activity of NompC (Yan *et al.*, 2013). I am taking advantage of prime-editing-based genetic-engineering technique to achieve the goal.

4.9. Altered actin network organisation in the absence of NompC

Actomyosin networks are some of the most important force-generating and force-transmitting components present in the developing tissues. Two of the most relevant structural archetypes of these actomyosin networks are 1. pulsatile, highly

dynamic populations, 2. filamentous actin with higher stability (Miao and Blankenship, 2020).

The overall cortical density of the actomyosin network was higher in the WT AS cells. I detected actin populations were not limiting to the cortical surface of the cells only. In the WT embryos, they were distributed almost uniformly across the entire depth of the cells. However, the basolateral as well as the cortical populations of actomyosin was certainly decreased in the cells of the *nompC*$^{\Delta}$ embryos. I detected more filamentous actin on the cortical surface of the anisotropic AS cells devoid of NompC. In the WT AS cells the medioapical actomyosin aggregates and not the filamentous protrusions were more prominent (Figure 3.23-24).

Super-resolution imaging of the actomyosin networks in the dynamic AS cells showed a randomly organised dense medioapical actomyosin in the AS cells of isotropic morphology. In the anisotropic cells, on the contrary the networks are more parallel and conspicuously dispersed (Moore *et al.*, 2022). Another work by Lehne *et al.* suggests that Ca^{2+} bursts are essential for switching stable actin crosslinks into transient ones (Lehne *et al.*, 2022). Loss of Ca^{2+} influx in the absence of NompC may be a reason why the stabler cortical actin protrusions persist in the AS cells the *nompC*$^{\Delta}$ embryos. However, this needs more experiments to confirm. Imaging of Ca^{2+} dynamics in unperturbed AS tissue will be the first step to answer our query.

My observation gives hints why the contractions were unstable, reflected by the shorter time period of oscillations, in the AS cells of the *nompC*$^{\Delta}$ embryos, having the medioapical actomyosin, the principal driver of contraction hugely compromised. The filamentous actin population, at the cell cortex of the *nompC*$^{\Delta}$ embryos, provides clue as how the oscillation amplitude of the AS cells severely decreased all throughout the elliptical phase of the embryo. These fibers, supposedly acting as stress fibers, limit the degree of freedom for the cortical area oscillation. My findings also support the previous observation by Dehapiot *et al.* that only larger AS cells have visible actin bundles (Dehapiot *et al.*, 2020) and my observation that the AS cells of *nompC*$^{\Delta}$ embryos are larger than the WT ones (Figure 3.13.g).

4.10. NompC regulates tubulin orientation in the direction of cell anisotropy

It is not just one cytoskeletal component but a concerted cross-talk between them determines cell shapes and their functions (Dogterom and Koenderink, 2019). Microtubule orientation was reported to be in alignment with the cell shape in multiple epithelial tissues of developing *Drosophila* embryos (Gomez *et al.*, 2016). A recent study established that the microtubules are not just passive structural component in the cell, but actively bears compressive forces. The same group also deciphered the Ft-PCP signalling pathway is responsible for coupling the microtubules at the adherens junctions (Singh *et al.*, 2018). Work by Dr. Kong and colleagues of our lab showed an increase in microtubule amount in the LE but not in the AS during dorsal closure. This helps the LE bear a part of the mechanical pull from the AS (Lv *et al.*, 2022).

When I stained the WT *Drosophila* embryos with α-tubulin antibody, I found a striking difference in microtubule orientation in the AS cells during the elliptical phase and the DC phase. During the elliptical phase microtubule filaments are oriented toward the LE conforming to the angle of anisotropy of the AS cells. However, in the DC phase, as the AS cells become more isotropic, the microtubules accordingly adapt to a more random architecture. Loss of NompC affects this transition of microtubule orientation from the elliptical to DC phase. The microtubules remained oriented laterally in the AS cells of embryos undergoing DC. As the cell shape transition is affected in the absence of NompC, microtubules as the main structural component of the cytoskeleton follow the same (Figure 3.25).

My data suggests a critical role of NompC in randomizing the microtubule orientation during DC. We know that NompC interacts with microtubule by its cytoplasmic ankyrin-repeat helices. The gating relies on the compressive force exerted by the microtubules (Liang *et al.*, 2013; Sun *et al.*, 2019; Wang *et al.*, 2021). Taken together, it is possible that the establishment of isotropic cell shape depends on the efficient force sensing by NompC via its interaction with the underlying microtubules.

4.11. NompC facilitates directional force distribution across the AS cells

Cells in developing tissue are subjected to multiple morphogenetic forces and topological constraints that in turn regulate the shape and fate of the cells (Rauzi and Lenne, 2011). Hence, cell morphology often reflects the internal or external forces that the cells are subjected to (Hara *et al.*, 2016). Recent works also showed that cell shape does not only represent the history of physical and chemical signals that the cells encounter, but also can regulate cellular phenotype through a tension-independent mechanism (Ron *et al.*, 2017).

The anisotropic shapes of AS cells during the elliptical phase led us to think whether the forces experienced by the cells are also anisotopically distributed. I applied a laser-induced junction ablation approach to estimate the tension the junction is subjected to. I cut the junctions oriented axially (toward the anteroposterior) and laterally (toward the LE). In the WT embryos, the lateral junction tension was more than the axial junction tension. This can be explained easily by the stretched morphology of the AS cells towards the lateral direction. A higher recoil velocity in the lateral junctions can be interpreted as either more tension or less friction experienced by them. But as the viscoelasticity was comparable for both directions, it is evident that the lateral junctions are under higher tension than the axial ones (Figure 3.26).

In the *nompC*$^{\Delta}$ embryos, the situation is reversed. Although the cells are more anisotropic and remain so all along the DC phase, it is surprising to note that the lateral junction tension is, in fact, significantly higher than the axial junction tension (Figure 3.27). The colleagues of our lab performed the similar experiments with other mechanogated (Piezo) for putatively mechanogated (Tmc) channel. Interestingly, though the AS cells of the other mutants maintained an anisotropic morphology like the *nompC*$^{\Delta}$ embryos throughout the elliptical phase, junction cut experiments produced very different results. The axial junction tension was not significantly different from the WT in all the mutants. However, the lateral junction tension always significantly differed from their WT counterparts, see Figure 4.1. It shows, though an increased force is commonly inferred from the direction of the major axis of cell anisotropy, it is not a steadfast principal. When two or more tissues are interacting, several other factors like viscoelasticity, role of cytoskeletal components etc. need to be considered.

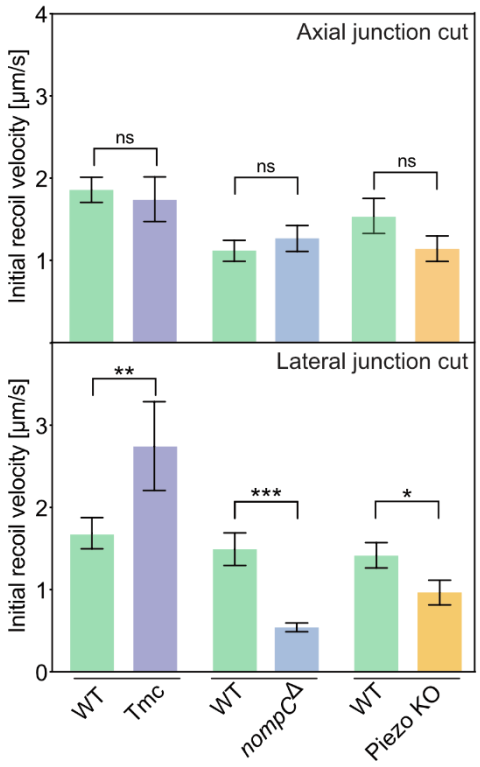

Figure 4.1. Mechanogated channels contribute to the tissue-scale force distribution very differently despite having similar morphometry. My former colleague Dr. Richa and Qiyan, my colleague did the junction ablation experiments in Tmc and piezo mutants respectively. In the piezo mutants, the lateral junction tension decreased like the NompC mutants, only to a lesser extent. However, the same for the Tmc mutants increased, indicating to a different mechanism of action. It requires further research to dissect the exact molecular mechanism of these ion channels in epithelial cells.

As the AS cells experience a pulling force from the lateral epidermis from both sides, I asked if the force exerted by the LE was different in the WT and *nompC*$^{\Delta}$ embryos. Ablating lateral junctions of the lateral epidermis made me conclude that the pulling by the LE is comparable in the WT and *nompC*$^{\Delta}$ embryos (Figure 3.28). These results indicate to a force imbalance between AS And LE. AS cells are either unable to sense the force from LE or to generate a resistive force intrinsically and thus passively complying to extend laterally.

To test whether the AS junction tension depends on the lateral pull from the LE, I optically severed AS from the LE. The lateral junction tension in the WT AS cells dropped to the level of *nompC*$^{\Delta}$ embryos (Figure 3.29). It suggests that the AS tissue is somehow unable to resist the force exerted by the LE in the absence of NompC. This is

probably the reason why the AS tissue remains wide open even when the DC onsets. Instead of generating a opposing force to balance the pulling from the LE, the AS cells simply elongate to the direction of the LE, causing their anisotropic cell shape all throughout. The observation is schematically summarised in Figure 4.2.

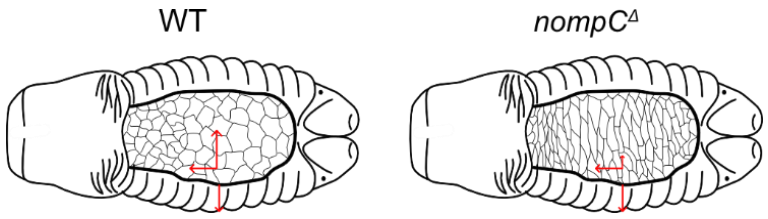

Figure 4.2. Schematic representation of the tension distribution in the WT and *nompC*$^{\Delta}$ embryos. The lateral junction tension of the AS cells in the WT embryos was higher than the axial junction tension. In the *nompC*$^{\Delta}$ embryos, the situation is reversed, with a greatly decreased lateral junction tension. The axial junction tension was comparable with that of the WT. Lateral junction tension of the LE was also comparable. The facts suggest that either the AS cells are unable to generate resistive force against the pulling force from the LE or, the cell junctions experience only a part of the force.

I also noticed an anisotropic distribution of the microtubules along the direction of cell anisotropy (Figure 3.25). I hypothesized that the part of the force from the lateral epidermis is also absorbed by the microtubules, see Figure 4.3. My hypothesis is based on the fact that the recoil velocities in single junction cut vs. the tissue cut can be different and microtubules can be reason behind it (Lv *et al.*, 2022).

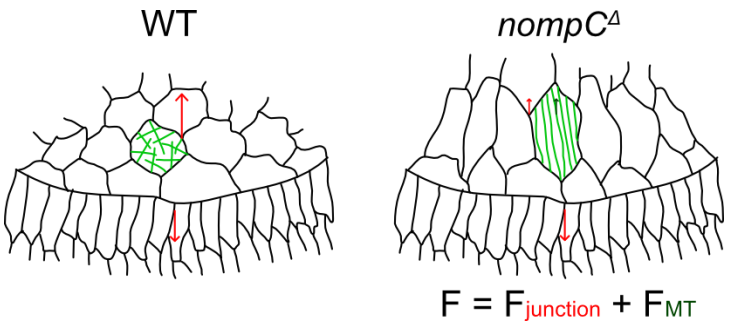

Figure 4.3. A part of the tension experienced by the AS cells is supposed to be absorbed by the microtubules. As the embryo progress into DC, in the WT embryos, the microtubules become less anisotropic than in the *nompC*$^{\Delta}$ embryos. The laterally oriented microtubules along with the cell junctions

may also experience the pulling force from the LE, whereas the cell junctions are subjected to more tension if the microtubules are randomly oriented.

To decipher if the tissue cut behaves differently than the junction cut, I severed the AS tissue in the middle, in the wild type embryos (Figure 3.30). I observed the recoil velocity decreased as the DC onsets from the elliptical phase. This temporal transition in recoil velocities were absent in the absence of NompC (Figure 3.31). The recoil at the elliptical phase, however, was significantly less than the WT. This is in agreement with the observation by single junction cuts. In the absence of NompC, the AS acts like a loose tissue, unable to generate intrinsic force. But the temporal transition of the recoil was missing as the anisotopically distributed microtubules might soak part of the pulling force from the LE.

4.12. NompC is an essential regulator of coordinated cell behaviour in AS tissue

Previously, Solon *et al.* put forward the idea that the instead of behaving individually AS cells were, in fact, coordinated. The authors reported an anti-sync. coordination between neighbouring pairs, and sync. coordination between distant pairs. Ablating junction between two neighbouring cells made the surrounding cells stop pulsing (Solon *et al.*, 2009). This suggested a mechanical coupling with the contracting cells. However, the procedure was invasive and only took a few couple of cells into account. To break this barrier, I took advantage of Cycle-GAN based large-scale image processing and analysis pipeline (Figure3.33).

Loss of mechanosensitive ion channel NompC affected not only the oscillatory dynamics of the AS cell, but also the intercellular coordination between adjacent pair of cells. Continuous oscillations of AS cells are non-autonomous and coordinated with the neighbouring cells in the tissue. Neighbour-dependent contractions are either positively or negatively or neutrally correlated in a pair of AS cells. Analysis of intercellular coordination of all possible AS cell-pairs sharing at least one junction revealed ~1.6 times higher number of synchronised cell pairs over the anti-synchronised ones in the WT embryos. This ratio was decreased to ~0.7 in the $nompC^{\Delta}$ embryos though the overall correlation remained unaffected (Figure 3.34). The left shift in the

frequency distribution of correlated cell pairs was caused by a significant increase in the anti-synchronised cell pairs at an equal expense of the synchronised pairs. The coupling strength (the parameter that is responsible for the synchronisation) also reduced in the absence of NompC (WT=0.0446, *nompC*$^{\Delta}$=0.0431). Figure 4.4 shows the gist of my findings.

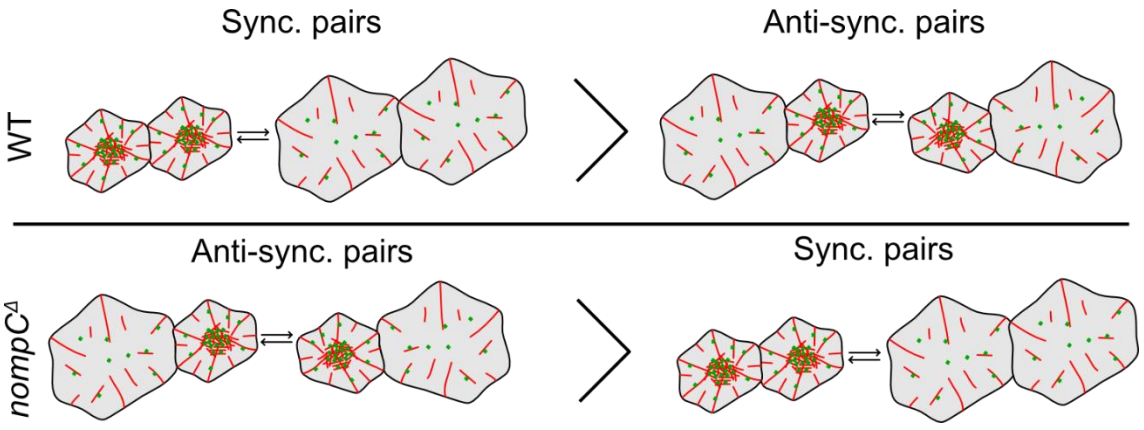

Figure 4.4. Overview of the cell-cell coordination in WT and *nompC*$^{\Delta}$ embryos. Sync. cell pairs are more abundant in the WT embryos, meaning a high degree of coordination between cells. The coordination is lost in the absence of NompC, though not completely but to a great extent, resulting in an increase in anti-sync. cell pairs.

The distribution of sync. pairs along the principle axis of the embryo was essentially bimodal. The peak at the anterior side was higher in WT embryos compared to the *nompC*$^{\Delta}$ ones. Absence of NompC clearly reduced specifically the anterior population of sync. cell pairs. The loss of sync. pairs in *nompC*$^{\Delta}$ embryos was replenished by an equal increase in anti-sync. pairs (Figure 3.35).

These results strongly suggests that NompC is an important regulator of cell-cell coordination the epithelial tissue. This can also explain why the WT AS tissue gradually transition from the elliptical to the DC phase with a significant reduction in the overall tissue area, whereas this transition happened without much reduction in the open AS area in the absence of NompC.

Conclusion

In this study, I have shown that mechanosensitive ion channels like NompC are not only active in neurons but also in the epithelial cells. During morphogenesis epithelial cells need to have a highly coordinated movements, of which NompC is regulator. NompC drives the cells to generate and sense forces via regulating the cytoskeletal components, though the exact mechanism is not fully understood yet. Absence of NompC leads to disruption of the tissue-scale tension distribution. My study also indicates a seminal role of Ca^{2+} with respect to epithelial morphogenesis. For the first time, I showed epithelial cell dynamics is in sync with the intracellular Ca^{2+} density dynamics. Mechanosensitive ion channels, though are categorised broadly under one umbrella term, seem to have very different gating and signal transduction mechanisms.

Based on my findings, I can say that NompC, being an ion channel, drives epithelial cell contraction supposedly via a Ca^{2+}-dependent way. NompC receives the mechanical inputs could be directly from the microtubules, the only known interacting partner forming the cytoskeleton. Due to a short extracellular domain, there is no known interactors at the extracellular domain of NompC. However, it is possible that NompC interacts with other proteins, e.g. E-cad or other channel proteins (Brv1, Nanchung *etc*.) that, in turn, interact with proteins from the neighbouring cells, establishing a machinery of direct cell-cell communication. The model is summarised in Figure 4.5.

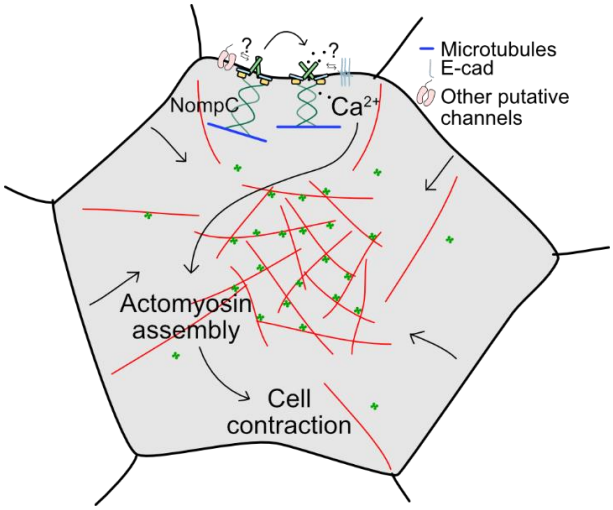

Figure 4.5. Model showing the proposed function of NompC in epithelial cells. Compressive forces from microtubules make the NompC channel adapt an open conformation that allows Ca^{2+} influx, causing

actomyosin assembly and cell contraction. However, how NompC acts as a coordinator between neighbouring cell dynamics is still an open question. It is hypothesised that junction proteins or other mechano-gated channels together with NompC establish direct communication between cells.

Bibliography

Abe, K., 2000. Therapeutic Potential of Neurotrophic Factors and Neural Stem Cells Against Ischemic Brain Injury. J. Cereb. Blood Flow Metab. 20, 1393–1408. https://doi.org/10.1097/00004647-200010000-00001

Adams, C.M., Anderson, M.G., Motto, D.G., Price, M.P., Johnson, W.A., Welsh, M.J., 1998. Ripped Pocket and Pickpocket, Novel Drosophila DEG/ENaC Subunits Expressed in Early Development and in Mechanosensory Neurons. J. Cell Biol. 140, 143–152. https://doi.org/10.1083/jcb.140.1.143

Angulo-Urarte, A., van der Wal, T., Huveneers, S., 2020. Cell-cell junctions as sensors and transducers of mechanical forces. Biochim. Biophys. Acta BBA - Biomembr. 1862, 183316. https://doi.org/10.1016/j.bbamem.2020.183316

Antunes, M., Pereira, T., Cordeiro, J.V., Almeida, L., Jacinto, A., 2013. Coordinated waves of actomyosin flow and apical cell constriction immediately after wounding. J. Cell Biol. 202, 365–379. https://doi.org/10.1083/jcb.201211039

Bachmann, A., Schneider, M., Theilenberg, E., Grawe, F., Knust, E., 2001. Drosophila Stardust is a partner of Crumbs in the control of epithelial cell polarity. Nature 414, 638–643. https://doi.org/10.1038/414638a

Bailles, A., Collinet, C., Philippe, J.-M., Lenne, P.-F., Munro, E., Lecuit, T., 2019. Genetic induction and mechano-chemical propagation of a morphogenetic wave. Nature 572, 467–473. https://doi.org/10.1038/s41586-019-1492-9

Balaji, R., Bielmeier, C., Harz, H., Bates, J., Stadler, C., Hildebrand, A., Classen, A.-K., 2017. Calcium spikes, waves and oscillations in a large, patterned epithelial tissue. Sci. Rep. 7, 42786. https://doi.org/10.1038/srep42786

Ben-Jonathan, N., Liu, J.W., 1992. Pituitary lactotrophs: endocrine, paracrine, juxtacrine, and autocrine interactions. Trends Endocrinol. Metab. TEM 3, 254–258. https://doi.org/10.1016/1043-2760(92)90127-m

Beyder, A., 2018. Gut development on a full stomach. Nat. Rev. Gastroenterol. Hepatol. 15, 394–395. https://doi.org/10.1038/s41575-018-0012-y

Bischof, J., Maeda, R.K., Hediger, M., Karch, F., Basler, K., 2007. An optimized transgenesis system for Drosophila using germ-line-specific phiC31 integrases. Proc. Natl. Acad. Sci. U. S. A. 104, 3312–3317. https://doi.org/10.1073/pnas.0611511104

Bodenschatz, J.F.E., Ajmail, K., Skamrahl, M., Vache, M., Gottwald, J., Nehls, S., Janshoff, A., 2022. Epithelial cells sacrifice excess area to preserve fluidity in response to external mechanical stress. Commun. Biol. 5, 1–11. https://doi.org/10.1038/s42003-022-03809-8

Bosch, J.A., Perrimon, N., 2022. Prime Editing for Precise Genome Engineering in Drosophila. Methods Mol. Biol. Clifton NJ 2540, 113–134. https://doi.org/10.1007/978-1-0716-2541-5_5

Brodskiy, P.A., Wu, Q., Soundarrajan, D.K., Huizar, F.J., Chen, J., Liang, P., Narciso, C., Levis, M.K., Arredondo-Walsh, N., Chen, D.Z., Zartman, J.J., 2019. Decoding Calcium Signaling Dynamics during Drosophila Wing Disc Development. Biophys. J. 116, 725–740. https://doi.org/10.1016/j.bpj.2019.01.007

Buckley, C.D., Tan, J., Anderson, K.L., Hanein, D., Volkmann, N., Weis, W.I., Nelson, W.J., Dunn, A.R., 2014. Cell adhesion. The minimal cadherin-catenin complex

binds to actin filaments under force. Science 346, 1254211. https://doi.org/10.1126/science.1254211
CAI, Y., SHEETZ, M.P., 2009. Force Propagation across Cells: Mechanical Coherence of Dynamic Cytoskeletons. Curr. Opin. Cell Biol. 21, 47–50. https://doi.org/10.1016/j.ceb.2009.01.020
Chanet, S., Martin, A.C., 2014. Mechanical Force Sensing in Tissues. Prog. Mol. Biol. Transl. Sci. 126, 317–352. https://doi.org/10.1016/B978-0-12-394624-9.00013-0
Chanet, S., Miller, C.J., Vaishnav, E.D., Ermentrout, B., Davidson, L.A., Martin, A.C., 2017. Actomyosin meshwork mechanosensing enables tissue shape to orient cell force. Nat. Commun. 8, 15014. https://doi.org/10.1038/ncomms15014
Chen, J., Peng, Y., Zhang, H., Wang, K., Zhao, C., Zhu, G., Reddy Palli, S., Han, Z., 2021. Off-target effects of RNAi correlate with the mismatch rate between dsRNA and non-target mRNA. RNA Biol. 18, 1747–1759. https://doi.org/10.1080/15476286.2020.1868680
Chen, Y., Ju, L., Rushdi, M., Ge, C., Zhu, C., 2017. Receptor-mediated cell mechanosensing. Mol. Biol. Cell 28, 3134–3155. https://doi.org/10.1091/mbc.e17-04-0228
Chou, T.B., Perrimon, N., 1996. The autosomal FLP-DFS technique for generating germline mosaics in Drosophila melanogaster. Genetics 144, 1673–1679. https://doi.org/10.1093/genetics/144.4.1673
Christensen, A.P., Corey, D.P., 2007. TRP channels in mechanosensation: direct or indirect activation? Nat. Rev. Neurosci. 8, 510–521. https://doi.org/10.1038/nrn2149
Clément, R., Dehapiot, B., Collinet, C., Lecuit, T., Lenne, P.-F., 2017. Viscoelastic Dissipation Stabilizes Cell Shape Changes during Tissue Morphogenesis. Curr. Biol. 27, 3132-3142.e4. https://doi.org/10.1016/j.cub.2017.09.005
Collinet, C., Lecuit, T., 2021a. Deterministic and self-organizational modes of morphogenetic information. Nat. Rev. Mol. Cell Biol. 22, 245. https://doi.org/10.1038/s41580-020-00318-6
Collinet, C., Lecuit, T., 2021b. Programmed and self-organized flow of information during morphogenesis. Nat. Rev. Mol. Cell Biol. 22, 245–265. https://doi.org/10.1038/s41580-020-00318-6
Coravos, J.S., Martin, A.C., 2016. Apical sarcomere-like actomyosin contracts nonmuscle Drosophila epithelial cells. Dev. Cell 39, 346–358. https://doi.org/10.1016/j.devcel.2016.09.023
Corominas-Murtra, B., Petridou, N.I., 2021. Viscoelastic Networks: Forming Cells and Tissues. Front. Phys. 9.
Courtemanche, N., 2018. Mechanisms of formin-mediated actin assembly and dynamics. Biophys. Rev. 10, 1553–1569. https://doi.org/10.1007/s12551-018-0468-6
Cox, C.D., Bavi, N., Martinac, B., 2019. Biophysical Principles of Ion-Channel-Mediated Mechanosensory Transduction. Cell Rep. 29, 1–12. https://doi.org/10.1016/j.celrep.2019.08.075
Créton, R., Kreiling, J.A., Jaffe, L.F., 2000. Presence and Roles of Calcium Gradients along the Dorsal-Ventral Axis in Drosophila Embryos. Dev. Biol. 217, 375–385. https://doi.org/10.1006/dbio.1999.9542

Das, D., Jülich, D., Schwendinger-Schreck, J., Guillon, E., Lawton, A.K., Dray, N., Emonet, T., O'Hern, C.S., Shattuck, M.D., Holley, S.A., 2019. Organization of Embryonic Morphogenesis via Mechanical Information. Dev. Cell 49, 829-839.e5. https://doi.org/10.1016/j.devcel.2019.05.014

David, R., Luu, O., Damm, E.W., Wen, J.W.H., Nagel, M., Winklbauer, R., 2014. Tissue cohesion and the mechanics of cell rearrangement. Dev. Camb. Engl. 141, 3672–3682. https://doi.org/10.1242/dev.104315

Dehapiot, B., Clément, R., Alégot, H., Gazsó-Gerhát, G., Philippe, J.-M., Lecuit, T., 2020. Assembly of a persistent apical actin network by the formin Frl/Fmnl tunes epithelial cell deformability. Nat. Cell Biol. 22, 791–802. https://doi.org/10.1038/s41556-020-0524-x

Deng, H., Gerencser, A.A., Jasper, H., 2015. Signal integration by Ca2+ regulates intestinal stem-cell activity. Nature 528, 212–217. https://doi.org/10.1038/nature16170

Dogterom, M., Koenderink, G.H., 2019. Actin–microtubule crosstalk in cell biology. Nat. Rev. Mol. Cell Biol. 20, 38–54. https://doi.org/10.1038/s41580-018-0067-1

Doubrovinski, K., Swan, M., Polyakov, O., Wieschaus, E.F., 2017. Measurement of cortical elasticity in Drosophila melanogaster embryos using ferrofluids. Proc. Natl. Acad. Sci. 114, 1051–1056. https://doi.org/10.1073/pnas.1616659114

Drees, F., Pokutta, S., Yamada, S., Nelson, W.J., Weis, W.I., 2005. α-Catenin Is a Molecular Switch that Binds E-Cadherin-β-Catenin and Regulates Actin-Filament Assembly. Cell 123, 903–915. https://doi.org/10.1016/j.cell.2005.09.021

DuFort, C.C., Paszek, M.J., Weaver, V.M., 2011. Balancing forces: architectural control of mechanotransduction. Nat. Rev. Mol. Cell Biol. 12, 308–319. https://doi.org/10.1038/nrm3112

Duque, J., Gorfinkiel, N., 2016. Integration of actomyosin contractility with cell-cell adhesion during dorsal closure. Dev. Camb. Engl. 143, 4676–4686. https://doi.org/10.1242/dev.136127

Emmons-Bell, M., Hariharan, I.K., 2021. Membrane potential regulates Hedgehog signalling in the Drosophila wing imaginal disc. EMBO Rep. 22, e51861. https://doi.org/10.15252/embr.202051861

Ferrandiz-Huertas, C., Mathivanan, S., Wolf, C.J., Devesa, I., Ferrer-Montiel, A., 2014. Trafficking of ThermoTRP Channels. Membranes 4, 525–564. https://doi.org/10.3390/membranes4030525

Fichtner, D., Lorenz, B., Engin, S., Deichmann, C., Oelkers, M., Janshoff, A., Menke, A., Wedlich, D., Franz, C.M., 2014. Covalent and Density-Controlled Surface Immobilization of E-Cadherin for Adhesion Force Spectroscopy. PLOS ONE 9, e93123. https://doi.org/10.1371/journal.pone.0093123

Fischer, S.C., Blanchard, G.B., Duque, J., Adams, R.J., Arias, A.M., Guest, S.D., Gorfinkiel, N., 2014. Contractile and mechanical properties of epithelia with perturbed actomyosin dynamics. PloS One 9, e95695. https://doi.org/10.1371/journal.pone.0095695

Flores-Benitez, D., Knust, E., 2015. Crumbs is an essential regulator of cytoskeletal dynamics and cell-cell adhesion during dorsal closure in Drosophila. eLife 4, e07398. https://doi.org/10.7554/eLife.07398

Friedl, P., Gilmour, D., 2009. Collective cell migration in morphogenesis, regeneration and cancer. Nat. Rev. Mol. Cell Biol. 10, 445–457. https://doi.org/10.1038/nrm2720
Gilmour, D., Rembold, M., Leptin, M., 2017. From morphogen to morphogenesis and back. Nature 541, 311–320. https://doi.org/10.1038/nature21348
Goldstein, B., Nance, J., 2020. Caenorhabditis elegans Gastrulation: A Model for Understanding How Cells Polarize, Change Shape, and Journey Toward the Center of an Embryo. Genetics 214, 265–277. https://doi.org/10.1534/genetics.119.300240
Gomez, J.M., Chumakova, L., Bulgakova, N.A., Brown, N.H., 2016. Microtubule organization is determined by the shape of epithelial cells. Nat. Commun. 7, 13172. https://doi.org/10.1038/ncomms13172
Gong, J., Nirala, N.K., Chen, J., Wang, F., Gu, P., Wen, Q., Ip, Y.T., Xiang, Y., 2023. TrpA1 is a shear stress mechanosensing channel regulating intestinal stem cell proliferation in Drosophila. Sci. Adv. 9, eadc9660. https://doi.org/10.1126/sciadv.adc9660
Guillot, C., Lecuit, T., 2013. Mechanics of Epithelial Tissue Homeostasis and Morphogenesis. Science 340, 1185–1189. https://doi.org/10.1126/science.1235249
Guo, Y., Wang, Y., Zhang, W., Meltzer, S., Zanini, D., Yu, Y., Li, J., Cheng, T., Guo, Z., Wang, Q., Jacobs, J.S., Sharma, Y., Eberl, D.F., Göpfert, M.C., Jan, L.Y., Jan, Y.N., Wang, Z., 2016. Transmembrane channel-like (tmc) gene regulates Drosophila larval locomotion. Proc. Natl. Acad. Sci. 113, 7243–7248. https://doi.org/10.1073/pnas.1606537113
Hara, Y., Shagirov, M., Toyama, Y., 2016. Cell Boundary Elongation by Non-autonomous Contractility in Cell Oscillation. Curr. Biol. 26, 2388–2396. https://doi.org/10.1016/j.cub.2016.07.003
Häring, M., Großhans, J., Wolf, F., Eule, S., 2018. Automated Segmentation of Epithelial Tissue Using Cycle-Consistent Generative Adversarial Networks. https://doi.org/10.1101/311373
Hartenstein, V., Campos-Ortega, J.A., 1985. Fate-mapping in wild-typeDrosophila melanogaster. Wilhelm Rouxs Arch. Dev. Biol. 194, 181–195. https://doi.org/10.1007/BF00848246
Hartshorne, D.J., Ito, M., Erdödi, F., 1998. Myosin light chain phosphatase: subunit composition, interactions and regulation. J. Muscle Res. Cell Motil. 19, 325–341. https://doi.org/10.1023/a:1005385302064
Haswell, E.S., Phillips, R., Rees, D.C., 2011. Mechanosensitive channels: what can they do and how do they do it? Struct. Lond. Engl. 1993 19, 1356–1369. https://doi.org/10.1016/j.str.2011.09.005
Hayes, P., Solon, J., 2017. Drosophila dorsal closure: An orchestra of forces to zip shut the embryo. Mech. Dev., Roles of physical forces in development 144, 2–10. https://doi.org/10.1016/j.mod.2016.12.005
He, L., Si, G., Huang, J., Samuel, A.D.T., Perrimon, N., 2018. Mechanical regulation of stem-cell differentiation by the stretch-activated Piezo channel. Nature 555, 103–106. https://doi.org/10.1038/nature25744

He, L., Wang, X., Tang, H.L., Montell, D.J., 2010. Tissue elongation requires oscillating contractions of a basal actomyosin network. Nat. Cell Biol. 12, 1133–1142. https://doi.org/10.1038/ncb2124

He, M., Ye, W., Wang, W.-J., Sison, E.S., Jan, Y.N., Jan, L.Y., 2017. Cytoplasmic Cl− couples membrane remodeling to epithelial morphogenesis. Proc. Natl. Acad. Sci. 114, E11161–E11169. https://doi.org/10.1073/pnas.1714448115

Homem, C.C.F., Peifer, M., 2008. Diaphanous regulates myosin and adherens junctions to control cell contractility and protrusive behavior during morphogenesis. Development 135, 1005–1018. https://doi.org/10.1242/dev.016337

Hoon, J.L., Tan, M.H., Koh, C.-G., 2016. The Regulation of Cellular Responses to Mechanical Cues by Rho GTPases. Cells 5, 17. https://doi.org/10.3390/cells5020017

Huang, J., Zhou, W., Dong, W., Watson, A.M., Hong, Y., 2009. Directed, efficient, and versatile modifications of the Drosophila genome by genomic engineering. Proc. Natl. Acad. Sci. 106, 8284–8289. https://doi.org/10.1073/pnas.0900641106

Huebner, R.J., Wallingford, J.B., 2018. Coming to Consensus: A Unifying Model Emerges for Convergent Extension. Dev. Cell 46, 389–396. https://doi.org/10.1016/j.devcel.2018.08.003

Hunter, G., 2012. The Role of Mechanically Gated Ion Channels in Dorsal Closure During Drosophila Morphogenesis.

Hunter, G.L., Crawford, J.M., Genkins, J.Z., Kiehart, D.P., 2014. Ion channels contribute to the regulation of cell sheet forces during Drosophila dorsal closure. Development 141, 325–334. https://doi.org/10.1242/dev.097097

Hutson, M.S., Tokutake, Y., Chang, M.-S., Bloor, J.W., Venakides, S., Kiehart, D.P., Edwards, G.S., 2003. Forces for morphogenesis investigated with laser microsurgery and quantitative modeling. Science 300, 145–149. https://doi.org/10.1126/science.1079552

Indra, I., Troyanovsky, R.B., Shapiro, L., Honig, B., Troyanovsky, S.M., 2020. Sensing Actin Dynamics through Adherens Junctions. Cell Rep. 30, 2820-2833.e3. https://doi.org/10.1016/j.celrep.2020.01.106

Inoue, Y., Suzuki, M., Watanabe, T., Yasue, N., Tateo, I., Adachi, T., Ueno, N., 2016. Mechanical roles of apical constriction, cell elongation, and cell migration during neural tube formation in Xenopus. Biomech. Model. Mechanobiol. 15, 1733–1746. https://doi.org/10.1007/s10237-016-0794-1

Irvine, K.D., Wieschaus, E., 1994. Cell intercalation during Drosophila germband extension and its regulation by pair-rule segmentation genes. Dev. Camb. Engl. 120, 827–841. https://doi.org/10.1242/dev.120.4.827

Jaalouk, D.E., Lammerding, J., 2009. Mechanotransduction gone awry. Nat. Rev. Mol. Cell Biol. 10, 63–73. https://doi.org/10.1038/nrm2597

Jacinto, A., Wood, W., Woolner, S., Hiley, C., Turner, L., Wilson, C., Martinez-Arias, A., Martin, P., 2002. Dynamic Analysis of Actin Cable Function during Drosophila Dorsal Closure. Curr. Biol. 12, 1245–1250. https://doi.org/10.1016/S0960-9822(02)00955-7

Jaffe, L.F., 2010. Fast calcium waves. Cell Calcium 48, 102–113. https://doi.org/10.1016/j.ceca.2010.08.007

Janmey, P.A., Miller, R.T., 2011. Mechanisms of mechanical signaling in development and disease. J. Cell Sci. 124, 9–18. https://doi.org/10.1242/jcs.071001
Jayasinghe, A.K., Crews, S.M., Mashburn, D.N., Hutson, M.S., 2013. Apical Oscillations in Amnioserosa Cells: Basolateral Coupling and Mechanical Autonomy. Biophys. J. 105, 255–265. https://doi.org/10.1016/j.bpj.2013.05.027
Jeong, H., Clark, S., Goehring, A., Dehghani-Ghahnaviyeh, S., Rasouli, A., Tajkhorshid, E., Gouaux, E., 2022. Structures of the TMC-1 complex illuminate mechanosensory transduction. Nature 610, 796–803. https://doi.org/10.1038/s41586-022-05314-8
Jin, P., Bulkley, D., Guo, Y., Zhang, W., Guo, Z., Huynh, W., Wu, S., Meltzer, S., Cheng, T., Jan, L.Y., Jan, Y.-N., Cheng, Y., 2017a. Electron cryo-microscopy structure of the mechanotransduction channel NOMPC. Nature 547, 118–122. https://doi.org/10.1038/nature22981
Jin, P., Bulkley, D., Guo, Y., Zhang, W., Guo, Z., Huynh, W., Wu, S., Meltzer, S., Cheng, T., Jan, L.Y., Jan, Y.-N., Cheng, Y., 2017b. Cryo-EM Structure of the Mechanotransduction Channel NOMPC. Nature 547, 118–122. https://doi.org/10.1038/nature22981
Jung, W., Li, J., Chaudhuri, O., Kim, T., 2020. Nonlinear Elastic and Inelastic Properties of Cells. J. Biomech. Eng. 142, 100806. https://doi.org/10.1115/1.4046863
Kernan, M., Cowan, D., Zuker, C., 1994. Genetic dissection of mechanosensory transduction: mechanoreception-defective mutations of Drosophila. Neuron 12, 1195–1206. https://doi.org/10.1016/0896-6273(94)90437-5
Kiehart, D.P., Crawford, J.M., Aristotelous, A., Venakides, S., Edwards, G.S., 2017. Cell Sheet Morphogenesis: Dorsal Closure in Drosophila melanogaster as a Model System. Annu. Rev. Cell Dev. Biol. 33, 169–202. https://doi.org/10.1146/annurev-cellbio-111315-125357
Kiehart, D.P., Galbraith, C.G., Edwards, K.A., Rickoll, W.L., Montague, R.A., 2000. Multiple Forces Contribute to Cell Sheet Morphogenesis for Dorsal Closure in Drosophila. J. Cell Biol. 149, 471–490. https://doi.org/10.1083/jcb.149.2.471
Kim, S.E., Coste, B., Chadha, A., Cook, B., Patapoutian, A., 2012. The role of Drosophila Piezo in mechanical nociception. Nature 483, 209–212. https://doi.org/10.1038/nature10801
Kindberg, A., Hu, J., Bush, J.O., 2020. “Forced to communicate: integration of mechanical and biochemical signaling in morphogenesis.” Curr. Opin. Cell Biol. 66, 59–68. https://doi.org/10.1016/j.ceb.2020.05.004
Kong, D., Großhans, J., 2020. Planar Cell Polarity and E-Cadherin in Tissue-Scale Shape Changes in Drosophila Embryos. Front. Cell Dev. Biol. 0. https://doi.org/10.3389/fcell.2020.619958
Kong, D., Lv, Z., Häring, M., Lin, B., Wolf, F., Großhans, J., 2019. In vivo optochemical control of cell contractility at single-cell resolution. EMBO Rep. 20, e47755. https://doi.org/10.15252/embr.201947755
Koshland, D.E., 1958. Application of a Theory of Enzyme Specificity to Protein Synthesis. Proc. Natl. Acad. Sci. U. S. A. 44, 98–104. https://doi.org/10.1073/pnas.44.2.98

Kuo, I.Y., Ehrlich, B.E., 2015. Signaling in Muscle Contraction. Cold Spring Harb. Perspect. Biol. 7, a006023. https://doi.org/10.1101/cshperspect.a006023
Lacy, M.E., Hutson, M.S., 2016. Amnioserosa development and function in Drosophila embryogenesis: Critical mechanical roles for an extraembryonic tissue. Dev. Dyn. 245, 558–568. https://doi.org/10.1002/dvdy.24395
Lai, S.-L., Chan, T.-H., Lin, M.-J., Huang, W.-P., Lou, S.-W., Lee, S.-J., 2008. Diaphanous-related formin 2 and profilin I are required for gastrulation cell movements. PloS One 3, e3439. https://doi.org/10.1371/journal.pone.0003439
Lam, P.Y., Webb, S.E., Leclerc, C., Moreau, M., Miller, A.L., 2009. Inhibition of stored Ca2+ release disrupts convergence-related cell movements in the lateral intermediate mesoderm resulting in abnormal positioning and morphology of the pronephric anlagen in intact zebrafish embryos. Dev. Growth Differ. 51, 429–442. https://doi.org/10.1111/j.1440-169X.2009.01106.x
Lane, M.C., Koehl, M.A.R., Wilt, F., Keller, R., 1993. A role for regulated secretion of apical extracellular matrix during epithelial invagination in the sea urchin. Development 117, 1049–1060. https://doi.org/10.1242/dev.117.3.1049
Lee, H., Nagele, R.G., 1986. Toxic and teratologic effects of verapamil on early chick embryos: Evidence for the involvement of calcium in neural tube closure. Teratology 33, 203–211. https://doi.org/10.1002/tera.1420330207
Lee, H.C., Auersperg, N., 1980. Calcium in epithelial cell contraction. J. Cell Biol. 85, 325–336. https://doi.org/10.1083/jcb.85.2.325
Lehne, F., Pokrant, T., Parbin, S., Salinas, G., Großhans, J., Rust, K., Faix, J., Bogdan, S., 2022. Calcium bursts allow rapid reorganization of EFhD2/Swip-1 cross-linked actin networks in epithelial wound closure. Nat. Commun. 13, 2492. https://doi.org/10.1038/s41467-022-30167-0
Lehnert, B.P., Baker, A.E., Gaudry, Q., Chiang, A.-S., Wilson, R.I., 2013. Distinct Roles of TRP Channels in Auditory Transduction and Amplification in Drosophila. Neuron 77, 115–128. https://doi.org/10.1016/j.neuron.2012.11.030
Lembong, J., Sabass, B., Stone, H.A., 2017. Calcium oscillations in wounded fibroblast monolayers are spatially regulated through substrate mechanics. Phys. Biol. 14, 045006. https://doi.org/10.1088/1478-3975/aa6b67
Lemieux, R.U., Spohr, U., 1994. How Emil Fischer was Led to the Lock and Key Concept for Enzyme Specificity11Presented at the symposium “Emil Fischer: 100 Years of Carbohydrate Chemistry,” 203rd National Meeting of the American Chemical Society, Division of Carbohydrate Chemistry, San Francisco, California, April 5–10, 1992., in: Horton, D. (Ed.), Advances in Carbohydrate Chemistry and Biochemistry. Academic Press, pp. 1–20. https://doi.org/10.1016/S0065-2318(08)60149-3
Lemke, S.B., Nelson, C.M., 2021. Dynamic changes in epithelial cell packing during tissue morphogenesis. Curr. Biol. CB 31, R1098–R1110. https://doi.org/10.1016/j.cub.2021.07.078
Leoni, G., Neumann, P.-A., Sumagin, R., Denning, T., Nusrat, A., 2015. Wound repair: role of immune–epithelial interactions. Mucosal Immunol. 8, 959–968. https://doi.org/10.1038/mi.2015.63
Levin, M., 2012. Morphogenetic fields in embryogenesis, regeneration, and cancer: Non-local control of complex patterning. Biosystems 109, 243–261. https://doi.org/10.1016/j.biosystems.2012.04.005

Leybaert, L., Sanderson, M.J., 2012. Intercellular Ca2+ Waves: Mechanisms and Function. Physiol. Rev. 92, 1359–1392. https://doi.org/10.1152/physrev.00029.2011

Li, B., Li, S., Zheng, H., Yan, Z., 2021. Nanchung and Inactive define pore properties of the native auditory transduction channel in *Drosophila*. Proc. Natl. Acad. Sci. 118, e2106459118. https://doi.org/10.1073/pnas.2106459118

Li, C., Rezania, S., Kammerer, S., Sokolowski, A., Devaney, T., Gorischek, A., Jahn, S., Hackl, H., Groschner, K., Windpassinger, C., Malle, E., Bauernhofer, T., Schreibmayer, W., 2015. Piezo1 forms mechanosensitive ion channels in the human MCF-7 breast cancer cell line. Sci. Rep. 5, 8364. https://doi.org/10.1038/srep08364

Li, J.X.H., Tang, V.W., Brieher, W.M., 2020. Actin protrusions push at apical junctions to maintain E-cadherin adhesion. Proc. Natl. Acad. Sci. 117, 432–438. https://doi.org/10.1073/pnas.1908654117

Liang, X., Gomez, G.A., Yap, A.S., 2015. Current perspectives on cadherin-cytoskeleton interactions and dynamics. Cell Health Cytoskelet. 7, 11–24. https://doi.org/10.2147/CHC.S76107

Liang, X., Madrid, J., Gärtner, R., Verbavatz, J.-M., Schiklenk, C., Wilsch-Bräuninger, M., Bogdanova, A., Stenger, F., Voigt, A., Howard, J., 2013. A NOMPC-dependent membrane-microtubule connector is a candidate for the gating spring in fly mechanoreceptors. Curr. Biol. CB 23, 755–763. https://doi.org/10.1016/j.cub.2013.03.065

Liang, X., Michael, M., Gomez, G.A., 2016. Measurement of Mechanical Tension at Cell-cell Junctions Using Two-photon Laser Ablation. Bio-Protoc. 6, e2068. https://doi.org/10.21769/BioProtoc.2068

Lv, Z., Zhang, N., Zhang, X., Großhans, J., Kong, D., 2022. The Lateral Epidermis Actively Counteracts Pulling by the Amnioserosa During Dorsal Closure. Front. Cell Dev. Biol. 10, 865397. https://doi.org/10.3389/fcell.2022.865397

Lynch, J.A., El-Sherif, E., Brown, S.J., 2012. Comparisons of the embryonic development of Drosophila, Nasonia, and Tribolium. WIREs Dev. Biol. 1, 16–39. https://doi.org/10.1002/wdev.3

Maître, J.-L., Heisenberg, C.-P., 2013. Three Functions of Cadherins in Cell Adhesion. Curr. Biol. 23, R626–R633. https://doi.org/10.1016/j.cub.2013.06.019

Markova, O., Lenne, P.-F., 2012. Calcium signaling in developing embryos: Focus on the regulation of cell shape changes and collective movements. Semin. Cell Dev. Biol., RNA Editing & Developmental Cell Behavior 23, 298–307. https://doi.org/10.1016/j.semcdb.2012.03.006

Markova, O., Senatore, S., Lenne, P.-F., 2019. Spatiotemporal dynamics of calcium transients during embryogenesis of Drosophila melanogaster. https://doi.org/10.1101/540070

Martin, A.C., 2020. The Physical Mechanisms of Drosophila Gastrulation: Mesoderm and Endoderm Invagination. Genetics 214, 543–560. https://doi.org/10.1534/genetics.119.301292

Martin, A.C., 2010. Pulsation and stabilization: Contractile forces that underlie morphogenesis. Dev. Biol., Special Section: Morphogenesis 341, 114–125. https://doi.org/10.1016/j.ydbio.2009.10.031

Martin, A.C., Goldstein, B., 2014. Apical constriction: themes and variations on a cellular mechanism driving morphogenesis. Dev. Camb. Engl. 141, 1987–1998. https://doi.org/10.1242/dev.102228
Martin, A.C., Kaschube, M., Wieschaus, E.F., 2009. Pulsed contractions of an actin-myosin network drive apical constriction. Nature 457, 495–499. https://doi.org/10.1038/nature07522
Martinac, B., Kloda, A., 2003. Evolutionary origins of mechanosensitive ion channels. Prog. Biophys. Mol. Biol., Mechano-Electric Feedback and Cardiac Arrhythmias 82, 11–24. https://doi.org/10.1016/S0079-6107(03)00002-6
Martino, F., Perestrelo, A.R., Vinarský, V., Pagliari, S., Forte, G., 2018. Cellular Mechanotransduction: From Tension to Function. Front. Physiol. 9.
Matsuda, M., Sokol, S.Y., 2021. Xenopus neural tube closure: A vertebrate model linking planar cell polarity to actomyosin contractions. Curr. Top. Dev. Biol. 145, 41–60. https://doi.org/10.1016/bs.ctdb.2021.04.001
McCleery, W.T., Veldhuis, J., Bennett, M.E., Lynch, H.E., Ma, X., Brodland, G.W., Hutson, M.S., 2019. Elongated Cells Drive Morphogenesis in a Surface-Wrapped Finite-Element Model of Germband Retraction. Biophys. J. 117, 157–169. https://doi.org/10.1016/j.bpj.2019.05.023
Mège, R.M., Ishiyama, N., 2017. Integration of Cadherin Adhesion and Cytoskeleton at Adherens Junctions. Cold Spring Harb. Perspect. Biol. 9, a028738. https://doi.org/10.1101/cshperspect.a028738
Miao, H., Blankenship, J.T., 2020. The pulse of morphogenesis: actomyosin dynamics and regulation in epithelia. Development 147, dev186502. https://doi.org/10.1242/dev.186502
Miller, C.J., Davidson, L., 2013. The interplay between cell signaling and mechanics in developmental processes. Nat. Rev. Genet. 14, 733–744. https://doi.org/10.1038/nrg3513
Miyake, Y., Inoue, N., Nishimura, K., Kinoshita, N., Hosoya, H., Yonemura, S., 2006. Actomyosin tension is required for correct recruitment of adherens junction components and zonula occludens formation. Exp. Cell Res. 312, 1637–1650. https://doi.org/10.1016/j.yexcr.2006.01.031
Molnar, K., Labouesse, M., 2021. The plastic cell: mechanical deformation of cells and tissues. Open Biol. 11, 210006. https://doi.org/10.1098/rsob.210006
Moore, R.P., Fogerson, S.M., Tulu, U.S., Yu, J.W., Cox, A.H., Sican, M.A., Li, D., Legant, W.R., Weigel, A.V., Crawford, J.M., Betzig, E., Kiehart, D.P., 2022. Superresolution microscopy reveals actomyosin dynamics in medioapical arrays. Mol. Biol. Cell 33, ar94. https://doi.org/10.1091/mbc.E21-11-0537
Morali, O., Savagner, P., Larue, L., 2013. Epithelium–Mesenchyme Transitions Are Crucial Morphogenetic Events Occurring During Early Development, in: Madame Curie Bioscience Database [Internet]. Landes Bioscience.
Moran, D., Rice, R.W., 1976. Action of papaverine and ionophore A23187 on neurulation. Nature 261, 497–499. https://doi.org/10.1038/261497a0
Mui, K.L., Chen, C.S., Assoian, R.K., 2016. The mechanical regulation of integrin–cadherin crosstalk organizes cells, signaling and forces. J. Cell Sci. 129, 1093–1100. https://doi.org/10.1242/jcs.183699

Murrell, M., Oakes, P.W., Lenz, M., Gardel, M.L., 2015. Forcing cells into shape: the mechanics of actomyosin contractility. Nat. Rev. Mol. Cell Biol. 16, 486–498. https://doi.org/10.1038/nrm4012
Nance, J., Zallen, J.A., 2011. Elaborating polarity: PAR proteins and the cytoskeleton. Dev. Camb. Engl. 138, 799–809. https://doi.org/10.1242/dev.053538
Nelson, C.M., 2009. Geometric control of tissue morphogenesis. Biochim. Biophys. Acta 1793, 903–910. https://doi.org/10.1016/j.bbamcr.2008.12.014
Newell-Litwa, K.A., Horwitz, R., Lamers, M.L., 2015. Non-muscle myosin II in disease: mechanisms and therapeutic opportunities. Dis. Model. Mech. 8, 1495–1515. https://doi.org/10.1242/dmm.022103
Nobe, K., Nobe, H., Obara, K., Paul, R.J., 2000. Preferential role of intracellular Ca2+ stores in regulation of isometric force in NIH 3T3 fibroblast fibers. J. Physiol. 529 Pt 3, 669–679. https://doi.org/10.1111/j.1469-7793.2000.00669.x
Paré, A.C., Vichas, A., Fincher, C.T., Mirman, Z., Farrell, D.L., Mainieri, A., Zallen, J.A., 2014. A positional Toll receptor code directs convergent extension in Drosophila. Nature 515, 523–527. https://doi.org/10.1038/nature13953
Pasakarnis, L., Frei, E., Caussinus, E., Affolter, M., Brunner, D., 2016. Amnioserosa cell constriction but not epidermal actin cable tension autonomously drives dorsal closure. Nat. Cell Biol. 18, 1161–1172. https://doi.org/10.1038/ncb3420
Pedersen, S.F., Owsianik, G., Nilius, B., 2005. TRP channels: An overview. Cell Calcium, Frontiers in calcium signalling 38, 233–252. https://doi.org/10.1016/j.ceca.2005.06.028
Perez, T.D., Nelson, W.J., 2004. Cadherin Adhesion: Mechanisms and Molecular Interactions. Handb. Exp. Pharmacol. 3–21. https://doi.org/10.1007/978-3-540-68170-0_1
Perez-Vale, K.Z., Peifer, M., 2020. Orchestrating morphogenesis: building the body plan by cell shape changes and movements. Dev. Camb. Engl. 147, dev191049. https://doi.org/10.1242/dev.191049
Perrimon, N., 1984. Clonal Analysis of Dominant Female-Sterile, Germline-Dependent Mutations in DROSOPHILA MELANOGASTER. Genetics 108, 927–939.
Petzold, J., Gentleman, E., 2021. Intrinsic Mechanical Cues and Their Impact on Stem Cells and Embryogenesis. Front. Cell Dev. Biol. 9.
Plageman, T.F., Chung, M.-I., Lou, M., Smith, A.N., Hildebrand, J.D., Wallingford, J.B., Lang, R.A., 2010. Pax6-dependent Shroom3 expression regulates apical constriction during lens placode invagination. Dev. Camb. Engl. 137, 405–415. https://doi.org/10.1242/dev.045369
Ranade, S.S., Syeda, R., Patapoutian, A., 2015. Mechanically Activated Ion Channels. Neuron 87, 1162–1179. https://doi.org/10.1016/j.neuron.2015.08.032
Rauzi, M., Hočevar Brezavšček, A., Ziherl, P., Leptin, M., 2013. Physical Models of Mesoderm Invagination in Drosophila Embryo. Biophys. J. 105, 3–10. https://doi.org/10.1016/j.bpj.2013.05.039
Rauzi, M., Lenne, P.-F., 2011. Chapter four - Cortical Forces in Cell Shape Changes and Tissue Morphogenesis, in: Labouesse, M. (Ed.), Current Topics in Developmental Biology, Forces and Tension in Development. Academic Press, pp. 93–144. https://doi.org/10.1016/B978-0-12-385065-2.00004-9

Reed, B.H., Wilk, R., Lipshitz, H.D., 2001. Downregulation of Jun kinase signaling in the amnioserosa is essential for dorsal closure of the Drosophila embryo. Curr. Biol. 11, 1098–1108. https://doi.org/10.1016/S0960-9822(01)00318-9

Restrepo, S., Basler, K., 2016. Drosophila wing imaginal discs respond to mechanical injury via slow InsP3R-mediated intercellular calcium waves. Nat. Commun. 7, 12450. https://doi.org/10.1038/ncomms12450

Rezakhaniha, R., Agianniotis, A., Schrauwen, J.T.C., Griffa, A., Sage, D., Bouten, C.V.C., van de Vosse, F.N., Unser, M., Stergiopulos, N., 2012. Experimental investigation of collagen waviness and orientation in the arterial adventitia using confocal laser scanning microscopy. Biomech. Model. Mechanobiol. 11, 461–473. https://doi.org/10.1007/s10237-011-0325-z

Richa, P., 2019. Role of mechanosensitive ion channels in coordinated epithelial cell dynamics in Drosophila. Georg-August-University Göttingen. https://doi.org/10.53846/goediss-7714

Richards, J.S., Ascoli, M., 2018. Endocrine, Paracrine, and Autocrine Signaling Pathways That Regulate Ovulation. Trends Endocrinol. Metab. TEM 29, 313–325. https://doi.org/10.1016/j.tem.2018.02.012

Rivera-Pérez, J.A., Hadjantonakis, A.-K., 2015. The Dynamics of Morphogenesis in the Early Mouse Embryo. Cold Spring Harb. Perspect. Biol. 7, a015867. https://doi.org/10.1101/cshperspect.a015867

Ron, A., Azeloglu, E.U., Calizo, R.C., Hu, M., Bhattacharya, S., Chen, Y., Jayaraman, G., Lee, S., Neves-Zaph, S.R., Li, H., Gordon, R.E., He, J.C., Hone, J.C., Iyengar, R., 2017. Cell shape information is transduced through tension-independent mechanisms. Nat. Commun. 8, 2145. https://doi.org/10.1038/s41467-017-02218-4

Roth, S., Stein, D., Nüsslein-Volhard, C., 1989. A gradient of nuclear localization of the dorsal protein determines dorsoventral pattern in the Drosophila embryo. Cell 59, 1189–1202. https://doi.org/10.1016/0092-8674(89)90774-5

Roy Choudhury, A., Großhans, J., Kong, D., 2021. Ion Channels in Epithelial Dynamics and Morphogenesis. Cells 10, 2280. https://doi.org/10.3390/cells10092280

Saias, L., Swoger, J., D'Angelo, A., Hayes, P., Colombelli, J., Sharpe, J., Salbreux, G., Solon, J., 2015. Decrease in Cell Volume Generates Contractile Forces Driving Dorsal Closure. Dev. Cell 33, 611–621. https://doi.org/10.1016/j.devcel.2015.03.016

Salazar-Ciudad, I., Jernvall, J., Newman, S.A., 2003. Mechanisms of pattern formation in development and evolution, in: Development. pp. 2027–2037. https://doi.org/10.1242/dev.00425

Sammak, P.J., Hinman, L.E., Tran, P.O.T., Sjaastad, M.D., Machen, T.E., 1997. How do injured cells communicate with the surviving cell monolayer? J. Cell Sci. 110, 465–475. https://doi.org/10.1242/jcs.110.4.465

Schöck, F., Perrimon, N., 2003. Retraction of the Drosophila germ band requires cell–matrix interaction. Genes Dev. 17, 597–602. https://doi.org/10.1101/gad.1068403

Sharif-Naeini, R., 2015. Chapter Three - Contribution of Mechanosensitive Ion Channels to Somatosensation, in: Price, T.J., Dussor, G. (Eds.), Progress in Molecular Biology and Translational Science, Molecular and Cell Biology of

Pain. Academic Press, pp. 53–71. https://doi.org/10.1016/bs.pmbts.2014.11.011
Sheldahl, L.C., Slusarski, D.C., Pandur, P., Miller, J.R., Kühl, M., Moon, R.T., 2003. Dishevelled activates Ca2+ flux, PKC, and CamKII in vertebrate embryos. J. Cell Biol. 161, 769–777. https://doi.org/10.1083/jcb.200211094
Singh, A., Saha, T., Begemann, I., Ricker, A., Nüsse, H., Thorn-Seshold, O., Klingauf, J., Galic, M., Matis, M., 2018. Polarized microtubule dynamics directs cell mechanics and coordinates forces during epithelial morphogenesis. Nat. Cell Biol. 20, 1126–1133. https://doi.org/10.1038/s41556-018-0193-1
Slabodnick, M.M., Tintori, S.C., Prakash, M., Zhang, P., Higgins, C.D., Chen, A.H., Cupp, T.D., Wong, T., Bowie, E., Jug, F., Goldstein, B., 2023. Zyxin contributes to coupling between cell junctions and contractile actomyosin networks during apical constriction. PLOS Genet. 19, e1010319. https://doi.org/10.1371/journal.pgen.1010319
Slusarski, D.C., Corces, V.G., Moon, R.T., 1997. Interaction of Wnt and a Frizzled homologue triggers G-protein-linked phosphatidylinositol signalling. Nature 390, 410–413. https://doi.org/10.1038/37138
Smedley, M.J., Stanisstreet, M., 1986. Calcium and neurulation in mammalian embryos: II. Effects of cytoskeletal inhibitors and calcium antagonists on the neural folds of rat embryos. Development 93, 167–178. https://doi.org/10.1242/dev.93.1.167
Sokolow, A., Toyama, Y., Kiehart, D.P., Edwards, G.S., 2012. Cell Ingression and Apical Shape Oscillations during Dorsal Closure in Drosophila. Biophys. J. 102, 969–979. https://doi.org/10.1016/j.bpj.2012.01.027
Solon, J., Kaya-Çopur, A., Colombelli, J., Brunner, D., 2009. Pulsed Forces Timed by a Ratchet-like Mechanism Drive Directed Tissue Movement during Dorsal Closure. Cell 137, 1331–1342. https://doi.org/10.1016/j.cell.2009.03.050
Spencer, A.K., Siddiqui, B.A., Thomas, J.H., 2015. Cell shape change and invagination of the cephalic furrow involves reorganization of F-actin. Dev. Biol. 402, 192–207. https://doi.org/10.1016/j.ydbio.2015.03.022
St Johnston, D., Nüsslein-Volhard, C., 1992. The origin of pattern and polarity in the Drosophila embryo. Cell 68, 201–219. https://doi.org/10.1016/0092-8674(92)90466-p
Sumi, A., Hayes, P., D'Angelo, A., Colombelli, J., Salbreux, G., Dierkes, K., Solon, J., 2018. Adherens Junction Length during Tissue Contraction Is Controlled by the Mechanosensitive Activity of Actomyosin and Junctional Recycling. Dev. Cell 47, 453-463.e3. https://doi.org/10.1016/j.devcel.2018.10.025
Sun, L., Gao, Y., He, J., Cui, L., Meissner, J., Verbavatz, J.-M., Li, B., Feng, X., Liang, X., 2019. Ultrastructural organization of NompC in the mechanoreceptive organelle of Drosophila campaniform mechanoreceptors. Proc. Natl. Acad. Sci. 116, 7343–7352. https://doi.org/10.1073/pnas.1819371116
Sun, Z., Guo, S.S., Fässler, R., 2016. Integrin-mediated mechanotransduction. J. Cell Biol. 215, 445–456. https://doi.org/10.1083/jcb.201609037
Sutherland, A., Lesko, A., 2020. Pulsed actomyosin contractions in morphogenesis. https://doi.org/10.12688/f1000research.20874.1

Suzuki, M., Sato, M., Koyama, H., Hara, Y., Hayashi, K., Yasue, N., Imamura, H., Fujimori, T., Nagai, T., Campbell, R.E., Ueno, N., 2017. Distinct intracellular Ca2+ dynamics regulate apical constriction and differentially contribute to neural tube closure. Development 144, 1307–1316. https://doi.org/10.1242/dev.141952

Sweeton, D., Parks, S., Costa, M., Wieschaus, E., 1991. Gastrulation in *Drosophila:* the formation of the ventral furrow and posterior midgut invaginations. Development 112, 775–789. https://doi.org/10.1242/dev.112.3.775

Tepass, U., 2014. Polarize to elongate. Nature 515, 499–501. https://doi.org/10.1038/nature13937

Tostevin, F., Howard, M., 2008. Modeling the Establishment of PAR Protein Polarity in the One-Cell C. elegans Embryo. Biophys. J. 95, 4512–4522. https://doi.org/10.1529/biophysj.108.136416

Totsukawa, G., Yamakita, Y., Yamashiro, S., Hartshorne, D.J., Sasaki, Y., Matsumura, F., 2000. Distinct roles of ROCK (Rho-kinase) and MLCK in spatial regulation of MLC phosphorylation for assembly of stress fibers and focal adhesions in 3T3 fibroblasts. J. Cell Biol. 150, 797–806. https://doi.org/10.1083/jcb.150.4.797

Tripathi, A., Bankaitis, V.A., 2017. Molecular Docking: From Lock and Key to Combination Lock. J. Mol. Med. Clin. Appl. 2, 10.16966/2575-0305.106.

Umetsu, D., n.d. Cell mechanics and cell-cell recognition controls by Toll-like receptors in tissue morphogenesis and homeostasis. Fly (Austin) 16, 233–247. https://doi.org/10.1080/19336934.2022.2074783

Uray, I.P., Uray, K., 2021. Mechanotransduction at the Plasma Membrane-Cytoskeleton Interface. Int. J. Mol. Sci. 22, 11566. https://doi.org/10.3390/ijms222111566

van Soldt, B.J., Cardoso, W.V., 2020. Hippo-Yap/Taz signaling: Complex network interactions and impact in epithelial cell behavior. WIREs Dev. Biol. 9, e371. https://doi.org/10.1002/wdev.371

Vangeel, L., Voets, T., 2019. Transient Receptor Potential Channels and Calcium Signaling. Cold Spring Harb. Perspect. Biol. 11, a035048. https://doi.org/10.1101/cshperspect.a035048

Varadarajan, S., Chumki, S.A., Stephenson, R.E., Misterovich, E.R., Wu, J.L., Dudley, C.E., Erofeev, I.S., Goryachev, A.B., Miller, A.L., 2022. Mechanosensitive calcium flashes promote sustained RhoA activation during tight junction remodeling. J. Cell Biol. 221, e202105107. https://doi.org/10.1083/jcb.202105107

Vasquez, C.G., Heissler, S.M., Billington, N., Sellers, J.R., Martin, A.C., 2016. Drosophila non-muscle myosin II motor activity determines the rate of tissue folding. eLife 5, e20828. https://doi.org/10.7554/eLife.20828

Vasquez, C.G., Tworoger, M., Martin, A.C., 2014. Dynamic myosin phosphorylation regulates contractile pulses and tissue integrity during epithelial morphogenesis. J. Cell Biol. 206, 435–450. https://doi.org/10.1083/jcb.201402004

Verdier, V., Guang-Chao-Chen, null, Settleman, J., 2006. Rho-kinase regulates tissue morphogenesis via non-muscle myosin and LIM-kinase during Drosophila development. BMC Dev. Biol. 6, 38. https://doi.org/10.1186/1471-213X-6-38

Verin, A.D., Bogatcheva, N.V., 2006. CYTOSKELETAL PROTEINS, in: Laurent, G.J., Shapiro, S.D. (Eds.), Encyclopedia of Respiratory Medicine. Academic Press, Oxford, pp. 615–622. https://doi.org/10.1016/B0-12-370879-6/00108-3
Vicente-Manzanares, M., Ma, X., Adelstein, R.S., Horwitz, A.R., 2009. Non-muscle myosin II takes centre stage in cell adhesion and migration. Nat. Rev. Mol. Cell Biol. 10, 778–790. https://doi.org/10.1038/nrm2786
Walker, R.G., Willingham, A.T., Zuker, C.S., 2000. A Drosophila Mechanosensory Transduction Channel. Science 287, 2229–2234. https://doi.org/10.1126/science.287.5461.2229
Wallingford, J.B., Ewald, A.J., Harland, R.M., Fraser, S.E., 2001. Calcium signaling during convergent extension in Xenopus. Curr. Biol. 11, 652–661. https://doi.org/10.1016/S0960-9822(01)00201-9
Wang, Y., Guo, Y., Li, G., Liu, C., Wang, L., Zhang, A., Yan, Z., Song, C., 2021. The push-to-open mechanism of the tethered mechanosensitive ion channel NompC. eLife 10, e58388. https://doi.org/10.7554/eLife.58388
Warn, R.M., Robert-Nicoud, M., 1992. The formation and fate of the blastoderm epithelium of the Drosophila embryo, in: Fleming, T.P. (Ed.), Epithelial Organization and Development. Springer Netherlands, Dordrecht, pp. 137–161. https://doi.org/10.1007/978-94-011-2354-9_5
Wells, A.R., Zou, R.S., Tulu, U.S., Sokolow, A.C., Crawford, J.M., Edwards, G.S., Kiehart, D.P., 2014. Complete canthi removal reveals that forces from the amnioserosa alone are sufficient to drive dorsal closure in Drosophila. Mol. Biol. Cell 25, 3552–3568. https://doi.org/10.1091/mbc.E14-07-1190
Wyatt, T., Baum, B., Charras, G., 2016. A question of time: tissue adaptation to mechanical forces. Curr. Opin. Cell Biol. 38, 68–73. https://doi.org/10.1016/j.ceb.2016.02.012
Yan, Z., Zhang, W., He, Y., Gorczyca, D., Xiang, Y., Cheng, L.E., Meltzer, S., Jan, L.Y., Jan, Y.N., 2013. Drosophila NOMPC is a mechanotransduction channel subunit for gentle-touch sensation. Nature 493, 221–225. https://doi.org/10.1038/nature11685
Yevick, H.G., Miller, P.W., Dunkel, J., Martin, A.C., 2019. Structural redundancy in supracellular actomyosin networks enables robust tissue folding. Dev. Cell 50, 586-598.e3. https://doi.org/10.1016/j.devcel.2019.06.015
Young, P.E., Richman, A.M., Ketchum, A.S., Kiehart, D.P., 1993. Morphogenesis in Drosophila requires nonmuscle myosin heavy chain function. Genes Dev. 7, 29–41. https://doi.org/10.1101/gad.7.1.29
Zallen, J.A., Wieschaus, E., 2004. Patterned gene expression directs bipolar planar polarity in Drosophila. Dev. Cell 6, 343–355. https://doi.org/10.1016/s1534-5807(04)00060-7
Zechini, L., Amato, C., Scopelliti, A., Wood, W., 2022. Piezo acts as a molecular brake on wound closure to ensure effective inflammation and maintenance of epithelial integrity. Curr. Biol. 32, 3584-3592.e4. https://doi.org/10.1016/j.cub.2022.06.041
Zhang, W., Cheng, L.E., Kittelmann, M., Li, J., Petkovic, M., Cheng, T., Jin, P., Guo, Z., Göpfert, M.C., Jan, L.Y., Jan, Y.N., 2015. Ankyrin Repeats Convey Force to Gate the NOMPC Mechanotransduction Channel. Cell 162, 1391–1403. https://doi.org/10.1016/j.cell.2015.08.024

Zhang, W., Yan, Z., Jan, L.Y., Jan, Y.N., 2013. Sound response mediated by the TRP channels NOMPC, NANCHUNG, and INACTIVE in chordotonal organs of Drosophila larvae. Proc. Natl. Acad. Sci. U. S. A. 110, 13612–13617. https://doi.org/10.1073/pnas.1312477110

Zhang, Y., Rózsa, M., Liang, Y., Bushey, D., Wei, Z., Zheng, J., Reep, D., Broussard, G.J., Tsang, A., Tsegaye, G., Narayan, S., Obara, C.J., Lim, J.-X., Patel, R., Zhang, R., Ahrens, M.B., Turner, G.C., Wang, S.S.-H., Korff, W.L., Schreiter, E.R., Svoboda, K., Hasseman, J.P., Kolb, I., Looger, L.L., 2023. Fast and sensitive GCaMP calcium indicators for imaging neural populations. Nature 615, 884–891. https://doi.org/10.1038/s41586-023-05828-9

List of Figures